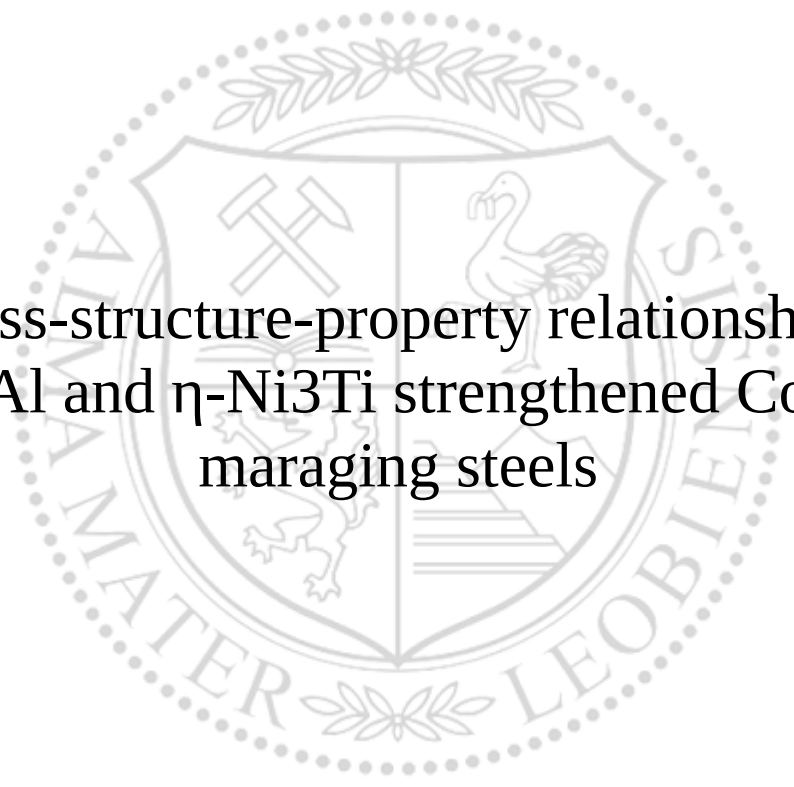




Chair of Physical Metallurgy

Doctoral Thesis



Process-structure-property relationships of
 β -NiAl and η -Ni₃Ti strengthened Co-free
maraging steels

Dipl.-Ing. Stefan Zeisl, BSc

February 2023



MONTANUNIVERSITÄT LEOBEN

www.unileoben.ac.at

AFFIDAVIT

I declare on oath that I wrote this thesis independently, did not use other than the specified sources and aids, and did not otherwise use any unauthorized aids.

I declare that I have read, understood, and complied with the guidelines of the senate of the Montanuniversität Leoben for "Good Scientific Practice".

Furthermore, I declare that the electronic and printed version of the submitted thesis are identical, both, formally and with regard to content.

Date 21.03.2023

Signature Author
Stefan Zeisl

“Life can only be understood backwards; but it must be lived forwards.”
Søren Kierkegaard

This work was supported by the Research Fund for Coal and Steel (RFCS)
in the framework of the *iNiTiAl* project. Grant agreement 847165.

Danksagung

Ich blicke zu diesem Zeitpunkt auf etwas mehr als zehn Jahre als Student an der Montanuniversität Leoben zurück. Es war eine Zeit geprägt von Hingabe, Aufopferung und dem Kampf mit den eigenen zweifelnden inneren Stimmen. Aber es war auch eine Zeit des Lernens über sich selbst, des Wachstums und der Erkenntnis alles zu schaffen wonach man seinen Willen richtet. Aber ein Studium wäre kein Studium ohne die Menschen die einen auf dem Weg begleiten. Ich bin dankbar für all die interessanten Leute aus den verschiedensten Kreisen die ich kennenlernen durfte, aber auch für die paar Freundschaften die ich über die Zeit knüpfen konnte. Danke für die interessanten Gespräche, die mit Sicherheit auch teilweise meine eigenen Ansichten in Frage gestellt haben und meine Denkweise geprägt haben.

Danke ebenfalls an meinen Betreuer Prof. Ronald Schnitzer. Nicht nur hast du meine Manuskripte immer rasch gelesen, deine Kritik und Anmerkungen waren auch sehr wertvoll und haben meine Schreibfähigkeiten deutlich verbessert. Auch meiner ehemaligen Vorgesetzten Dr. Francisca Mendez-Martin gebührt mein Dank. Schade dass du die Universität schon vor dem Ende meiner Dissertation verlassen hast, denn du hattest immer ein offenes Ohr für mich und es war echt super dass wir uns immer gegenseitig helfen konnten.

Die wichtigsten Begleiter neben meinem Studium waren mit Sicherheit meine Eltern Edith & Michael Zeisl. Nicht nur hatten sie immer ein offenes Ohr für meine Probleme und konnten meine Moral immer aufbessern wenn diese am Boden war (z.B. nach dem dritten Mechanik I Nicht genügend), sie haben mir auch immer die Möglichkeit geboten bei ihnen zu wohnen, was ich auch für den Großteil meines Studiums in Anspruch nahm. Danke für Alles, ich könnte mir keine besseren Eltern vorstellen.

Acknowledgements

This thesis was supported by the EU project “iNiTiAl” (RFCS 847165). I want to thank the EU and the Research Fund for Coal and Steel to make this project possible. Furthermore, I want to thank Nele Van Steenberge and Wahib Saikaly who did a great job at organizing and leading the project. A big thanks also goes out to our project partners from France (Aubert & Duval), Belgium (OCAS) and Germany (Liebherr Aerospace and RWTH Aachen). It was a pleasure to collaborate with you and thank you for always sending plenty of material to perform my studies with.

Abbreviations

AM	Additive manufacturing
APT	Atom probe tomography
CSR	Complete spatial randomness model
EBSD	Electron backscatter diffraction
HPT	High pressure torsion
L-DED	Laser based directed energy deposition
LEAP	Local electrode atom probe
LOM	Light optical microscopy
L-PBF	Laser powder bed fusion
M_s	Martensite start temperature
M_f	Martensite finish temperature
MSM	Maximum separation method
NMI	Non-metallic inclusions
PH	Precipitation hardening/hardened
SAD	Selected area diffraction
SPD	Severe plastic deformation
TEM	Transmission electron microscopy
TKD	Transmission Kikuchi diffraction
TRIP	Transformation induced plasticity
T_f	Forging temperature
VIM	Vacuum induction melting
VAR	Vacuum arc remelting
WAAM	Wire arc additive manufacturing
XRD	X-Ray diffraction

Contents

Contents	xi
Abstract	1
1 Motivation and aim of the thesis	3
2 State of the art	5
2.1 History of Maraging Steels	5
2.2 Processing	5
2.2.1 Manufacturing Route	7
2.2.2 Solution Annealing	7
2.2.3 Aging Heat Treatment	7
2.2.4 Additive Manufacturing	8
2.3 Microstructure of Maraging Steels	9
2.3.1 Martensite and Austenite	9
2.3.2 Precipitates	10
2.4 Strength of Maraging Steels	13
2.4.1 Grain Size Strengthening	14
2.4.2 Dislocation Density Strengthening	14
2.4.3 Solid Solution Strengthening	14
2.4.4 Phase Composition (Martensite & Austenite)	15
2.5 Precipitation Hardening	15
2.5.1 The precipitate life cycle	15
2.5.2 Precipitate-dislocation interactions	17
2.6 The role of alloying elements	19
2.7 Influence of deformation	20
3 Materials and Characterization Methods	23
3.1 Investigated Material	23

3.2	High-pressure torsion	24
3.3	Atom Probe Tomography	24
3.3.1	Technical background	24
3.3.2	Precipitate Characterization	26
4	Relation of the current thesis to the state of the art	29
5	Published Content	31
	Publication I	33
	Publication II	43
	Publication III	57
	Publication IV	67
6	Summary and discussion of the publications	99
6.1	Aim of the investigations	99
6.2	Influence of processing parameters on the precipitation	99
6.3	Influence of the chemical composition on the microstructure	103
6.4	Strengthening mechanisms of Fe-12Ni maraging steels	107
7	Novel features	111
8	Outlook	113
	Bibliography	115

Abstract

Abstract

Maraging steels are martensitic steels that are strengthened by the precipitation of nano-sized intermetallic phases and which are used for high-performance applications such as for aircraft parts, missile parts or in the sport industry. The strengthening effect of the precipitates can be severely influenced by the chemical composition, the process history, and the heat treatment parameters. The industrial steel grade that is used in this thesis is a candidate for a specific structural aircraft part. Furthermore, the goal is to manufacture these parts using recycled material. To ensure that the mechanical properties fulfill the requirements this thesis focuses on determining the influence of processing parameters and the chemical composition on the precipitation behavior, on the formation of austenite, and the mechanical properties of a Co-free maraging steel. To achieve this a combination of laboratory-processed model alloys and an industrially processed alloy with various heat treatment conditions were characterized using high-resolution methods. The microstructural changes were identified and correlated to the changes in strength, hardness, and toughness. Furthermore, a novel approach for determining the precipitation strengthening was developed and used to learn about the underlying strengthening mechanisms in η -Ni₃Ti and β -NiAl strengthened Co-free maraging steels. It was found that severe plastic deformation had a strong influence on the hardness and aging response, that the cooling rate can be used as a parameter to influence the precipitation hardening, and that the volume fraction of the η -Ni₃Ti and the β -NiAl precipitates is influenced by Cr, Mo and the Ti- and Al-concentration.

Kurzfassung

Maragingstähle sind martensitische Stähle, welche unter anderem für Teile in der Flugzeugindustrie, für militärische Raketen oder für Sportartikel Anwendung finden und welche durch die Ausscheidung von nanometergroßen intermetallischen Phasen verfestigt werden. Wie stark diese Ausscheidungen festigkeitsteigernd sind hängt von der chemischen Zusammensetzung, der Herstellroute und den Wärmebehandlungsparametern ab. Die industrielle Maraging Legierung, die in dieser Arbeit verwendet wurde, soll zukünftig für ein bestimmtes Bauteil im Flugzeugbau verwendet werden. Zusätzlich ist es das Ziel diese Teile mit Recyclingmaterial herzustellen. Um zu garantieren, dass die Anforderungen an die mechanischen Eigenschaften sichergestellt werden können, fokussiert sich diese Arbeit darauf wie die Prozessparameter und die chemische Zusammensetzung die Ausscheidungsbildung, die Austenitbildung und die mechanischen Eigenschaften beeinflussen. Dazu wurden verschiedene Legierungen, die eine Kombination aus industriell gefertigten, und im Labor gefertigten Material darstellen, mit hochauflösenden Methoden charakterisiert und daraus eine Beziehung zwischen Prozess, Struktur und Eigenschaften herstellt. Außerdem wurde eine Methode entwickelt um die Ausscheidungshärtung zu charakterisieren und um die zugrundeliegenden Mechanismen zu studieren, die bei η -Ni₃Ti und β -NiAl verfestigten Co-freien Maraging Stählen für die Festigkeit verantwortlich sind. Es stellte sich heraus das Hochverformung (engl. severe plastic deformation) die Härte und Geschwindigkeit der Ausscheidungsreaktion wesentlich beeinflusst, dass man die Ausscheidungsreaktion mit der Abkühlgeschwindigkeit gezielt beeinflussen kann und, dass der Phasenanteil der η -Ni₃Ti und der β -NiAl Ausscheidungsphase von Cr, Mo und dem Ti- und Al-Gehalt beeinflusst wird.

Motivation and aim of the thesis

This thesis is part of a larger project between partners from 4 different EU countries. Within this project, the goal is to manufacture a specific high-performance part using a novel maraging steel. This maraging steel will replace an existing carbon steel grade that is not corrosion resistant and which needs to be protected by environmentally hazardous anti-corrosion coatings.

Maraging steels are a class of high-strength steels which have various applications in the industry for high-performance parts, such as structural aircraft parts, missile hulls or fencing blades. Due to their high alloying content, high strength, and multiple heat treatments, they are costly to synthesize, forge and process. This is not only an economic disadvantage of these materials but also an ecologic disadvantage if the environmental impact of the energy expenditure of the synthesis is considered.

By using recycled material the energy expenditure and the costs of raw material can be reduced which gives the manufacturer a competitive advantage and which is a step towards a more livable environment for all organisms. However, the use of recycled material comes with the uncertainty of the chemical composition of the material. Unclean or not well-enough sorted scrap material might lead to an increased introduction of detrimental elements or variations in the concentration of alloying elements.

Therefore, the goal of this thesis is to address the issues that stem from using recycled material and to determine the process-structure-property relationship, which allows to guarantee the mechanical properties that satisfy and possibly surpass the requirements for a specific, undisclosed structural aircraft part. To achieve this a variety of processing parameters and alloys were tested and characterized using high-resolution methods such as atom probe tomography and transmission electron microscopy.

State of the art

2.1 History of Maraging Steels

Maraging steels were first introduced in the early 1960s by pioneer work from Bieber [1] and Decker, Eash, and Goldman [2]. Their idea was to create a steel based on a soft Ni-martensite and low carbon content to improve the toughness of their material. They found that these types of steels had excellent in-use properties such as machinability and weldability and showed only little dimensional changes during heat treatments [3]. These early maraging steels had a Ni concentration of 12 wt.% and more and were alloyed with Co and Mo. Their precipitation strengthening was based on Mo-rich phases that allowed for strengths up to 2060 MPa.

Co-alloyed maraging steels remain successful commercially and as a research topic to the present day. However, in the 1980s a Co shortage and rising Co prices led to the development of Co-free maraging steels [4]. Co-free maraging steels rely on the precipitation of different types of precipitates such as the β -NiAl or the η -Ni₃Ti phase.

2.2 Processing

Fig. 2.1 shows the typical processing route of a maraging steel from melting to aging the finished workpiece and Fig. 2.2 shows the heat treatment route alongside the microstructural evolution from the solution annealing to the aging. The individual steps that are shown in Fig. 2.1 and Fig. 2.2 are explained within the following sections.

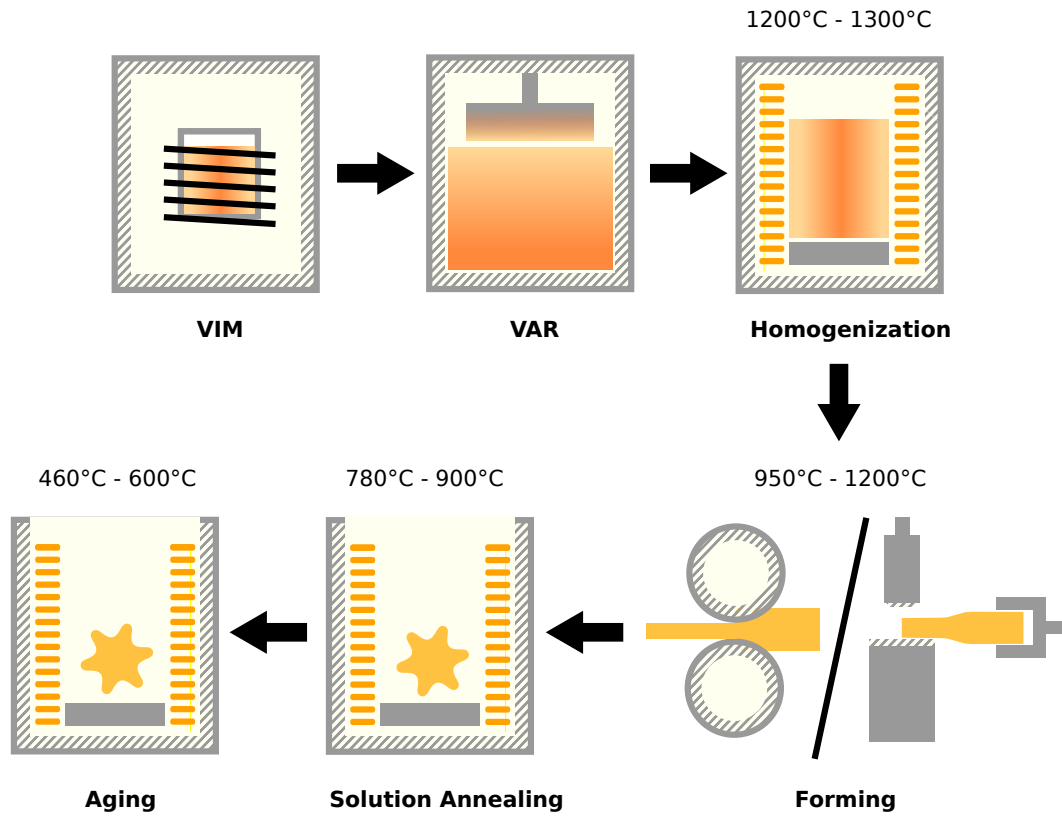


Figure 2.1: The processing route of a maraging steel workpiece from melting to aging the finished piece.

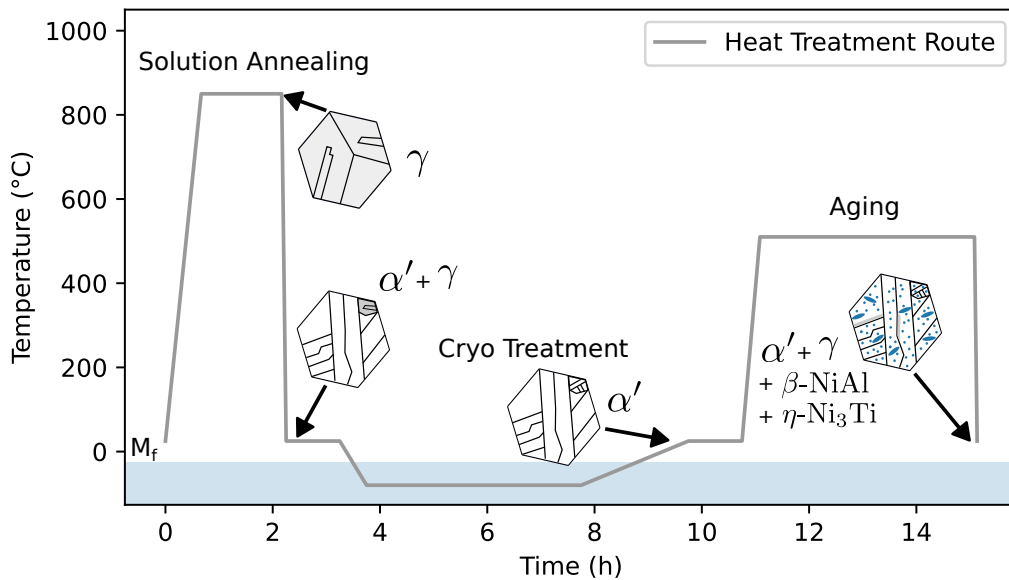


Figure 2.2: Heat treatment route of a typical maraging steel strengthened by two intermetallic phases. The figure shows the temperature control of the solution annealing, cryogenic treatment, and aging heat treatment as well as the microstructural composition at selected points.

2.2.1 Manufacturing Route

The traditional manufacturing route of maraging steels (opposed to the more modern additive manufacturing) consists of a combination of vacuum induction melting (VIM) and vacuum arc remelting (VAR). The combination of a vacuum/vacuum route can guarantee a higher degree of cleanliness and fewer non-metallic inclusions (NMI) [5]. For maraging steels, the main concern are non-spherical NMIs like Ti-sulfides and Ti-carbonitrides which have a detrimental effect on the mechanical properties.

After solidification high-strength maraging steels commonly show a banded microstructure that stems from segregation that occurs during solidification. A homogenization heat treatment between 1200°C and 1300°C for 2 h to 8 h can be used to improve the homogeneity of the microstructure [6] which ensures a uniform microstructure and mechanical properties.

After homogenization, the material is prepared for the form-giving process. The type of the form-giving process and the process temperatures can vary between manufacturers and applications. Commonly maraging steels are hot-deformed in the austenite phase region at temperatures between 950°C and 1200°C [7, 8]. Choosing the right forging temperature (T_f) is always a trade-off between the energy required for heating (low T_f is better), the energy required for forging (high T_f is better) and the risk of excessive austenite grain growth (low T_f is better [9]). The influence of deformation on the mechanical properties and the microstructure will be explained in section 2.7.

2.2.2 Solution Annealing

The first heat treatment is solution annealing (see Fig. 2.2). This heat treatment is performed in the austenite phase region and has the goal to ensure that all alloying elements are in a solid solution within the austenite. Li et al. [10] showed that this can be achieved with annealing temperatures between 780°C and 900°C. After the solution annealing the material is typically quenched in air or water and the austenite is transformed into martensite. If the martensite finish temperature is below the temperature of the medium that was used for quenching retained austenite can be present. A cryogenic treatment, where the material is soaked in a medium at cryogenic temperatures (e.g. -196°C) [11], can remove the retained austenite [12]. In the solution annealed condition, maraging steels exhibit a comparatively low hardness but good ductility. Studies [13–15] reported a hardness between ~240 HV and ~330 HV in this condition.

2.2.3 Aging Heat Treatment

The aging of the material is the final step in the thermal processing of the material and gives it its final mechanical properties. The aging temperatures and times are highly dependent on

the chemical composition of the maraging steel as well as the desired properties, but typical aging temperatures range between 460°C [16] and 600°C [17] and aging times can reach up to 100 h [18], but aging times between 1 h and 16 h are commonly used.

Aging is a highly complex process that includes multiple simultaneous microstructural changes. The early stages of aging are characterized by the formation of clusters of precipitating elements [19]. Meanwhile, austenite is formed at local Ni-enriched zones at the martensite lath boundaries [20, 21]. As the aging continues the clusters begin to form precipitates and the fraction of austenite increases. The precipitation significantly improves the strength of the material, while the formation of austenite decreases strength but improves toughness and ductility [21, 22]. If the material is aged for times past the peak hardness, then the precipitates begin to coarsen (see section 2.5.1) and the strength drops [19].

2.2.4 Additive Manufacturing

While this thesis focuses on the process-structure-property relationship of materials that were produced on the traditional route, the additive manufacturing (AM) of maraging steels becomes increasingly important. Fig. 2.3 shows the percentage of maraging steel research articles that include the search string “additive manufacturing”. The figure shows that the research interest in additive manufactured maraging steels steeply increased from 2014 onwards. Simultaneously the general research interest in maraging steels also increased as shown in Fig. 2.3.

AM has some advantages over traditional manufacturing like the production of complex geometries and more efficient use of materials. Maraging steels are a good candidate as raw materials for AM because of their good resistance against cracking during the solidification process and their complex and costly production of the raw material which encourages material efficiency [23]. In terms of the microstructural characteristics, maraging steels lend themselves to AM because of the fast solidification rates which promote the martensite transformation and a fine-grained structure which is beneficial for the mechanical properties [23].

Current AM technologies offer a variety of processes to choose from, but for maraging steels, the most relevant processes are laser powder bed fusion (L-PBF), wire arc additive manufacturing (WAAM), and laser-based directed energy deposition (L-DED) [23].

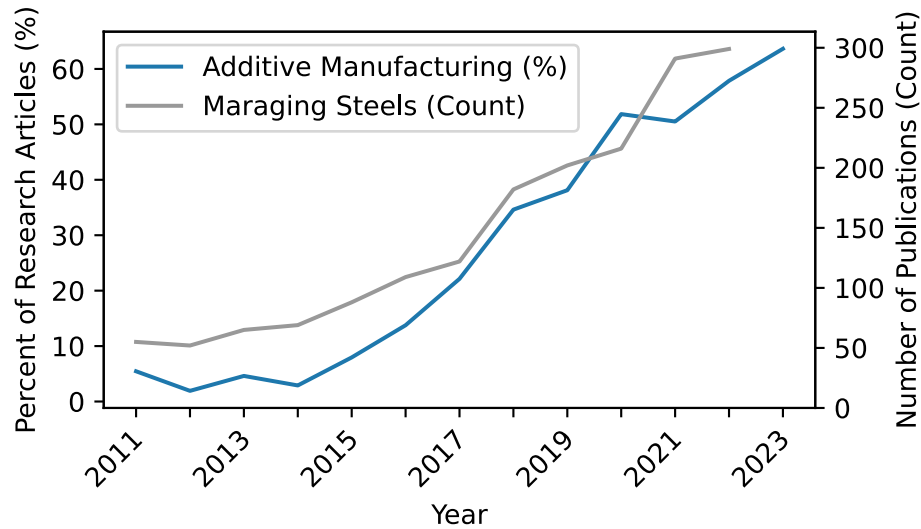


Figure 2.3: Total count of research articles about maraging steels found on the scientific search engine ScienceDirect and percentage of maraging steel research articles referencing or focusing on additive manufacturing (accessed December 2022).

2.3 Microstructure of Maraging Steels

2.3.1 Martensite and Austenite

The microstructure of maraging steels consists of three main components: the martensite matrix, austenite (as retained or reverted austenite), and the precipitates as shown in Fig. 2.4.

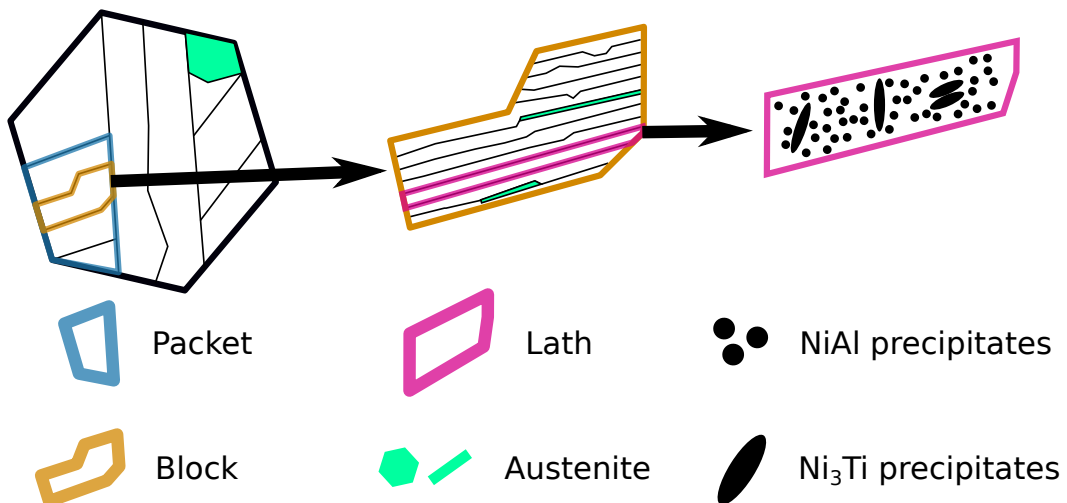


Figure 2.4: Schematic presentation of the hierarchical structure of a maraging steel strengthened with two different intermetallic phases.

The martensite matrix consists of a hierarchical structure of packets, blocks, and laths, with laths being the smallest structure, with lath widths in the order of a few 100 nm [24]. The

martensite structure starts to form at the boundaries of the prior austenite grains. The martensite itself has a body-centered cubic crystal structure ($a=0.2866$ nm) [25] and can show an orientation relationship with the prior austenite grains, namely the Kurdjumov-Sachs $((111)_\gamma // (1\bar{1}0)_\alpha, [\bar{1}10]_\gamma // [\bar{1}11]_\alpha)$ or the Nishiyama-Wassermann $((111)_\gamma // (1\bar{1}0)_\alpha, [\bar{1}01]_\gamma // [001]_\alpha)$ orientation relationship [26, 27]. Yao et al. [28] found that the size of the martensite sub-structures is related to the size of the prior austenite grains. In essence, this means that a finer prior austenite grain size leads to a finer martensite.

Austenite, which has a face-centered crystal structure ($a \approx 0.36$ nm) [29], can be present as retained austenite or as reverted austenite. Retained austenite remains after quenching from the solution annealing temperature if the martensite finish temperature is below the quenching temperature. The fraction of retained austenite can be reduced by conducting a cryogenic treatment, where the sample is soaked in a medium (e.g liquid nitrogen) at a temperature below the martensite finish temperature. However, retained austenite can not always be removed completely as demonstrated by Zhirafar et al. [11], who used a cryogenic treatment at -196°C to reduce the fraction of retained austenite from 5.7% to 4.2%. Wu et al. [30] found that the fraction of retained austenite after quenching is inversely proportional to the martensite start temperature (M_S), which can be calculated by an equation proposed by Barbier et al. [31]. Using only the elements relevant for this thesis, M_S can be calculated as: $M_S = 545 - 9.2Cr - 17.3Ni - 15.4Mo - 1.4Al - 2.44Ti$. This shows that the fraction of retained austenite should increase with a higher content of alloying elements.

Reverted austenite forms during the aging heat treatment of the maraging steel and can form with different morphologies, depending on the aging temperature [32]. Zhang et al. [32] found that at aging temperatures of 500°C the primary form of austenite was lath-like, as a film along the lath boundaries, while at 600°C the primary form was blocky. The role of reverted austenite in maraging steels is to improve the toughness and ductility via the transformation-induced plasticity (TRIP) effect [21, 22]. However, the drawback of an increased austenite fraction is a decreased yield strength and ultimate tensile strength [33].

Austenite can transform to martensite under mechanical stress [34] but also thermally activated [20]. The thermal stability of austenite is influenced by its chemical composition, but also by its grain size and morphology [20]. In contrast to thermal stability, mechanical stability is independent of the grain size of the austenite [35].

2.3.2 Precipitates

Precipitates are the property-defining microstructural constituent in maraging steels, which are formed during aging. For aging typical temperatures are between 450°C and 600°C and typical aging times can range from just one hour to several hours. Table 2.1 shows an

overview of phases that are commonly found within maraging steels. For Co-free maraging steels the β -NiAl and η -Ni₃Ti phases are often found in many different alloys [36–39]. Fig. 2.5 shows the unit cells of the β -NiAl phase and the η -Ni₃Ti phase.

Table 2.1: Overview of precipitate phases that are commonly found in maraging steels (MS).

Phase	Crystal Structure	Found In	Remarks
β -NiAl	B2 (CsCl structure)	Al alloyed MS [13–15]	homogeneous nucleation, spherical, coherent
η -Ni ₃ Ti	D0 ₂₄ (ordered hexagonal structure)	Ti alloyed MS [13, 40, 41]	nucleation at dislocations, rod-like morphology
Fe ₂ Mo	C14 (Laves phase)	Mo alloyed MS [14, 42]	
μ -Fe ₇ Mo ₆	stacked (0001) slabs of C14-Fe ₂ Mo	Mo alloyed MS [43]	more stable than the Fe ₂ Mo phase
ω phase	hexagonal	Ti free MS [43, 44]	precursor to Ni ₃ Mo and μ phase
G-Phase (Ti ₆ Si ₇ Ni ₁₆)	D8 _a [45]	Si and Ti alloyed MS [41, 46]	spherical

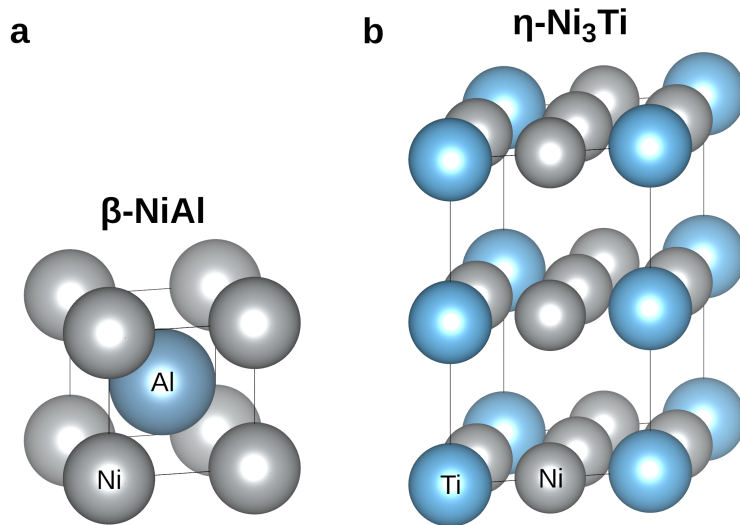


Figure 2.5: Unit cells of the a) β -NiAl phase and b) the η -Ni₃Ti phase.

β -NiAl This phase has a B2-type ordered crystal structure, as shown in Fig. 2.5 a. The lattice parameter of this phase is 2.887 Å at room temperature [14]. β -NiAl typically forms spherical particles which are coherent with the martensite matrix [14, 47]. In experiments by Sun et al. [14] where aging temperatures were varied (540-560°C) it was found that the size and distribution of β -NiAl are very sensitive to the aging temperature, showing an increase in volume fraction and a decrease in mean particle spacing with an increasing aging

temperature. Simm et al. [48] observed in local electrode atom probe (LEAP) tomography and small angle neutron scattering (SANS) studies that the volume fraction of β -NiAl precipitates increases rapidly during aging before saturation sets in and the volume fraction stays approximately constant with time (>1 h).

Huang et al. [15] found that the β -NiAl phase remains coherent and stable up to temperatures of 650°C. Schnitzer et al. [49] found that the addition of Cu leads to a faster formation of the β -NiAl precipitates by decreasing the misfit to the martensite matrix and that the β -NiAl phase forms directly and without precursor phase from the matrix phase [13].

Sun et al. [14] estimated that the strengthening effect of β -NiAl is around 700 MPa for a volume fraction of 12.3%. They also found that elements such as Cr, Mo, and Co were present in β -NiAl as solutes.

η -Ni₃Ti The η -Ni₃Ti phase is a semi-coherent phase that nucleates at dislocations [17]. Using LEAP and TEM measurements, studies [50, 51] have observed that this phase forms precipitates with rod-like morphology. The rod-like morphology stems from the enhanced diffusion along the dislocation cores [17]. Furthermore, due to the growth along the dislocation, the η -Ni₃Ti particles often show a preferential orientation within the matrix [17]. This phase has an ordered hexagonal close-packed crystal structure (D0₂₄-type) with lattice parameters of $a=5.101$ Å and $c=8.307$ Å [10, 40]. The crystal structure of this phase is shown in Fig. 2.5 b.

Studies found that the Ti sites can be substituted with Mo or Al [18, 40]. This phase has been reported in multiple Ti-containing steels [10, 13, 52, 53]. It is thought that it forms during the early stages of aging [53] as the lattice misfit, and thus the energy required for nucleation, is lower, compared to other phases [43]. He et al. [39] described that the Orowan mechanism is the dominant strengthening mechanism for this phase.

In the early stages of aging Ni-Ti-rich clusters with spherical morphology are formed [17]. These clusters act as a precursor for the η -Ni₃Ti phase [53]. The addition of Cu can affect the nucleation of this phase, as Ni-Ti-rich clusters are formed at Cu-rich clusters [41].

Laves phase A Fe₂Mo-type Laves phase was observed in studies of different maraging steels [14, 54]. Sun et al. [14] found that a primary Laves phase is formed during solution annealing at 825°C at the grain boundaries of the austenite. During the aging heat treatment, the formation of a secondary Laves phase was observed. The lattice parameters of the hexagonal laves phase with C14 structure were calculated to be $a=4.75$ Å and $c=7.73$ Å [14]. In creep tests, performed at 500°C and with a load of 700 MPa, they found that the secondary laves phase precipitates contribute to creep resistance, since the precipitates, which are formed at lath boundaries, hinder the movement of grain boundaries.

The contribution to the ultimate tensile strength was estimated to be ~ 200 MPa for a volume fraction of 6.4% [14].

G-phase A G-phase with the composition $\text{Ti}_6\text{Ni}_{16}\text{Si}_7$ can be observed in Si-containing maraging steels after very long aging times [41]. The G-phase shows an ordered $\text{Th}_6\text{Mn}_{23}\text{D}_{8a}$ structure with a $\text{Fm}\bar{3}\text{m}$ space group and a lattice parameter of $a=11.26$ Å [45]. Thuvander et al. [41] studied the precipitate evolution of a PH13-8 Mo type maraging steel and found that the evolution of the G-phase starts with Ni and Ti-rich clusters after 5 min of aging. From these clusters, γ' - $\text{Ni}_3(\text{Ti},\text{Al},\text{Si})$ precipitates are formed after 4 h of aging. After 100 h of aging the γ' particles were dissolved and the G-phase was formed, alongside a quasi-crystalline R' phase.

Other phases The ω phase is only observed in Ti-free steels and shows a hexagonal crystal structure [43, 44]. It is thought that this phase is a precursor to the more stable Ni_3Mo and μ phases [43].

The Ni_3Mo phase was observed in Co-containing and Co-free maraging steels [43] as one of the phases contributing to precipitation strengthening [55].

The μ phase Fe_7Mo_6 has a structure that consists of inter-grown $\{0001\}$ Laves phase slabs and is thought to be more stable than the Fe_2Mo Laves phase [43].

2.4 Strength of Maraging Steels

The mechanical strength of maraging steels is directly influenced by the microstructural characteristics, which are: the grain size, dislocation density, chemical composition, and phase composition (including precipitates). To establish meaningful process-structure-property relationships it is vital to determine the value of the strengthening contribution from the different mechanisms.

A comparison of the following studies highlights the broad spectrum of mechanical strength that is offered by maraging steels. Schnitzer et al. [47, 56] determined a hardness of 31 HRC in the quenched solution annealed condition of a PH 13-8 Mo corrosion-resistant maraging steel. After aging at 575°C the hardness of this steel increased to 42 HRC. Niu et al. [53] tested a $\text{Ni}_{18}\text{Co}_{15}\text{Mo}_7\text{Ti}_1$ maraging steel and found that the ultimate tensile strength increased from 798 MPa (34.5 HRC) in the solution annealed condition to 2564 MPa (60.5 HRC) in the aged condition.

The ductility and fracture elongation of maraging steels are also highly variable and dependent on the aging heat treatment [53] but also on the alloy composition. Examples of

typical fracture elongations in the peak aged condition are $\sim 2\text{-}3\%$ [53] for a Ni18Co15Mo7Ti1 maraging steel or $\sim 10\%$ for a PH 13-8 steel [57].

2.4.1 Grain Size Strengthening

Grain size strengthening is described by the Hall-Petch equation $\sigma_y = \sigma_0 + d^{-1/2} \cdot k_y$ [58], which relates the yield strength σ_y to the mean grain size d via the Hall-Petch factor k_y . σ_0 refers to the lattice friction stress [59].

Since lath martensite is a hierarchical structure of packets, blocks, and laths that form within a prior austenite grain there are four different structure sizes that can be considered for grain size strengthening. Morito et al. [60] investigated the relationship between the prior austenite grain size and the lath martensite sub-structures of a low-C steel and found that the block size and the packet size are strongly correlated to the prior austenite grain size while the lath size is only weakly correlated, which confirmed results found by Yao et al. [28]. To describe the Hall-Petch relationship using the prior austenite grain size Rack [58] conducted experiments with a 18% Ni maraging steel. They found that their maraging steel satisfied the Hall-Petch relationship across various chemical compositions in the solution annealed and the aged condition. The Hall-Petch factor k_y was found to be dependent on the chemistry and heat treatment condition, but it was within a range of $2160 \text{ MPa}\mu\text{m}^{1/2}$ and $4740 \text{ MPa}\mu\text{m}^{1/2}$ in the solution annealed condition. Later Galindo-Nava et al. [61] proposed a value of $k_y=300 \text{ MPa}\mu\text{m}^{1/2}$ when using the block size as grain size in the Hall-Petch equation.

2.4.2 Dislocation Density Strengthening

Maraging steels naturally have a high density of dislocations, which are introduced during quenching after the solution annealing heat treatment. Because of this, the strengthening effect of dislocations is an important factor for the strength of the precipitate-free martensite.

The value of the strengthening effect $\Delta\sigma_p$ can be described by the so-called Taylor equation: $\Delta\sigma_p = 0.25M\mu\rho$ [61] with μ being the shear modulus of the martensite matrix, $M=2.5$ being the Taylor orientation factor and ρ being the dislocation density.

2.4.3 Solid Solution Strengthening

Due to the high concentration of alloying elements in maraging steels solid solution strengthening not only plays a role in the solution annealed condition, but also in the aged condition. The value of solid solution strengthening $\Delta\sigma_{SS}$ is determined with the Fleischer model [61]:

$$\Delta\sigma_{SS} = \sum_i (\beta_i^2 x_i)^{1/2} \quad (2.1)$$

β_i and x_i correspond to the solid solution factor and the concentration (in at.%) of each alloying element, respectively. The solid solution factor β_i can be determined using Equation 2.2 according to Fleischer's formula [61, 62].

$$\beta_i = \kappa\mu(\eta'_i + 16\delta_i)^{3/2} \quad (2.2)$$

$\kappa = 0.0045$ [61] is a fitting parameter, $\eta'_i = \eta_i/(1 + 0.5\eta_i)$ are calculated from the modulus mismatch with respect to pure iron $\eta_i = |\mu_i - \mu_{Fe}|/\mu_{Fe}$ and the lattice mismatch with respect to pure iron $\delta_i = |r_i - r_{Fe}|/r_{Fe}$.

2.4.4 Phase Composition (Martensite & Austenite)

As described in section 2.3 the microstructure of maraging steels can contain austenite in various forms. Viswanthan et al. [33] showed that the yield strength decreases with an increasing austenite fraction. Their maraging steel was aged at 640°C for 5 different aging times between 1 h and 8 h, which led to austenite fractions between 8% and 24%. They found that the ultimate tensile strength decreased from 1715 MPa to 1458 MPa.

Schnitzer et al. [47] tested the tensile properties of pure reverted austenite and found that that condition had a yield strength of 217 MPa. Furthermore, they established that the strength of a combined martensite and austenite microstructure of a maraging steel can be described by a linear mixture rule [47, 56].

2.5 Precipitation Hardening

Alfred Wilm [63] was one of the pioneers of precipitation-hardened materials. In 1911 he published his work where he presented a precipitation-hardened Al-Mg alloy, which built the foundation for a class of materials that are nowadays used as material for air crafts. Since that time a lot has been accomplished, both in the development of Al-based precipitation-hardened alloys, but also with other metal alloys such as maraging steels, which were introduced commercially in the early 1960s [64].

The following sections will elaborate on how the formation of precipitates works, show the life cycle of the precipitates, and how the dislocation-precipitate interactions determine the strengthening effect of precipitates.

2.5.1 The precipitate life cycle

The precipitate life cycle begins with a supersaturated solid solution, which is produced by a solution annealing heat treatment at sufficient temperature and subsequent quenching [19]. The supersaturated solid solution is thermodynamically unstable, so given enough temperature, the solute elements will start to migrate.

Fig. 2.6 a-c shows the life cycle of precipitates from the formation of clusters to the coarsening of precipitates. In the current literature, the terms clusters and precipitates are often used interchangeably. In the context of this thesis, the term clusters will always be used to describe a collection of one or more defined elements within the crystal structure of the matrix that are in closer proximity to each other than they are within the surroundings of the cluster. In addition to clusters, precipitates have a defined crystal structure, form a phase boundary to the matrix, and have a defined morphology.

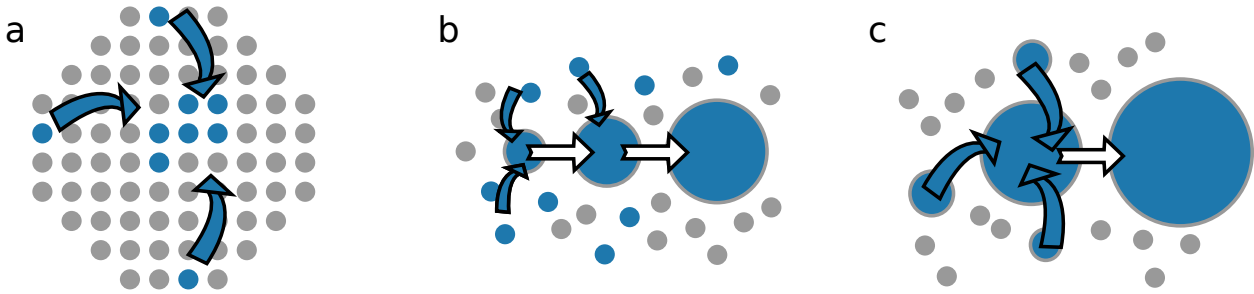


Figure 2.6: Overview of the life cycle of a precipitate. a) Formation of clusters from individual solute atoms. b) Growth of clusters and precipitate formation. c) Coarsening of larger precipitates to the detriment of smaller precipitates.

The cluster formation is the first stage in the life cycle of precipitates and occurs during the early stages of aging. The precipitating elements begin to diffuse and agglomerate near each other, however, they still remain part of the matrix microstructure [19]. The clusters already have an influence on the mechanical properties, because in this stage some maraging steels already show a significant strength increase [17, 53]. For maraging steels, Ti is known to be one of the very rapidly clustering elements [65]. Niu et al. [53] reported an ultimate tensile strength of 1134 MPa in the solution annealed condition of their maraging steel, and after an aging heat treatment for 15 min the strength increased to 2159 MPa. The same condition was also characterized using atom probe tomography, where they detected co-clusters of Ni and Ti [53].

At some point during the aging heat treatment the clusters begin to form their own crystal structure [19]. During this stage the precipitating solute elements continue to migrate toward the precipitates, leading to their growth. Within this stage, there exists an optimal configuration of precipitate number density, volume fraction, and size which corresponds to the peak hardness.

Continued aging after peak hardness is reached leads to the decline of the strength of the material and the stage of coarsening or over-aging is reached. The coarsening stage is characterized by the dissolution of smaller particles and the growth of larger particles. The driving force for this process is the minimization of the interfacial energy [66].

2.5.2 Precipitate-dislocation interactions

Precipitates act as an obstacle to the movement of dislocations, so when a dislocation comes into contact with a precipitate certain interaction mechanisms take place which define the strengthening effect of the particle.

To understand the strengthening effect of precipitates we first must distinguish between the different types of precipitate-matrix interfaces. Fig. 2.7 shows a schematic visualization of the coherent, semi-coherent, and incoherent precipitate-matrix interfaces. If the crystal structure of the precipitate and the matrix are the same, and if their lattice constants are similar the precipitate-matrix interface is coherent [67]. Within the coherent interface, the mismatch between the lattice constants of the precipitate and the matrix is accommodated by an elastic strain. If the lattice mismatch becomes larger a certain degree of coherency can be maintained by periodically introducing misfit dislocations. Such an interface is called semi-coherent [67]. For dislocations, a coherent interface means that they can propagate from the matrix phase through the precipitate while staying on the same glide plane, thus classifying them as shearable particles [67].

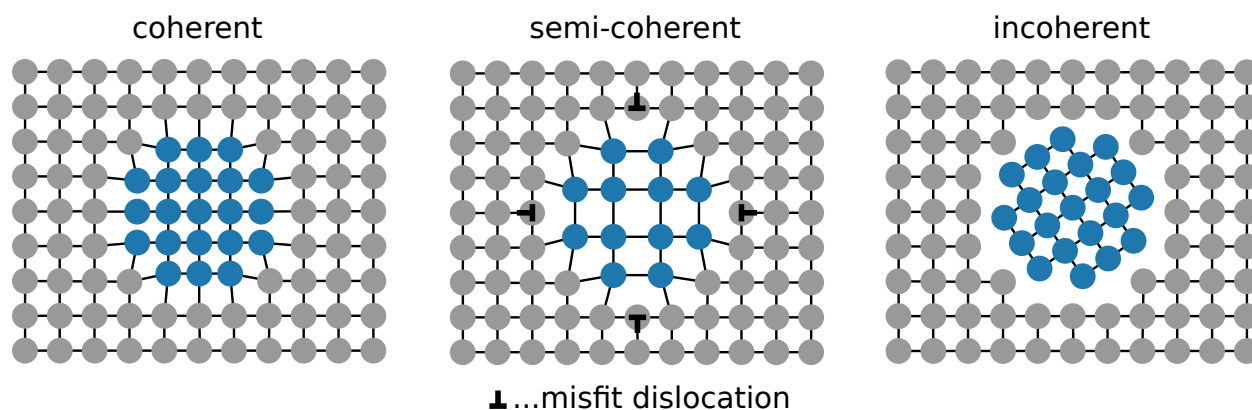


Figure 2.7: Schematic of the different types of matrix-precipitate interfaces: coherent, semi-coherent, and incoherent interfaces.

When a moving dislocation comes into contact with a shearable precipitate the dislocation first bows around the particle. As the bowing angle Ψ decreases from 180° (straight dislocation), the shear force acting on the dislocation increases until a critical angle (outer cut-off angle) Ψ_C is reached and the dislocation is able to move through the particle [68]. This critical angle is dependent on the dislocation character and the size and characteristics of the precipitate. As the dislocation moves through the particle it experiences stress fields from the coherency strain, differences in the elastic properties compared to the matrix, and a different stacking fault energy compared to the matrix [69]. Furthermore, if the particle has an ordered crystal structure the dislocations can only move in pairs through the particle. This is because the first dislocation destroys the ordered structure while the second dislocation repairs it. Coupled dislocations like these are called super-dislocations. The movement

of super-dislocations also leads to the formation of an anti-phase boundary between the dislocation pair [68].

For each dislocation that shears through a precipitate, the two halves of the precipitate are moved apart by the distance of one Burgers vector in relation to each other [67]. This leads to the formation of an additional interface area between the matrix and the precipitate [68]. In summary, the strengthening mechanisms of shearable particles can be summarized by the following effects [68, 70]:

- The coherency effect,
- the effect of elastic misfit,
- the effect from stacking fault energy differences,
- the formation of interface area and
- the formation of anti-phase boundaries for ordered particles.

For shearable particles the force equilibrium between a dislocation and a particle can be described by [68]:

$$\tau bL = 2T \cos\left(\frac{\Psi}{2}\right) \quad (2.3)$$

with

$$T(\Phi) = \frac{Gb^2}{4\pi} \left(\frac{1 + \nu - 3\nu(\sin \Phi)^2}{1 - \nu} \right) \ln\left(\frac{r_o}{r_i}\right) \quad (2.4)$$

In Equation 2.3 τ is the shear force acting on the particle, L is the distance along the dislocation between two particles, T is the dislocation line tension, Ψ is the bending angle of the dislocation, and b is the magnitude of the Burgers vector [68]. In the expression for the dislocation line tension T (Equation 2.4) G is the bulk modulus of the matrix phase, ν is the Poisson's ratio of the matrix phase, Φ is the angle between the line element of the dislocation and the Burgers vector, and r_o and r_i are the outer and the inner cut-off radius of the dislocation, respectively [68].

The third type of interface is the incoherent interface, where no common lattice plane can be shared, and instead, a phase boundary is formed which separates the matrix from the interface [67]. Since there is no continuous lattice between the matrix and precipitate it is not possible for dislocations to shear through the particle and instead bypasses the particle via the Orowan mechanism [67].

The Orowan mechanism describes that the moving dislocation bows around the particle, and since the particle can't be sheared the bowing angle decreases until it reaches zero. In this

configuration the two sides of the dislocation come into contact and annihilate each other (due to their opposing burgers vectors), leaving behind a closed dislocation loop around the particle [19, 67, 68]. The strengthening effect from the Orowan mechanism can be expressed as [68]:

$$\tau_{\text{Orowan}} = \frac{Gb}{2\pi\sqrt{1-\nu}L_s} \ln \frac{2r_s}{r_i} \quad (2.5)$$

In Equation 2.5 L_s is the mean surface-to-surface distance between precipitates and r_s is the mean radius of the precipitates [68].

It must be noted that shearable particles can also be bypassed by the Orowan mechanism if the bowing angle Ψ approaches 0 before the particle can be sheared.

2.6 The role of alloying elements

Ti Ti is a highly active alloying element for maraging steels and is responsible for the formation of Ti-rich precipitates such as Ni_3Ti at the beginning of aging treatments [43]. In Co-free maraging steels, Ti is also required to achieve high strengths, as the precipitation of Mo-rich phases appears to happen much slower. Thus Ti-rich precipitates are responsible for a large part of the precipitation hardening effect [43].

Co Cobalt increases the activity of Mo, lowers its solubility in the martensite matrix and so enhances the precipitation of Mo-rich phases [43]. Furthermore, Co increases the homogeneity of the precipitate dispersion by accelerating the precipitation process [71] and overall enhances the effectiveness of precipitation hardening [55].

Mo Mo is the main strength contributor in some maraging steels, as it is forming Ni_3Mo and Fe_2Mo precipitates during aging. Thuvander et al. [51] have shown that, in some alloys, Mo segregates to the interface between the precipitates and the matrix, forming a shell around the precipitate, and thus slows their coarsening at high aging temperatures. They [51] also found that out of three different alloys with 0.01, 1.2, and 2.3 at.% Mo this segregation effect was only observed in the 2.3 at.% Mo alloy, but both, the 1.2 at.% and 2.3 at.% samples slowed coarsening of Ni-rich phases. Finally, they [51] also found that a higher Mo concentration corresponds to a faster formation of Cu-rich clusters which act as nucleation sites for other precipitates [51].

Cr Generally, Cr is added to steel in order to improve corrosion resistance since Cr forms a stable and protective Cr_2O_3 layer. Although Cr is widely accepted to stabilize the α -ferrite phase, the addition of Cr to a maraging steel can lead to increased formation of reverted

austenite [43]. The Cr content seems to have a larger influence on the reversion than an increase of the aging temperature by 10°C [43]. Furthermore, it was observed by Mahmoudi et al. [54] that Cr leads to increased retention of austenite after quenching. Thuvander et al. [41] observed with APT measurements that Cr first segregates to the matrix-precipitate boundaries and then forms a Cr-rich α' -phase, which was first observed after 40 h of aging.

Cu It has been reported in several studies [13, 18, 51] that Cu leads to the formation of Cu-rich clusters in the early stages of aging [55]. Subsequently, these clusters act as nucleation sites for other types of precipitates [51], like β -NiAl and γ -Ni₃(Ti,Al) [13]. Schnitzer et al. [13] proposed that Cu accelerates the precipitation process, as Cu is a very fast segregating element in Fe and the quick formation of clusters, which act as a precursor for β -NiAl precipitates, promote shorter aging times compared to Cu-free maraging steels. The acceleration of β -NiAl is believed to be the result of Cu that solved in β -NiAl, where it decreases the lattice constant and reduces the misfit and the overall activation energy for nucleation of β -NiAl [13, 55].

Si Si is an impurity element that is often found in steels. It was shown by Thuvander et al. [41] that Si can migrate to γ' -Ni₃(Ti,Al,Si) type precipitates. After 100h it was observed that these precipitates have transformed into a G-type Ni₁₆Si₇Ti₆ phase. Furthermore, Si is known to decrease the formation time of laves phase precipitates [14].

2.7 Influence of deformation

Forging processes not only influence the microstructure of the matrix but also affect the kinetics of the precipitate formation. Generally, it can be distinguished between cold deformation, hot deformation, and severe plastic deformation (SPD) which presents a special case of deformation processes. While hot deformation takes place at temperatures above the recrystallization temperature, cold deformation takes place at lower temperatures [72].

Castro-Güiza et al. [8] studied the effect of warm deformation on the microstructure and mechanical properties of a C300 maraging steel. They performed compression tests with deformations of 30% and 60% at a temperature of 950°C and 1050°C. Their results revealed that the deformation led to a significantly reduced grain size and a higher fraction of reverted austenite. Furthermore, they found that for short aging times (1 h) the samples that were deformed showed a higher hardness than the undeformed samples. This effect was stronger for the 60% deformed samples than for the 30% deformed samples and got progressively weaker up to aging times of 10 h, where the measured hardness was equal for the deformed and the undeformed samples. The difference between a deformation temperature of 950°C and 1050°C was evident in the martensite grain size. While for 950°C the formation of

martensite from the work-hardened austenite led to a fine and homogeneous microstructure, at 1050°C the partial recrystallization led to some coarser-grained areas.

These results are in agreement with studies performed by Lian et al. [73] and Tian et al. [74] for a Co-free and Co-alloyed maraging steel, respectively. Both research groups addressed the effect of cold rolling on the microstructure and mechanical properties of their respective maraging steel. Lian et al. [73] found that the cold deformation leads to a refinement of the martensite microstructure. Both found that the peak hardness of their materials was shifted to shorter aging times with an increasing degree of deformation.

Severe plastic deformation (SPD) is a collective term for different metal-forming processes which introduce an extremely high degree of deformation into a sample. Typically SPD is used to create ultrafine-grained and nanocrystalline materials [75]. Commonly used processes include high-pressure torsion, equal channel angular pressing, and accumulative roll bonding. SPD leads to the formation of different types of non-equilibrium high-angle grain boundaries that provide a hierarchy of fast diffusion pathways [76].

During SPD the material undergoes five different stages with increasing grain refinement caused by the formation of dislocation cells structures and sub-grains [77]. During the final stage of SPD (steady-state stage), the grain refinement is balanced with dynamic recrystallization, which can take place at relatively low homologous temperatures (in contrast to hot deformation) [77].

In current literature, the effect of SPD on the precipitation kinetics and on the mechanical properties after aging heat treatments is not well established yet, specifically for Co-free maraging steels.

Materials and Characterization Methods

Within this thesis, multiple alloys with different deformation conditions were characterized. A large part of the research was conducted on experimental maraging steels with the goal to determine how the process-structure-property relationship changes with the addition and variation of the alloying elements.

The materials were characterized from micro- to nano-scale using standard characterization methods such as EBSD and XRD, but also the high-resolution methods APT and TEM were used. The following sections will explain how the alloy variations were selected, explain the severe plastic deformation method of high-pressure torsion, and will go into detail about how APT was used to characterize the precipitates that were present in the materials used in this thesis.

3.1 Investigated Material

The main goal of this thesis was to study the influence of the process parameters and of the alloying elements on the properties of Fe-12Ni type maraging steels. To achieve this, two types of materials were used: firstly an industrial maraging steel, that was forged into bars with 90 mm and 140 mm diameter, and secondly, six different model alloys that were selected to determine the effect of individual elements. The chemical compositions of the industrial alloy and the model alloys are shown in Table 3.1.

The development from model alloy 1 to model alloy 6 represents the addition of Ti, Al, Cr, and Mo to obtain an alloy with a similar chemical composition to the industrial alloy. Alloys 1 and 2 were selected to determine the strengthening effect of the η -Ni₃Ti and the β -NiAl phase, respectively. In alloy 3 Ti and Al were both added to investigate the combined effect of η -Ni₃Ti and β -NiAl. Finally, Cr and Mo were added to improve the corrosion resistance and also to investigate how they affect the precipitation of η -Ni₃Ti and β -NiAl and the

formation of reverted austenite.

Table 3.1: Nominal chemical composition (in wt.%) of the maraging steel alloys used in this thesis.

Alloy	Fe	Ni	Cr	Mo	Ti	Al	C
Industrial	bal.	12.3	10.2	2.0	1.2	1.5	<0.03
Model 1	bal.	12			1		<0.03
Model 2	bal.	12				1.5	<0.03
Model 3	bal.	12			1	1.5	<0.03
Model 4	bal.	12	10		1	1.5	<0.03
Model 5	bal.	12	10		1.5	1	<0.03
Model 6	bal.	12	10	2.0	1.2	1.3	<0.03

3.2 High-pressure torsion

High-pressure torsion (HPT) is a deformation method that is classified as an SPD method, which is able to produce very large plastic strains in materials without causing a macroscopic fracture. Due to the high degree of deformation that is obtained by SPD many defects, such as dislocations and vacancies, are introduced into the crystal lattice [76, 78]. Furthermore, SPD methods have been used successfully to create ultra-fine-grained and nano-sized materials in many cases for a variety of materials [79–81].

HPT is performed by inserting a disk-shaped sample between two anvils which build up an isostatic pressure of a few GPa [82]. One of the anvils is connected to a motor that rotates the anvil at a certain speed around its own axis, and in the process of the rotation, the sample is twisted which generates a high degree of plastic deformation. The strain γ is dependent on the position of the sample [80]: $\gamma = \frac{2 \cdot \pi r}{t} \cdot n$ with r being the radius of the sample, t its thickness and n the number of rotations.

Since the degree of deformation in an HPT disc is varying locally the degree of grain refinement can also be homogeneous [82]. The homogeneity is dependent on the applied pressure and the material and can be determined with micro-hardness measurements across the disc surface [82].

3.3 Atom Probe Tomography

3.3.1 Technical background

Atom probe tomography (APT) is a characterization method with near atomic resolution that allows the creation of a 3-dimensional representation of a material at the nano-scale.

APT is not only a tool to observe microstructural features, but it is also a spectroscopy tool [83]. This means that we can accurately describe the chemical composition of the smallest microstructural constituents such as precipitates.

For the work in this thesis, an Imago LEAP 3000X HR (LEAP 3000) atom probe tomography microscope was used. This microscope allows measurements in the pulsed voltage mode and the laser-assisted mode, which uses a laser wavelength of 532 nm. The detector efficiency of the LEAP 3000 is 37% and the specimen temperature can be set to values between 20 K and 70 K.

Fig. 3.1 shows the basic principle of a LEAP. APT uses needle-shaped samples with very small tip radii (< 100 nm), which is necessary to create a sufficiently large electric field. The sample is placed in a special holder, inserted into an ultra-high vacuum environment ($< 10^{-7}$ Torr [84]) and is transferred to the analysis chamber, which had a vacuum of $< 10^{-10}$ Torr for the LEAP 3000 microscope used for this thesis. Afterward, the sample is placed into a specimen stage which is cooled to cryogenic temperatures of < 70 K using a closed-cycle He cryostat [85].

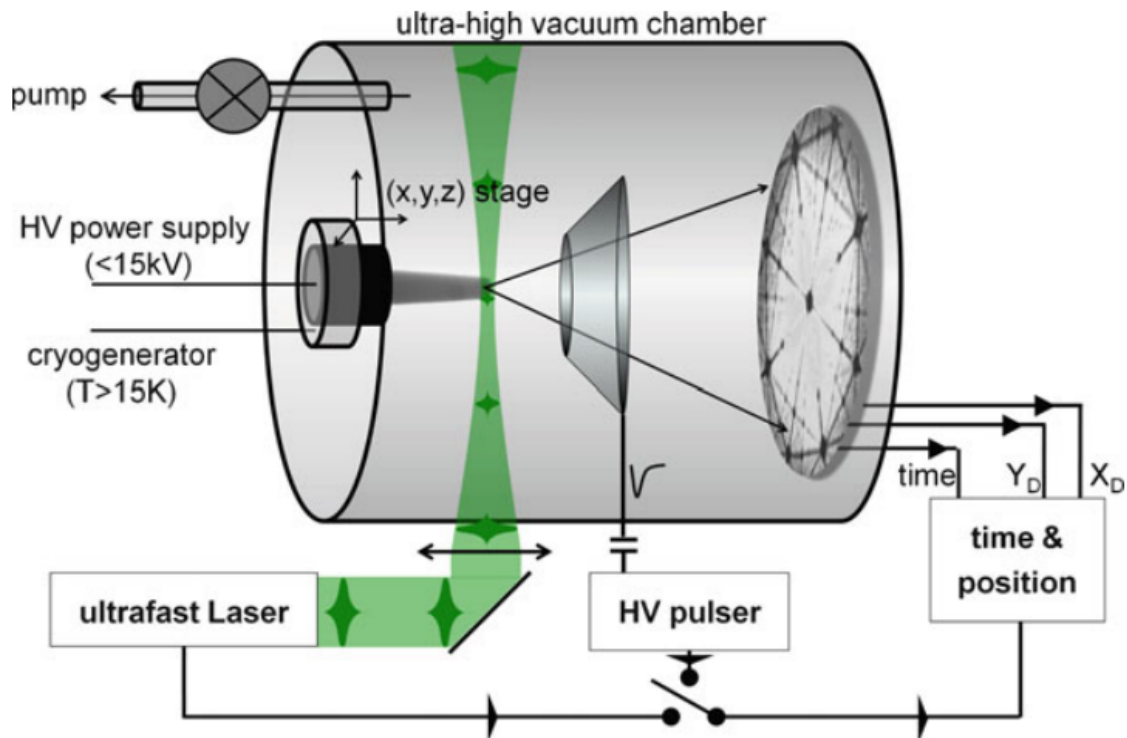


Figure 3.1: Experimental setup of a local electrode atom probe tomography microscope. Reprinted with permission from [85].

A local electrode separates the specimen from the detector. The local electrode is connected to the negative pole of the voltage supply and the specimen is connected to the positive pole.

When the measurement is started a bias voltage V is applied. This bias voltage creates a high electric field E at the apex of the specimen according to [86]:

$$E = \frac{V}{kr}$$

Where r is the radius of the specimen tip and k is a factor that accounts for the reduction of the electric field due to the shank angle and the material behind the tip [86]. In addition to the bias voltage also voltage pulses (15% to 25% of V) or laser pulses are applied with a well-defined pulse frequency. The pulse frequency defines the time intervals between evaporation events. During these intervals the evaporated and positively charged ions are accelerated towards the local electrode, fly through its aperture, and hit the position-sensitive detector [83]. The time between the last pulse and the detection event is used to calculate the time of flight of the ion. The attractive force towards the local electrode is a function of the charge state of the ion and the acceleration is a function of the ion mass which means that the mass-to-charge ratio is uniquely identified by the time of flight [86]. For the chemical analysis, the mass-to-charge ratio is plotted in a frequency histogram (mass spectrum), and by consulting the natural abundances of isotopes it is possible to identify each element within the mass spectrum [83].

The detector of an APT microscope is position-sensitive and gives information about the x - and y - position where an ion hit the detector. However, the z -position of the ion is determined by the evaporation sequence during the reconstruction of the measurement data [85].

It was explained how the mass-to-charge ratio and the x -, y - and z -position are measured. These 4 values are sufficient information to generate a 3-dimensional representation of the measured specimen, start the reconstruction process and characterize the material.

3.3.2 Precipitate Characterization

The main challenge of precipitate characterization with APT is to separate the precipitates from the matrix data set which can be achieved by 2 basic approaches. The first approach is to define so-called iso-concentration surfaces (iso-surfaces). These iso-surfaces separate a side with a higher concentration (or density) from a side with a lower concentration. The threshold concentration value is dependent on the chemical composition of the precipitate and the matrix phase, and generally, a concentration gradient can be observed across the precipitate-matrix interface. Iso-surfaces can be very useful to analyze the chemical composition within a precipitate and as a tool to visualize the precipitate morphology, as shown by other authors for a variety of materials [52, 87, 88].

The second approach is a so-called cluster analysis. A cluster itself can be defined as an intrinsic association of one or more solute atoms [85], and one strength of APT is the ability

to detect small clusters of only a few solute atoms due to the near-atomic spatial resolution [83]. In current literature, the term cluster and precipitate are often used interchangeably, but a reasonable distinction is that clusters can be seen as agglomerations of solute atoms within the matrix crystal structure while precipitates have their own crystal structure.

The most widely used cluster detection algorithms are the maximum separation method (MSM) and the DBSCAN algorithm. Both algorithms are based on the assumption that the density of solute atoms is higher in a cluster than in the surrounding matrix [85]. The maximum separation method searches for the nearest neighbor solute atom (neighbor) for each solute atom (central atom), and if it is within a certain threshold distance d_{Max} the two atoms belong to a cluster. In the next step, all clusters that are within d_{Max} to each other are linked to each other so that a final cluster is obtained.

The next advancement of the MSM is the DBSCAN algorithm which searches for higher order neighbors [85], e.g the 4th-nearest neighbor. Also with the DBSCAN algorithm, the neighbor must be within a threshold distance d_{Max} to the central atom so that the central atom and the neighbor are linked as a cluster. The DBSCAN algorithm has the advantage that clusters are more easily identified when the solute concentration is high, which can mean that the first nearest-neighbor distance in the matrix and within the precipitate is similar. With a higher neighbor order this problem can be minimized. Furthermore, the effect of density fluctuations can be minimized [85].

The key to a meaningful cluster analysis is to use the correct parameters. For the DBSCAN algorithm, three parameters are necessary: the maximum separation distance d_{Max} , the neighbor order k , and the minimum cluster size N_{Min} . Out of these parameters, d_{Max} is the most crucial one and should not be chosen arbitrarily. Instead, the literature offers scientific approaches which can be used to determine d_{Max} . For instance, Stephenson et al. [89] and Jäggle et al. [90] proposed strategies based on the approximation of the nearest-neighbor distribution using a complete spatial randomness (CSR) model. The strategy proposed by [89] was implemented and used successfully for this thesis.

Relation of the current thesis to the state of the art

With the goal to reduce the environmental impact of the steel production the use of recycled material becomes more and more important. As such it is crucial to know how changes in the chemical composition (e.g. Ti and Al variations) affect the mechanical properties of the manufactured parts.

Many commercially available Co-free maraging steels employ an alloying strategy that provides only one type of intermetallic phase that is used for strengthening. The alloys in this thesis will focus on the development and improvement of a maraging steel which is strengthened by two types of intermetallic phases, firstly the β -NiAl phase and secondly the η -Ni₃Ti phase. In the current literature, it is not well established how changes of the Ti and Al concentrations affect the relationship between the β -NiAl and η -Ni₃Ti phases and their relative strengthening effect and how the elements that are added for corrosion resistance (Cr and Mo) change the precipitation kinetics.

The industrial maraging steel used in this thesis is intended for the closed-die forging of high-performance parts. During forging the material is deformed by several different degrees over the whole part. The local deformation depends on the geometry of the part before forging and the desired end geometry after forging and affects the local grain size and dislocation density. These local microstructural differences not only can make a difference to the mechanical properties, but also to the precipitation of the intermetallic phases. Furthermore, the manufactured structures can be made up of parts with thicker and thinner wall-thickness which affects the local heating and cooling rates during heat treatments. Both, the influence of high degrees of deformation and the influence of the cooling rate after aging are currently not well established in the literature for Co-free maraging steels.

This thesis addresses the influence of the elements Ti, Al, Cr, and Mo on the microstructure

as well as the influence of high degrees of deformation and of the cooling rate after the aging heat treatment for a corrosion-resistant Co-free maraging steel and works on establishing their process-structure-property relationship. To achieve this goal mechanical characterization and high-resolution characterization methods were performed and strengthening models were used to quantify the precipitation hardening.

Published Content

Publications as first author

Publication I: *Precipitation behavior of a Co-free Fe-Ni-Cr-Mo-Ti-Al maraging steel after severe plastic deformation*

S. Zeisl, A. Lassnig, A. Hohenwarter, F. Mendez-Martin
Materials Science and Engineering: A **833**, 142416 (2022)

Publication II: *Cooling rate controlled aging of a Co-free Fe-Ni-Cr-Mo-Ti-Al maraging steel*

S. Zeisl, R. Schnitzer
Metals **12**(4), 538 (2022)

Publication III: *The role of alloying elements in NiAl and Ni₃Ti strengthened Co-free maraging steels*

S. Zeisl, A. Landefeld, N. Van Steenberge, Y. Chang and R. Schnitzer
Materials Science and Engineering: A **861**, 144313 (2022)

Publication IV: *Strengthening effect of NiAl and Ni₃Ti precipitates in Co-free maraging steels*

S. Zeisl, N. Van Steenberge, and R. Schnitzer
Manuscript under review for *Journal of Materials Science* (2023)

Publications as contributing author

From microscopic to atomistic scale: Temperature effect on yttria distribution in mechanically alloyed FeCrMnNiCo powder particles

M. Mayer, J. Svoboda, F. Mendez-Martin, S. Fellner, C. Gammer, V. Razumovskiy, W. Sprengel, A. Stark, S. Zeisl and G. Ressel

Manuscript under review for *Materials and Design*

Phase stability of TiAlXYZ BCC high entropy alloys

L. Hatzenbichler, S. Zeisl, H. Clemens and D. Holec

Manuscript under review for *Intermetallics*

Publication I

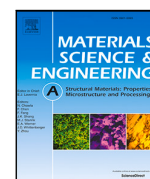
Precipitation behavior of a Co-free Fe-Ni-Cr-Mo-Ti-Al maraging steel after severe plastic deformation

S. Zeisl, A. Lassnig, A. Hohenwarter, F. Mendez-Martin
Materials Science and Engineering: A **833**, 142416 (2022)



Contents lists available at ScienceDirect

Materials Science & Engineering A

journal homepage: www.elsevier.com/locate/msea

Precipitation behavior of a Co-free Fe-Ni-Cr-Mo-Ti-Al maraging steel after severe plastic deformation

S. Zeisl^{a,*}, A. Lassnig^b, A. Hohenwarter^a, F. Mendez-Martin^a^a Department of Materials Science, Montanuniversität Leoben, Franz Josef Straße 18, 8700 Leoben, Austria^b Erich Schmid Institute of Materials Science, Austrian Academy of Sciences, Jahnstraße 12, 8700 Leoben, Austria

ARTICLE INFO

Keywords:

Atom probe tomography
Severe plastic deformation
Maraging steels
Intermetallics
Precipitation hardening

ABSTRACT

Maraging steels are martensitic steels that are strengthened by the precipitation of nano-sized intermetallic phases. Severe plastic deformation is known to influence diffusion, stability and properties of metallic materials. The goal of this study is to reveal the influence of severe plastic deformation on the hardness and the precipitation behavior of a Co-free maraging steel. For this study the as-quenched material was deformed with high-pressure torsion. Afterwards, a series of heat treatments were conducted. The hardness increase was measured and correlated with micro-to-nanoscale microstructural characteristics, focused on the precipitate characterization with atom probe tomography. Severe plastic deformation transformed the microstructure to a globular microstructure, delayed and minimized austenite reversion as well as accelerated and influenced the precipitation reaction, affecting the size, morphology and type of intermetallic phases.

1. Introduction

Maraging steels belong to the group of ultra-high strength steels. With ultimate tensile strengths up to 2.5 GPa, they are used for applications where high strength and good fracture toughness are needed [1, 2]. Applications for these types of alloys are typically in the fields of aerospace, automotive and machinery [1,3]. Maraging steels achieve their high strength due to the hardening effect of nano-sized precipitates. These precipitates are formed from elements such as Ni, Ti, Al or Mo during an aging heat treatment [1,4,5] at temperatures around 500 °C. Precipitation hardening was discovered in the early 1900s and today it is an important mechanism for increasing the strength of materials [6]. The strengthening effect stems from the role of the precipitates as obstacles for the movement of dislocations. Because of this, dislocations cannot freely pass the particles but they must overcome them using either the shearing or the bowing (Orowan) mechanism [6]. The strengthening effect depends on physical properties such as the coherency of the precipitates, their size and their distribution within the matrix but also on the elastic properties and anti-phase boundary energy [6,7]. In Co-free maraging steels the most well-known intermetallic phases are the β -NiAl (B2 structure) and η -Ni₃Ti (D0₂₄ structure) [8] phases. Other phases such as the G- and R'- and 9R-phase have been observed as well, after prolonged annealing [9, 10]. The β -NiAl and the η -Ni₃Ti phases are often reported showing a spherical and rod-like morphology respectively [2,9]. The β -NiAl and η -Ni₃Ti precipitates in maraging steels are (semi-)coherent with

the martensite matrix [1,11], thus both the bowing and the cutting mechanism are contributing to the strengthening effect. The martensitic matrix of maraging steels consists of a hierarchy of packets, blocks and laths with laths being the smallest structure. The martensite laths are typically 100–300 nm in thickness, however, for grain size strengthening the block size can be considered as the strength controlling length scale [12,13].

Hot deformation in the austenitic state was shown to lead to refinement of the martensitic matrix and to decreased block sizes [12,14] but also to a precipitation hardening response at shorter aging times and increased austenite reversion [14]. The effect of cold deformation on the microstructure and mechanical properties was studied by Lian et al. [15]. They found that cold rolling leads to a shift of the peak hardness to shorter aging times. A comparison between the aged undeformed and an aged cold rolled material (with 45% reduction in thickness) allowed them to show that static recovery was responsible for a 10 HV to 17 HV hardness decrease. Severe plastic deformation (SPD) has been used frequently over the last decades to achieve materials with ultrafine-grained and nanocrystalline microstructure [16–18]. The nanocrystalline structure, especially the high dislocation density and grain boundary fraction, of SPD material can lead to an increased rate of diffusion, particularly grain-boundary and pipe diffusion [19, 20]. SPD performed on bcc materials, such as as-quenched maraging steels, can lead to a refinement of the microstructure and sub-grain

* Corresponding author.

E-mail address: stefan.zeisl@unileoben.ac.at (S. Zeisl).<https://doi.org/10.1016/j.msea.2021.142416>

Received 20 August 2021; Received in revised form 24 November 2021; Accepted 25 November 2021

Available online 11 December 2021

0921-5093/© 2021 The Authors. Published by Elsevier B.V. This is an open access article under the CC BY license (<http://creativecommons.org/licenses/by/4.0/>).

sizes of tens of nanometers in combination with a substantial increase of strength [21].

The aim of this study is to show the influence of SPD on the microstructure and precipitate evolution of a Co-free maraging steel. The direct comparison of the SPD material with a reference material should reveal if a positive effect on the precipitation strengthening effect can be achieved.

2. Material and methods

The material was produced by vacuum induction melting followed by vacuum arc remelting to ensure a homogeneous ingot with high purity. The chemical composition of the alloy is listed in Table 1. The ingot with 500 mm diameter was then forged at 1250 °C to a bar with a diameter of 140 mm. The bar was solution annealed at 850 °C for 90 min, water-quenched and cryogenically treated at -80° C for 16 h (SA+Q condition). A 10 mm thin slice was cut off for sample preparation. Disk shaped samples with a diameter of 30 mm and a thickness of 5 mm were cut out using water-jet cutting and abrasive cutting. All samples were cut out from half-radius of the bar slice. These specimen disks were used as reference material and to perform SPD. For SPD the high-pressure torsion (HPT) method was used. In this process the sample is placed between two rotating anvils and subjected to high hydro-static pressures [22]. HPT was performed in the SA+Q condition using a pressure of 5 GPa and a rotational speed of 0.2 RPM for 10 revolutions. Aging of the reference and HPT material was carried out at 500 °C for times of 5 min, 60 min, 240 min and 960 min in a Carbolite RHF 750 convection oven. The samples were immediately quenched in water after removal from the oven. Metallographic samples for hardness testing, light optical microscopy (LOM), scanning electron microscopy (SEM) and X-ray diffraction (XRD) were prepared by standard polishing methods to a final surface roughness of about 1 µm. The SEM samples were finished by electrolytic polishing using a Struers Lectropol-5 machine and a Struers A2 electrolyte. Transmission electron microscopy (TEM) samples and samples for transmission Kikuchi diffraction (TKD) were prepared by twin-jet polishing using a Struers A2 electrolyte. Hardness testing was performed with all samples, the samples with 5 min, 60 min and 960 min aging time were selected for microstructural characterization.

The Vickers hardness was measured using a Zwick hardness testing machine and a load of 5 kg. The hardness was determined by using the average of at least five measurements for each sample. The matrix of the reference material was characterized with LOM using a ZEISS EVO optical microscope using bright field imaging. XRD was performed to measure the austenite fraction. A Bruker-AXS D8 Advance diffractometer with Cu-K α radiation, an acceleration voltage of 40 kV and a current of 40 mA was used. The austenite fraction was calculated using the MAUD software package [23]. The as-HPT matrix phase was characterized with SEM using a TESCAN Clara microscope. TKD was carried out to characterize the matrix phase of the aged HPT material using a ZEISS LEO 1525 microscope at 30 kV and an EBSD detector from Bruker (eFlash FS) equipped with an on-axis TKD detector head. TEM was performed with a JEOL 2200 FS microscope and selected area diffraction (SAD) was used to confirm the crystal structure of the precipitates.

Atom probe tomography (APT) was performed for statistical and chemical characterization of precipitates using a CAMECA IMAGO LEAP 3000 X HR microscope. The fine needle-shaped tips for APT were prepared by a standard 2-step electropolishing method [24]. Matchstick samples with a cross-section of $0.5 \times 0.5 \text{ mm}^2$ and a length of about 10 mm were first thinned with a solution of 25 vol% of perchloric acid in glacial acetic acid until a fine tip was formed. The final electropolishing step was performed with a 2% solution of perchloric acid in 2-butoxyethanol until a fine neck was formed and further polished until separation occurred. The samples were measured using the laser assisted mode with a laser energy of 0.3 nJ, a pulse rate of 250 kHz and

Table 1

Chemical composition of the maraging steel used in this study.

	Fe	Ni	Cr	Mo	Ti	Al	C
wt.%	bal.	12.3	10.2	2.0	1.2	1.5	<0.03
at.%	bal.	12.6	10.8	1.2	1.4	3.1	<0.14

a specimen temperature of 60 K at a detection rate of 0.5%. The APT measurements were analyzed using the CAMECA IVAS 3.6 software package. The statistical (number density N_V , volume fraction V_f and mean diameter \bar{d}_3) and chemical evaluation of clusters and precipitates was performed with a cluster analysis using the maximum separation method. For NiAl-type precipitates Al was used as central atom of the cluster search and for Ni₃(Ti,Al)-type precipitates Ti was used. The parameter d_{Max} for the maximum separation method was determined using a procedure described by Jäggle et al. [25]. The parameter N_{Min} was determined by with the aid of a cluster size distribution using the value for d_{Max} that was determined in the earlier step. For the envelope and erosion distance a value equal to d_{Max} was used. All parameters used for each condition and precipitate type is shown in Table 2. The evaluation of the precipitate and cluster mean diameter has been performed by transformation of the clusters into best-fitting ellipsoids. The volume fraction of the precipitates was calculated according to Eq. (1) by the number of ions found within the clusters corresponding the precipitate phase N and by the volume per atom that corresponds to the unit cell of the precipitate phase v divided by the volume of the reconstructed atom probe measurement V_{total} . The constant C acts as a factor that takes the detector efficiency of the instrument into account.

$$V_f = \frac{N \cdot v \cdot C}{V_{\text{total}}} \quad (1)$$

The chemical analysis of the precipitates and the matrix was performed using the IVAS feature of peak decomposition to account for the overlap of peaks (54-Fe²⁺, 27-Al⁺ and 54-Cr²⁺) in the mass spectrum. The chemical composition of the matrix was determined with the aid of iso-concentration surfaces. The precipitates were iteratively removed from the dataset using Ni+Al+Ti iso-concentration surfaces until a random first-nearest neighbor distribution of Al ions was observed.

3. Results

After the HPT process the sample had a thickness (t) of 4.5 mm. After 10 revolutions (n) this corresponds to a maximum shear strain (γ_{max}) of about 210 at the radius (r) of 15 mm, according to Eq. (2).

$$\gamma_{\text{max}} = \frac{2 \cdot \pi r}{t} \cdot n \quad (2)$$

The average hardness along the radius of the as-deformed (as-HPT) disk was 594 HV5. Compared to the hardness in the SA+Q reference material (324 HV5) this corresponded to a hardness increase of 270 HV5. All of the annealed HPT samples showed an increase in hardness, compared to the as-HPT condition, after aging for 5 min, 60 min, 240 min and 960 min. The hardness of the reference material also increased after the same aging conditions. The hardness and the hardness increase after the aging heat treatments is displayed in Fig. 1.

The reference sample showed a fine martensitic microstructure in the SA+Q condition (Fig. 2a). XRD measurements revealed (see Fig. 3) that the reference material contains austenite in all heat treatment states. The evolution of the austenite content is displayed in Fig. 4. The SA+Q condition of the reference material contained 6% austenite. The austenite fraction increased to 23% and 27% after aging for 5 min and 60 min and decreased to 14% after 960 min. The HPT material showed a globular microstructure with an average grain size of 152 nm in the as-HPT condition (Fig. 2b). The HPT material was austenite free in the as-HPT condition and in the conditions aged for 5 min and 60 min. Reverted austenite was first identified after 960 min of aging in the

Table 2
Parameters for the maximum-separation-method used for cluster detection for each condition and type of cluster or precipitate.

Material	Condition	Precipitate	Center element	Order	d_{Max} (nm)	N_{Min}
Reference	510 °C/5 min	NiAl cluster	Al	4	0.80	50
Reference	510 °C/60 min	NiAl	Al	4	0.83	50
Reference	510 °C/960 min	NiAl	Al	4	0.76	100
Reference	510 °C/960 min	Ni ₃ (Ti,Al)	Ti	4	1.01	2000
HPT	510 °C/5 min	NiAl cluster	Al	4	0.79	50
HPT	510 °C/60 min	NiAl	Al	4	0.79	50
HPT	510 °C/60 min	Ni ₃ (Al,Ti)	Ti	4	0.96	1000
HPT	510 °C/960 min	NiAl	Al	4	0.70	100
HPT	510 °C/960 min	Ni ₃ (Al,Ti)	Ti	4	0.96	1000

Table 3
Chemical composition (in at.%) and the Ni to Ti+Al ratio (in %) of the clusters and precipitates found in the aged reference (REF) and HPT material.

Condition	Precipitate	Fe	Ni	Ti	Al	Cr	Mo	Ni:(Ti+Al)
REF + 5 min	Cluster	51.3	11.6	2.7	26.4	7.3	0.6	29:71
REF + 60 min	Ni(Al,Ti)	48.0	14.3	3.4	27.0	6.6	0.6	32:68
REF + 960 min	Ni(Al,Ti)	44.1	24.1	3.9	21.2	5.9	0.5	49:51
	Ni ₃ (Ti,Al)	32.7	39.8	12.8	8.1	5.4	0.7	66:34
HPT + 5 min	Cluster	53.7	14.5	2.5	20.7	7.7	0.7	38:62
HPT + 60 min	Ni(Al,Ti)	49.2	16.4	3.2	23.6	6.9	0.5	38:62
	Ni ₃ (Al,Ti)	33.7	38.4	12.8	8.4	5.7	0.7	64:36
HPT + 960 min	Ni(Al,Ti)	49.2	16.4	3.2	23.6	6.9	0.5	38:62
	Ni ₃ (Al,Ti)	14.0	56.7	13.7	12.2	2.6	0.6	69:31

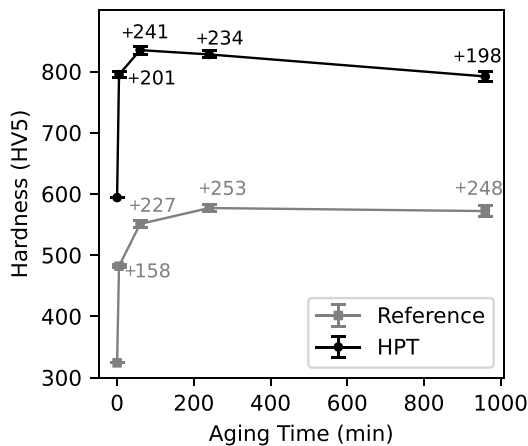


Fig. 1. Hardness of the reference and HPT material for different aging durations at 500 °C. The hardness increase compared to the conditions before aging is displayed as text.

HPT material (see Fig. 3,4). The austenite fraction in this condition was 5%.

TEM micrographs of the reference material (Fig. 5a,b) in the aged condition (500 °C for 960 min) confirmed the martensitic microstructure. Furthermore, precipitates with rod-like morphology were observed. A selected area diffraction (SAD) measurement (Fig. 5c) revealed that the rod-like precipitates correspond to a η -Ni₃(Ti,Al) phase [26]. Fig. 6a and 6b show the microstructure of the aged (500 °C for 960 min) HPT material. Using TKD a globular microstructure with an average grain size of 151 nm was observed in this condition. The results from SAD (Fig. 6c–d) showed reflections corresponding to the martensite matrix and overlapping reflections from the austenite phase and a γ' -Ni₃(Al,Ti) phase with L1₂ (ordered face-centered cubic) structure. Furthermore, a superlattice reflection corresponding to the γ' -Ni₃(Al,Ti) phase was identified at $k = 3.94 \text{ nm}^{-1}$.

Fig. 8a–c display the clusters and precipitates found in the aged conditions of the reference material. After 5 min of aging clusters rich in Al were found. Small spherical precipitates were observed after

60 min of aging. The Ti and Ni content of these spherical precipitates increased compared to the clusters in the condition after 5 min of aging. From the chemical composition this phase was identified as an early stage of the β -NiAl phase. After an aging time of 960 min a homogeneous distribution of spherical β -NiAl precipitates was observed in the reference material, furthermore rod-like η -Ni₃(Ti,Al) precipitates were observed. The precipitate evolution of the HPT material is displayed in Fig. 8d–f. The condition aged for 5 min shows clusters rich in Al and Ni. In the condition aged for 60 min two types of precipitates were observed, small spherical β -NiAl precipitates and larger and round γ' -Ni₃(Al,Ti) precipitates. After an aging time of 960 min both types of precipitates in the HPT material showed growth and similar phase chemistry compared to the condition aged for 60 min (see Table 3). Furthermore, precipitate free regions were observed in this condition (see Fig. 8f).

The evolution of the precipitate number density, volume fraction and mean diameter are displayed in Fig. 9. In the reference material the number density of the β -NiAl phase increased between 5 min and 60 min of aging, when compared to the number density of the clusters, but decreased after 960 min aging time. The volume fraction and the mean diameter of β -NiAl increased between 60 min and 960 min aging time. The volume fraction of η -Ni₃(Ti,Al) was lower than the volume fraction of the β phase. In the HPT material the evolution of the number density of β -NiAl showed a similar trend to the β phase in the reference material. The number density of the γ' -Ni₃(Al,Ti) phase remained constant between 60 min and 960 min aging time. The volume fraction of the γ' phase increased between 60 min and 960 min aging time, while the β phase remained at similar volume fractions. The mean diameter of the β -NiAl phase increased between 60 min and 960 min of aging, however the increase was smaller than in the reference material.

The chemical composition of the matrix phase is displayed in Fig. 7. The reference and the HPT material showed similar trends for the Ti, Al, Cr and Mo concentrations with respect to the aging time. In contrast, the Ni concentration is higher in the HPT material after 5 min than in the reference material with the same aging condition. After 60 min aging time the Ni concentration in the reference material remains stable while in the HPT material a decrease can be observed. In the 960 min aged condition both materials had a similar Ni concentration in the matrix.

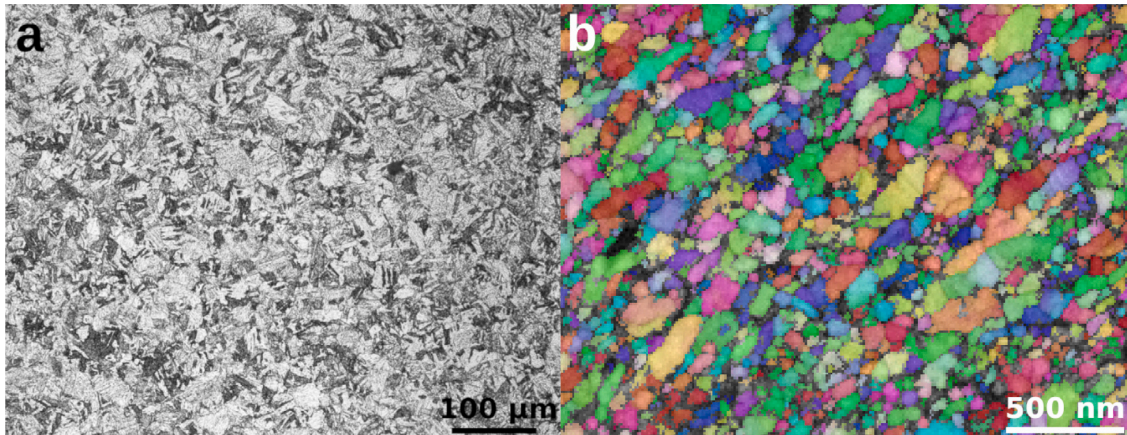


Fig. 2. (a) LOM brightfield micrograph showing the martensitic microstructure of the reference material in the SA+Q condition. (b) TKD IPF-Z map showing the fine-grained microstructure of the HPT material in the as-HPT condition.

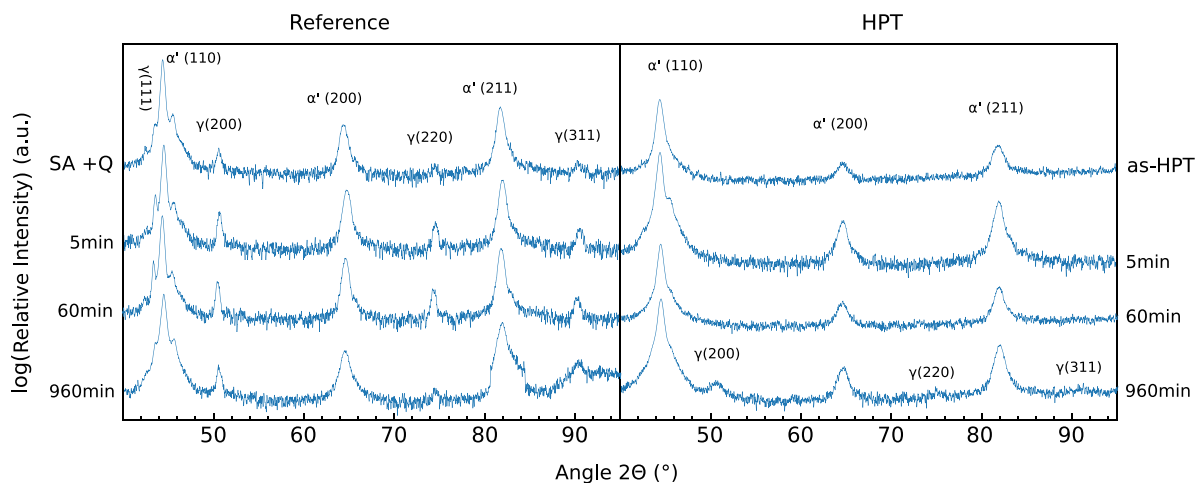


Fig. 3. XRD diffractograms of the reference material and the HPT material in the SA+Q/as-HPT condition and the 5 min, 60 min and 960 min aged conditions.

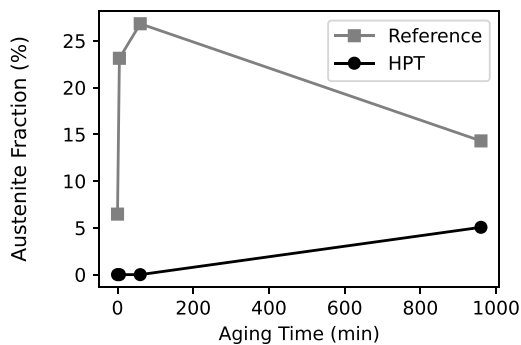


Fig. 4. Austenite fraction as function of the aging time at 500 °C of the reference and HPT material.

The grain boundary area of the aged HPT material was investigated within the regions of interest defined in Fig. 10. The corresponding one-dimensional concentration profiles of Mo are presented in Fig. 11. All three heat treatment states showed an enrichment of Mo at the grain

boundaries starting at 2% after 5 min aging time and stabilizing at 3.5% after aging for 60 min.

4. Discussion

HPT led to a change in microstructure from a martensitic structure in the reference material to a globular structure with grain sizes ranging from 25 nm to 325 nm in the HPT material. The transformation of the microstructure is accompanied by an increase in high-angle grain boundary surface area. As a consequence, the kinetics of diffusion processes at grain boundaries can be assumed to be accelerated [19,20]. Between the as-HPT condition and the condition aged for 960 min no grain growth could be observed, which is in agreement with measurements performed by Jacob et al. [27] on a HPT deformed Co-alloyed maraging steel.

APT measurements and cluster analysis of the aged material revealed that there is a clustering effect after 5 min for the HPT material and the reference material. The clusters formed in the reference material are more numerous, smaller and more homogeneously distributed than in the HPT material. After 60 min aging time the reference material shows precipitates that correspond to an early stage of β -NiAl, while two types of precipitates were observed in the HPT material. One precipitate phase corresponds to a β -NiAl phase, while the second phase

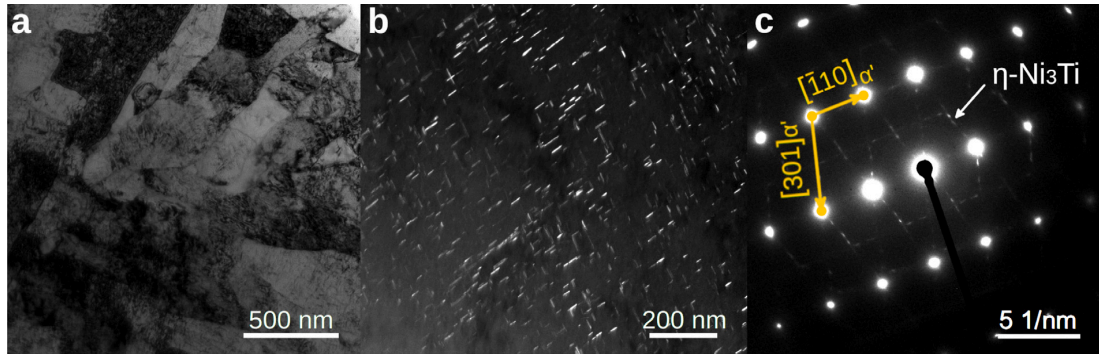


Fig. 5. Microstructure of the reference material after aging at 500 °C for 960 min. (a) TEM bright field micrograph of the martensitic structure, (b) TEM dark field image showing the rod-like η -Ni₃Ti precipitates and (c) SAD pattern showing the matrix phase (bright spots) and the η -Ni₃Ti (streaks) precipitate phase.

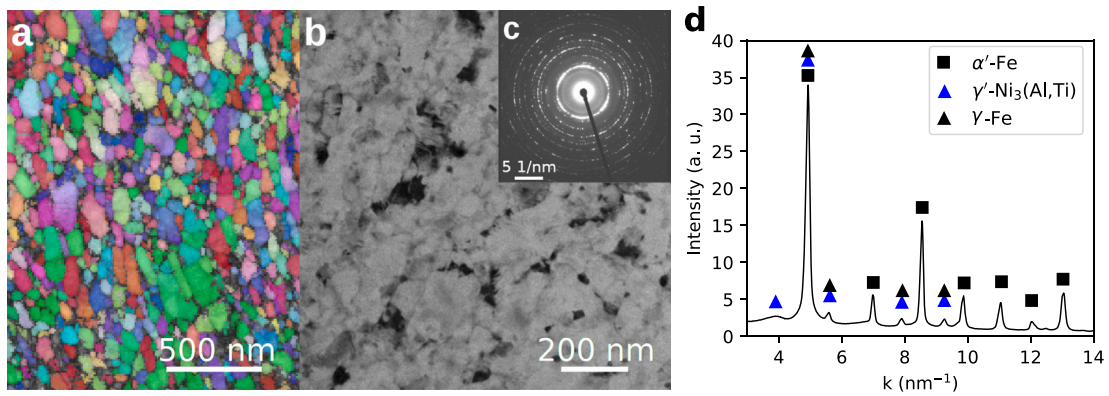


Fig. 6. Microstructure after HPT deformation and an aging heat treatment at 500 °C for 960 min. (a) TKD IPF-Z map, (b) TEM bright field micrograph, (c) SAD pattern corresponding to (b) and (d) integrated intensity of the SAD pattern.

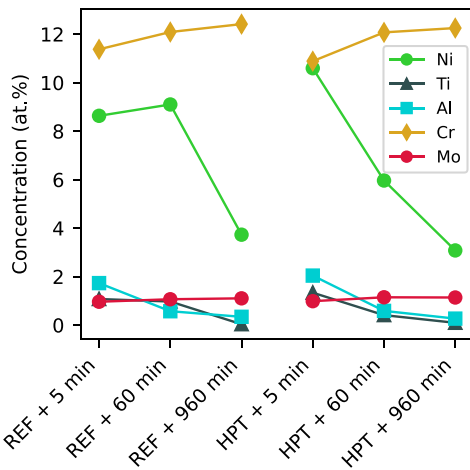


Fig. 7. Concentration (in at.%) of Ni, Ti, Al, Cr and Mo within the matrix phase for all aged conditions.

corresponds to a γ' -Ni₃(Al,Ti) phase, as confirmed with SAD measurements of the 960 min aged condition. In both materials, the reference and the HPT material, the mean diameter of the NiAl-type precipitates after 60 min of aging is smaller than the cluster size after 5 min of aging. For the HPT material this difference stems from the combination

of large and small clusters in the 5 min aged condition. The difference for the reference material can be explained by experimental scattering and parameter selection. After 960 min of aging a second phase that is rod-like in morphology and corresponds to a η -Ni₃(Ti,Al) phase was observed in the reference material. In the HPT material the γ' -Ni₃(Al,Ti) grew after 960 min of aging, leading to an increase in volume fraction. The mean diameter of the β -NiAl precipitates increased in both types of material. This growth is more pronounced in the reference material than in the HPT material.

In the condition aged for 5 min Al is the main element that contributes to clustering in the reference material. The clusters formed in the HPT material after 5 min show an increased Al and Ni concentration. However, the Al concentration of the clusters in the HPT material is smaller than in the clusters of the reference material in this condition. After 60 min of aging the precipitates in the HPT material are closer to their expected Ni to Ti+Al ratio (75:25 for γ' -Ni₃(Al,Ti) and 50:50 for β -NiAl) than in the reference material. The spherical particles in the reference material are greatly enriched in Al and show a Ni to Ti+Al ratio that is lower than the expected ratio of the η -Ni₃Ti phase (75:25) and of the β -NiAl phase (50:50). In this stage, the spherical phase acts as a precursor for the formation of β -NiAl and η -Ni₃Ti. This can be compared to an effect discovered in a study by Leitner et al. [28]. They found that β -NiAl can act as a precursor phase for the formation of the η -Ni₃Ti phase. Furthermore, Zhang et al. [29] found that the η -Ni₃Ti phase forms spherical particles with a coherent precipitate-matrix interface in the early stage of precipitate evolution before the characteristic rod-like morphology is observed. The conclusion is that SPD is responsible for the formation of two distinct phases in the early

S. Zeisl et al.

Materials Science & Engineering A 833 (2022) 142416

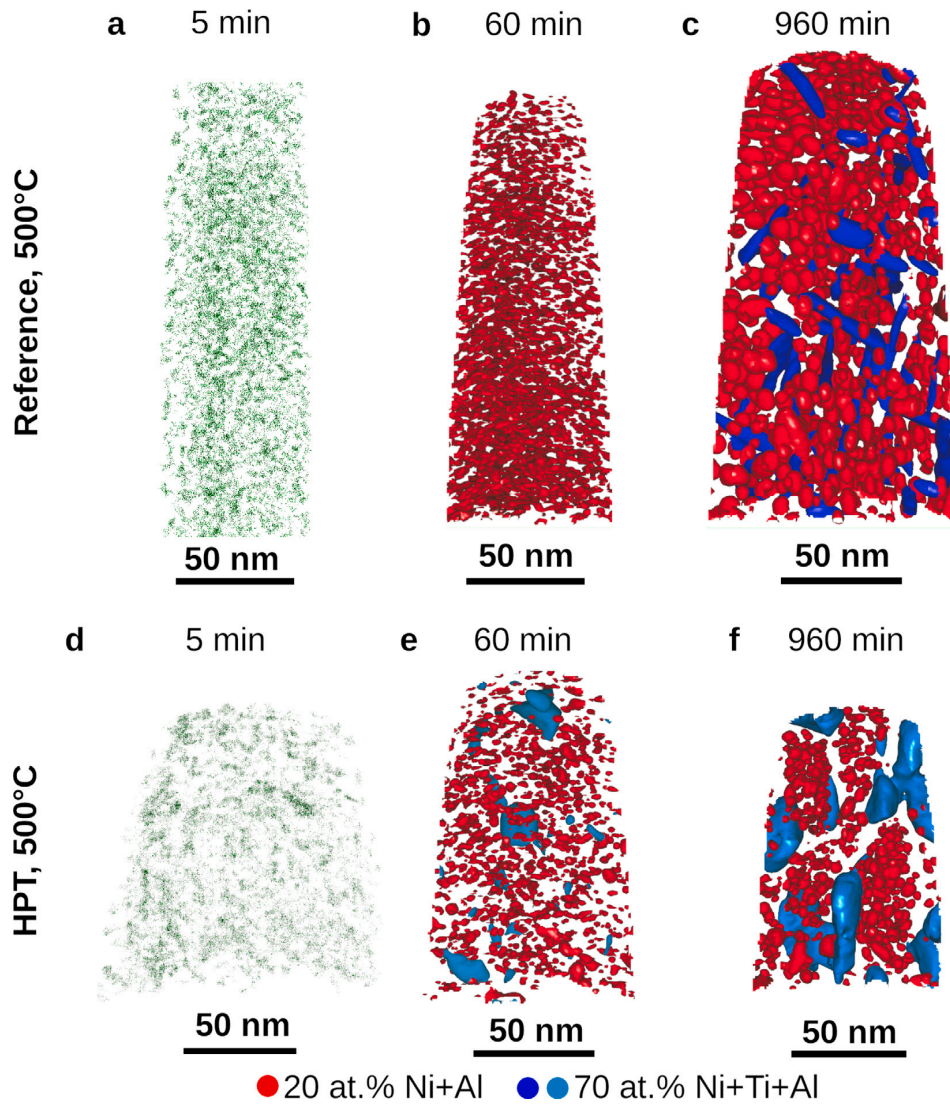


Fig. 8. Evolution of the clusters and precipitates for different aging times of the reference and the HPT material. The 5 min aged conditions are visualized by the distribution of Ni atoms, the remaining conditions are visualized using iso-concentration surfaces corresponding to the values in the legend.

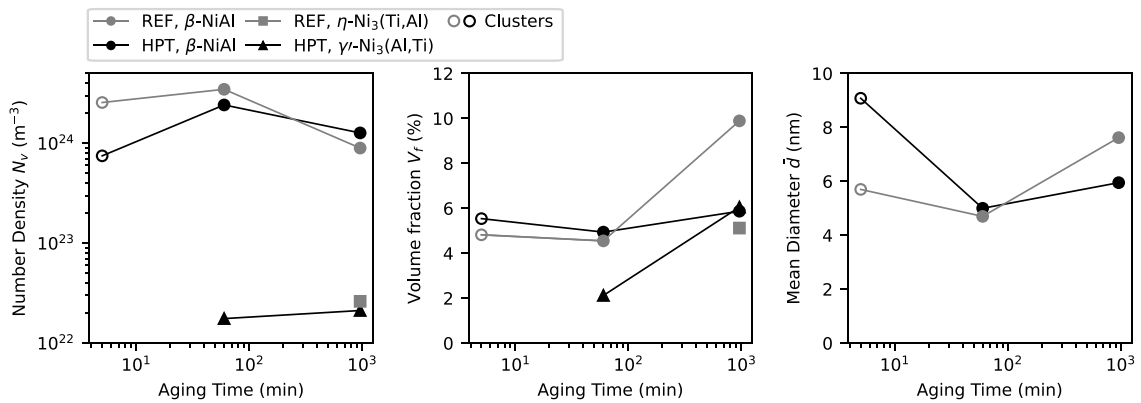


Fig. 9. Number density, volume fraction and mean diameter of the clusters and the β -NiAl, η -Ni₃(Ti,Al) and the γ' -Ni₃(Al,Ti) phase after aging at 500 °C.

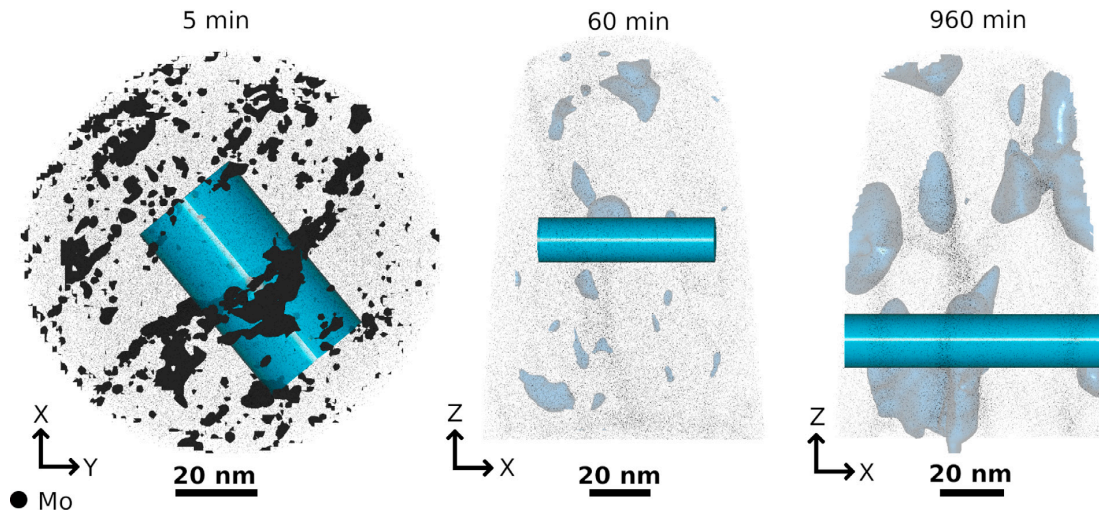


Fig. 10. Distribution Mo atoms and regions of interest corresponding to the 1-dimensional concentration profile of the aged HPT material. In the 60 min and 960 min aged condition the grain boundaries are visualized by the distribution of Mo atoms, for the 5 min condition 2.3 at.% Mo iso-concentration surfaces are used to show the grain boundaries. The location of the γ' -Ni₃(Al,Ti) precipitates with respect to the grain boundaries is visualized with 70 at.% Ni+Ti+Al iso-concentration surfaces.

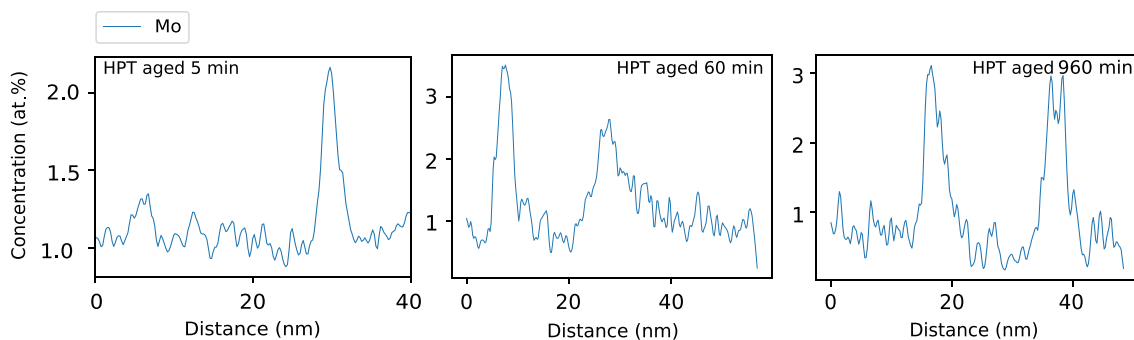


Fig. 11. 1-dimensional concentration profile showing the local concentration of Mo at the martensite lath boundaries. For the definition of the regions of interest refer to Fig. 10.

stages of aging (60 min) due to the heterogeneous nucleation of a γ' -phase at the grain boundaries. In the reference material, two distinct phases were observed after 960 min of aging. The β -NiAl particles in the HPT material aged for 960 min show a smaller increase of the average diameter than in the reference material. The comparison of the element concentrations in the conditions aged for 960 min show a higher concentration of Ni and Al in the γ' phase of the HPT material than for the η phase in the reference material. The growth of the γ' phase and the competition for Ni and Al with the β -NiAl phase leads to a slower growth behavior and to a constant volume fraction of β -NiAl in the HPT material and to the formation of precipitate free regions. APT reconstructions showed that the γ' -Ni₃(Al,Ti) phase was found exclusively at the grain boundaries in the HPT material. The rod-like η -Ni₃(Ti,Al) is typically formed at dislocations [26,29], explaining why this phase has a higher number density and is more evenly distributed than the γ' phase. The γ' -Ni₃(Al,Ti) phase was also observed in Cu and Si alloyed maraging steels [9,10].

After 5 min of aging the hardness increase is larger in the HPT material than in the reference material. The difference of the hardness increase between the two samples after the 5 min aging heat treatment stems from the different size of the clusters, their stage of development. Furthermore, the presence of austenite in the reference material contributes to a smaller hardness increase. After 60 min of aging the hardness increase is slightly smaller in the reference material than in the HPT material. This is in agreement with the observed precipitate

evolution. In this aging condition the number density, volume fraction and mean diameter of the β -NiAl phase is similar for the reference and HPT material. Additionally, the higher austenite fraction in the reference material contributes to a smaller overall hardness increase. After an aging time of 240 min the reference sample reaches its maximum hardness while the hardness of the HPT sample starts to decrease. In the reference material the hardening effect remains constant after 960 min of aging while the HPT material shows a further decrease. In the reference material the hardness increase between 60 min and 960 min is caused by the increased volume fraction of precipitates and by the decreased reverted austenite content. The hardness decrease in the HPT material stems from the precipitation of the γ' -Ni₃(Al,Ti) and from the formation of reverted austenite. The γ' -Ni₃(Al,Ti) phase forms at the grain boundaries and does not contribute to precipitation strengthening. As such, this phase is detrimental to the aging behavior because the potential for additional beneficial precipitates is not used and because precipitate free regions are created. Furthermore, for both materials a decreased contribution from solid solution strengthening can be expected since precipitating elements Ni, Ti and Al are continuously removed from the matrix as the precipitation reaction advances. The comparison of the evolution of the hardness increase can be used to show that the maximum hardening effect is the same for both samples. The aging time for peak hardness and for overaging is shifted to shorter times in the HPT material. The shift of aging times is in agreement with results from Tian et al. [30] who studied the influence of cold

rolling on a Co-alloyed maraging steel and with results from Castro Güiza et al. [14] who studied the influence of hot forging on a C300 maraging steel.

Segregation of Mo was observed in the HPT material already after 5 min of aging, after aging for 60 min and 960 min the concentration of Mo at the grain boundaries increased. This result is in agreement with the observations of Thuvander et al. [31] for a similar maraging steel. In a later study [9] Thuvander et al. found that the addition of Mo to a maraging steel can slow the coarsening of the Ni₃Ti phase for long aging times. This effect comes from the redistribution of Mo from the precipitate to the precipitate/matrix interface and thus a slower diffusion between matrix and precipitate. In the HPT material the segregation of Mo to the grain boundaries during aging was not sufficiently effective to slow the growth of the γ' phase.

Retained austenite was removed by HPT processing, this corresponds to a deformation induced transformation from austenite to martensite that is typically observed during cold deformation for steels with unstable austenite [5,32]. For both types of material (reference and HPT) an increase in the austenite content of the samples could be observed after aging. In the reference material the austenite content was increasing after already 5 min of aging, followed by a second increase after 60 min of aging. The austenite fraction decreased to a value of 15% after an aging time of 960 min. This overshooting of reverted austenite for 5 min and 60 min aging time is caused by the high amount of Ni solved in the matrix for these conditions. During the precipitation reaction between 60 min and 960 min reaction the Ni concentration in the matrix decreased as did the austenite fraction. In the HPT material the Ni concentration in the matrix was higher after 5 min of aging than in the reference material, but the Ni concentration decreased significantly between 5 min and 60 min aging time. The first austenite in the HPT material was found after 960 min. Quantitative analysis showed that HPT and the resulting grain refinement stabilized the globular α' matrix phase and led to a decreased reversion to austenite. At typical aging temperatures austenite nucleates at the prior austenite grain boundaries or at the martensite lath boundaries [33], but in the HPT material these features of the martensitic microstructure are lost. Furthermore, the grain boundaries are decorated with Mo, a stabilizer of the α -Fe phase, explaining the decreased reversion to austenite.

5. Conclusion

A Co-free Ti- and Al-alloyed maraging steel was deformed using an SPD method. Aging heat treatment experiments with varying aging times were performed and the material was characterized according to the hardness and the microstructure on a micro-to-nano scale. Following conclusions can be drawn:

1. SPD provides a significant hardness increase for solution-annealed maraging steels by a combination of grain refinement and cold deformation.
2. For the maraging steel used in this study the impact of SPD on the maximum hardening effect from aging is negligible and the effects caused by shorter over-aging times and additional grain boundary phases are detrimental to the aging behavior. As such, SPD is not a feasible process for this type of maraging steels if the influence on aging is the primary concern.
3. The change of the microstructure and grain refinement caused by SPD has an influence on the segregation behavior of Mo. Mo segregates to the grain boundaries during the aging heat treatment following SPD. The localized higher concentration of Mo suppresses the reversion of martensite to austenite.
4. The low fraction of reverted austenite and the segregation of Mo after SPD and aging can be expected to impact the toughness of this maraging alloy negatively. Furthermore, the observed trend of austenite reversion for short aging times in the reference material is unexpected, the mechanisms behind this observation were not within the scope of this study. Both points should be addressed in further research.

CRedit authorship contribution statement

S. Zeisl: Conceptualization, Methodology, Formal analysis, Writing – original draft. A. Lassnig: Investigation (TEM analysis), Writing – review & editing. A. Hohenwarter: Investigation (TKD analysis), Writing – review & editing. F. Mendez-Martin: Writing – review & editing, Supervision.

Declaration of competing interest

The authors declare the following financial interests/personal relationships which may be considered as potential competing interests:

1. The European Research Fund for Coal and Steel (RFCS 847165): funding for S. Zeisl and for the material.
2. The Austrian Science Fund (FWF) Hertha Firnberg Program (T891-N36): funding for A. Lassnig.

Data availability

Access to the experimental data will be given out by the authors upon request

Acknowledgments

The authors want to thank the European Research Fund for Coal and Steel (RFCS 847165) for providing the funding that made this study possible and the Austrian Science Fund (FWF) for providing the funding for A.L. within the Hertha Firnberg Program (T891-N36). Further thanks goes to the “iNiTiAl” consortium for providing the material.

References

- [1] K. Li, B. Yu, R.D. Misra, G. Han, S. Liu, C.J. Shang, Strengthening of cobalt-free 19Ni3Mo1.5Ti maraging steel through high-density and low lattice misfit nanoscale precipitates, *Mater. Sci. Eng. A* 715 (January) (2018) 174–185.
- [2] T.H. Simm, L. Sun, D.R. Galvin, E.P. Gilbert, D. Alba Venero, Y. Li, T.L. Martin, P.A. Bagot, M.P. Moody, P. Hill, H.K. Bhadeshia, S. Biroscas, M.J. Rawson, K.M. Perkins, A SANS and APT study of precipitate evolution and strengthening in a maraging steel, *Mater. Sci. Eng. A* 702 (July) (2017) 414–424.
- [3] R. Schnitzer, G.A. Zickler, E. Lach, H. Clemens, S. Zinner, T. Lippmann, H. Leitner, Influence of reverted austenite on static and dynamic mechanical properties of a PH 13-8 Mo maraging steel, *Mater. Sci. Eng. A* 527 (7–8) (2010) 2065–2070.
- [4] M. Schober, R. Schnitzer, H. Leitner, Precipitation evolution in a Ti-free and Ti-containing stainless maraging steel, *Ultramicroscopy* 109 (5) (2009) 553–562.
- [5] D. Raabe, D. Ponge, O. Dmitrieva, B. Sander, Nanoprecipitate-hardened 1.5 GPa steels with unexpected high ductility, *Scr. Mater.* 60 (12) (2009) 1141–1144.
- [6] A.J. Ardell, Precipitation hardening, *Metall. Trans. A* 16 (12) (1985) 2131–2165.
- [7] M.R. Ahmadi, E. Povoden-Karadeniz, K.I. Öksüz, A. Falahati, E. Kozeschnik, A model for precipitation strengthening in multi-particle systems, *Comput. Mater. Sci.* 91 (2014) 173–186.
- [8] H. Leitner, R. Schnitzer, M. Schober, S. Zinner, Precipitate modification in PH13-8 Mo type maraging steel, *Acta Mater.* 59 (12) (2011) 5012–5022.
- [9] M. Thuvander, M. Andersson, K. Stiller, Multiple influences of molybdenum on the precipitation process in a martensitic PH stainless steel, *Metals* 9 (10) (2019) 1118.
- [10] M. Thuvander, M. Andersson, K. Stiller, Precipitation process of martensitic PH stainless steel Nanoflex, *Mater. Sci. Technol.* 28 (6) (2012) 695–701.
- [11] H. Calderon, M.E. Fine, Coarsening kinetics of coherent NiAl-type precipitates in FeNiAl and FeNiAlMo alloys, *Mater. Sci. Eng.* 63 (2) (1984) 197–208.
- [12] C.K. Yao, Z. Xu, Influence of hot-deformation on morphology and effective grain size of lath martensite in 18Ni maraging steel, *Mater. Chem. Phys.* 14 (6) (1986) 559–568.
- [13] E.I. Galindo-Nava, W.M. Rainforth, P.E. Rivera-Díaz-del Castillo, Predicting microstructure and strength of maraging steels: Elemental optimisation, *Acta Mater.* 117 (2016) 270–285.
- [14] G.M. Castro Güiza, C.A. Oliveira, Microstructural changes produced by hot forging in a C300 maraging steel, *Mater. Sci. Eng. A* 655 (2016) 142–151.
- [15] Y. Lian, J. Huang, J. Zhang, C. Zhao, W. Gao, Z. Zhang, M. Ma, Effects of cold rolling on the microstructure and properties of Fe-Cr-Ni-Mo-Ti maraging steel, *Mater. Sci. Eng. A* 712 (July 2017) (2018) 663–670.

S. Zeisl et al.

Materials Science & Engineering A 833 (2022) 142416

- [16] Y.R. Kolobov, B. Kieback, K.V. Ivanov, T. Weissgaerber, N.V. Girsova, Y.I. Pochivalov, G.P. Grabovetskaya, M.B. Ivanov, V.U. Kazyhanov, I.V. Alexandrov, The structure and microhardness evolution in submicrocrystalline molybdenum processed by severe plastic deformation followed by annealing, *Int. J. Refract. Metals Hard Mater.* 21 (1–2) (2003) 69–73.
- [17] V. Maier, A. Hohenwarther, R. Pippan, D. Kiener, Thermally activated deformation processes in body-centered cubic Cr - how microstructure influences strain-rate sensitivity, *Scr. Mater.* 106 (2015) 42–45.
- [18] T. Leitner, I. Sabirov, R. Pippan, A. Hohenwarther, The effect of severe grain refinement on the damage tolerance of a superelastic NiTi shape memory alloy, *J. Mech. Behav. Biomed. Mater.* 71 (November 2016) (2017) 337–348.
- [19] B. Schuh, F. Mendez-Martin, B. Völker, E.P. George, H. Clemens, R. Pippan, A. Hohenwarther, Mechanical properties, microstructure and thermal stability of a nanocrystalline CoCrFeMnNi high-entropy alloy after severe plastic deformation, *Acta Mater.* 96 (2015) 258–268.
- [20] X. Sauvage, G. Wilde, S.V. Divinski, Z. Horita, R.Z. Valiev, Grain boundaries in ultrafine grained materials processed by severe plastic deformation and related phenomena, *Mater. Sci. Eng. A* 540 (2012) 1–12.
- [21] Y. Cao, S. Ni, X. Liao, M. Song, Y. Zhu, Structural evolutions of metallic materials processed by severe plastic deformation, *Mater. Sci. Eng. R* 133 (June) (2018) 1–59.
- [22] A.P. Zhilyaev, T.G. Langdon, Using high-pressure torsion for metal processing: Fundamentals and applications, *Prog. Mater. Sci.* 53 (6) (2008) 893–979.
- [23] L. Lutterotti, M. Bortolotti, G. Ischia, I. Lonardelli, H.R. Wenk, Rietveld texture analysis from diffraction images, *Z Kristallogr.* 1 (26) (2007) 125–130.
- [24] B. Gault, M. Moody, J.M. Cairney, S.P. Ringer, *Atom Probe Microscopy*, Springer, New York, NY, 2012.
- [25] E.A. Jäggle, P.P. Choi, D. Raabe, The maximum separation cluster analysis algorithm for atom-probe tomography: Parameter determination and accuracy, *Microsc. Microanal.* 20 (6) (2014) 1662–1671.
- [26] U.K. Viswanathan, G.K. Dey, M.K. Asundi, Precipitation hardening in 350 grade maraging steel, *Metall. Trans. A* 24 (11) (1993) 2429–2442.
- [27] K. Jacob, D. Yadav, S. Dixit, A. Hohenwarther, B.N. Jaya, High pressure torsion processing of maraging steel 250: Microstructure and mechanical behaviour evolution, *Mater. Sci. Eng. A* 802 (June 2020) (2021) 140665.
- [28] H. Leitner, M. Schober, R. Schnitzer, Splitting phenomenon in the precipitation evolution in an Fe-Ni-Al-Ti-Cr stainless steel, *Acta Mater.* 58 (4) (2010) 1261–1269.
- [29] C. Zhang, C. Wang, S.L. Zhang, Y.L. Ding, Q.L. Ge, J. Su, Effect of aging temperature on the precipitation behavior and mechanical properties of Fe-Cr-Ni maraging stainless steel, *Mater. Sci. Eng. A* 806 (January) (2021) 140763.
- [30] J. Tian, W. Wang, H. Li, M.B. Shahzad, Y. Shan, Z. Jiang, K. Yang, Effect of deformation on precipitation hardening behavior of a maraging steel in the aging process, *Mater. Charact.* 155 (April) (2019) 109827.
- [31] M. Thuvander, M. Andersson, K. Stiller, Atom probe tomography investigation of lath boundary segregation and precipitation in a maraging stainless steel, *Ultramicroscopy* 132 (2013) 265–270.
- [32] M.K. El-Fawkhry, M. Eissa, A. Fathy, T. Mattar, Development of maraging steel with retained austenite in martensite matrix, *Mater. Today Proc.* 2 (2015) 711–714.
- [33] K. Li, L. Wei, B. Yu, R.D. Misra, Reverted austenite with distinct characteristics in a new cobalt-free low lattice misfit precipitate-bearing 19Ni3Mo1.5Ti maraging steel, *Mater. Lett.* 257 (2019) 2–7.

Publication II

Cooling rate controlled aging of a Co-free Fe-Ni-Cr-Mo-Ti-Al maraging steel

S. Zeisl, R. Schnitzer

Metals **12(4)**, 538 (2022)

Article

Cooling Rate Controlled Aging of a Co-Free Fe-Ni-Cr-Mo-Ti-Al Maraging Steel

Stefan Zeisl ^{*}  and Ronald Schnitzer 

Department of Materials Science, Montanuniversität Leoben, Franz-Josef Straße 18, 8700 Leoben, Austria; ronald.schnitzer@unileoben.ac.at

* Correspondence: stefan.zeisl@unileoben.ac.at

Abstract: Maraging steels are high-strength steels that are hardened by the formation of precipitates during an isothermal aging heat treatment. Depending on the aging temperature and time the cooling rate after holding can play a significant factor on the development of the microstructure and mechanical properties. This study seeks to show how the cooling time influences the precipitation hardening effect, austenite reversion and the development of hardness and impact toughness. The material was aged at a constant temperature using holding times of 0 h, 4 h and 15 h and cooled with different cooling rates resulting in cooling times of 7 h, 28 h and 56 h. The microstructure was characterized using a combination of electron backscatter diffraction, X-ray diffraction and atom probe tomography with cluster-based precipitate analysis. It is shown that the effect of the cooling time is strongly dependent on the holding time and that a longer cooling time can improve hardness and impact toughness.

Keywords: maraging steels; atom probe tomography; heat treatment study; X-ray diffraction; intermetallic precipitates



Citation: Zeisl, S.; Schnitzer, R.

Cooling Rate Controlled Aging of a Co-Free Fe-Ni-Cr-Mo-Ti-Al Maraging Steel. *Metals* **2022**, *12*, 538. <https://doi.org/10.3390/met12040538>

Academic Editor: Angelo Fernando Padilha

Received: 2 March 2022

Accepted: 18 March 2022

Published: 22 March 2022

Publisher's Note: MDPI stays neutral with regard to jurisdictional claims in published maps and institutional affiliations.



Copyright: © 2022 by the authors. Licensee MDPI, Basel, Switzerland. This article is an open access article distributed under the terms and conditions of the Creative Commons Attribution (CC BY) license (<https://creativecommons.org/licenses/by/4.0/>).

1. Introduction

Maraging steels are a class of high-strength steels that provide a good combination of strength and ductility [1]. Therefore they are often used for applications where well-balanced mechanical properties are required. The microstructure of maraging steels consists of a soft lath martensite matrix with high dislocation density, precipitates and sometimes austenite [2]. The mechanical properties of maraging steels are governed by the precipitation of small intermetallic phases and the reversion of martensite to austenite. Both happen during isothermal aging heat treatments at aging temperatures around 400 to 600 °C typically for several hours. The strengthening effect of precipitates was discovered in the early 1900s by A. Wilm [3] and has become a widely used mechanism in modern materials. The precipitates act as obstacles for the movement of dislocations. These obstacles need to be overcome using either the shearing or the bowing (Orowan) mechanism. This increases the shear strength necessary to move the dislocations, leading to a strength increase [4]. Precipitation strengthening depends on many physical properties of the precipitate phase: the coherency with the matrix, the size and distribution, the elastic properties and anti-phase boundary energy [4], to name a few. A model for the strengthening effect, with focus on multi-precipitate systems, was extensively described by Ahmadi et al. [5]. For Co-free, Ti- and Al-alloyed maraging steels the main strength contributing precipitates are the β -NiAl (B2 structure) [6] and the η -Ni₃Ti (D0₂₄ structure) phases [7,8]. The β -NiAl precipitates can be identified by their spherical morphology [9,10] and are coherent with the α' -Fe martensitic matrix [11]. β -NiAl is a major strength contributor over a wide range of aging temperatures and aging times due to its slow coarsening behaviour. This can be attributed to its small lattice misfit with the matrix [11]. The η -Ni₃Ti precipitates preferably nucleate at dislocations and are only coherent in their early stages. In later aging stages this η -Ni₃Ti phase grows along the dislocation core to form rod-like semi-coherent particles [12].

The reversion of martensite to austenite is strongly dependent and enhanced by the aging temperature, as shown by studies from Nakagawa et al. [13] and Conde et al. [14]. Furthermore, the aging temperature and time have an impact on the location and morphology of the reverted austenite. At the lower end of aging temperatures austenite begins to form as a film-like phase along the lath boundaries, as demonstrated by Zhang et al. [15]. At the higher end of aging temperatures (around 600 °C) block-like austenite can be observed within the martensite matrix [15]. During deformation the reverted austenite is transformed to martensite, this manifests itself as an improvement in ductility and impact toughness (TRIP effect) [16]. For instance: Wang et al. [17] used a strategy based on cold-rolling to achieve a broad grain size distribution of reverted austenite. Using this strategy they could increase the ultimate tensile strength as well as the fracture elongation of a martensitic steel.

Currently, maraging steels are usually aged with isothermal holding followed by air cooling. This can lead to different cooling rates for large and small work pieces or for regions with different thickness within a work piece. The effects of the aging temperature and time are already well studied for many types of maraging steels, but the effect of the cooling rate after holding at the aging temperature is not. The goal of this study is to show how the hardness and the impact toughness of a Co-free Fe-Ni-Cr-Mo-Ti-Al maraging steel are influenced by the cooling rate after the aging heat treatment, with special focus on slow cooling rates. It should also be established how the aging time affects the relationship between the cooling rate and the hardness and impact toughness and how this relationship depends on the microstructural characteristics.

2. Materials and Methods

The material was produced by vacuum induction melting followed by vacuum arc melting for multiple times to ensure a homogeneous ingot. The ingot was then open-die forged to a bar with a diameter of 140 mm. The chemical composition of the maraging steel is displayed in Table 1. After forging the bar was solution annealed at 850 °C for 90 min and quenched in water, followed by a cryogenic treatment at −80 °C for 16 h. The starting point for all aging heat treatment was the solution annealed and quenched condition (SA + Q). Samples with a 12 × 12 mm² square profile and a length of 100 mm were cut from the half-radius position of the bar and furnished with a 10 mm deep blind hole with a diameter of 3 mm in the center of the cross section for temperature measurements during aging. The samples were aged at 510 °C with 15 h, 4 h and 0 h aging time. For each aging time 3 samples with constant cooling rates that resulted in cooling times of 56 h, 28 h and 7 h (measured from 510 °C to 100 °C) were produced. The temperature-time profiles of all aging heat treatments are shown in Figure 1. The aging heat treatments were performed in a Nabertherm N11/HR box oven. The core temperature of the samples was measured using a type K thermocouple and tracked using a Eurotherm 6100A data logger. For better readability the aged conditions will be abbreviated using a holding time-cooling time naming system (e.g., 0-56 for 0 h aging time and 56 h cooling time).

The samples for electron backscatter diffraction (EBSD) and X-ray diffraction (XRD) were prepared using standard polishing methods, EBSD samples were finished by electropolishing using a Struers A2 electrolyte. The Vickers hardness was measured using an M4C 025 G3M machine (EMCO-Test, Kuchl, Austria) and a load of 10 kg. The mean hardness and the standard error of mean was calculated using at least five measurements from each condition. The room temperature (21 °C) impact toughness was measured with a Charpy V-notch impact test according to EN ISO148-1 with specimens measuring 55 × 10 × 10 mm³ and a notch radius of 0.25 mm. One specimen was tested for each condition. The martensite block size was measured with EBSD using a Versa3D DualBeam workstation (FEI, Hillsboro, OR, USA) and an orientation mismatch of 10.5° was used to define the martensite blocks. The austenite fraction was determined by XRD using a Bruker Advanced D8 DaVinci instrument with Cu-K α radiation and evaluated using LaB₆-calibrated Rietveld refinement.

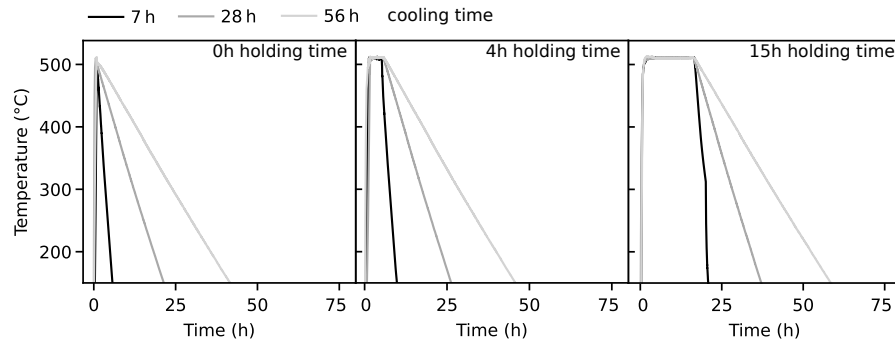


Figure 1. Temperature-time profiles of the aging heat treatments with 0 h, 4 h and 15 h aging time and with 7 h, 28 h and 56 h cooling time.

Table 1. Chemical composition of the maraging steel investigated in this study.

	Fe	Ni	Cr	Mo	Ti	Al	C
wt. %	bal.	12.3	10.2	2.0	1.2	1.5	<0.03
at. %	bal.	11.6	10.8	1.2	1.4	3.1	<0.14

Atom probe tomography (APT) was used to characterize the distribution and chemistry of precipitates. The measurements were performed with a LEAP 3000X HR microscope (Cameca, Gennevilliers Cedex, France) using the laser assisted mode with a pulse frequency of 250 kHz, a laser energy of 0.3 nJ and a detection rate of 1% at a temperature of 60 K. The APT specimens were prepared with a standard 2-step electropolishing method [18]. The first polishing step was performed with a solution of 25 vol% of perchloric acid in glacial acetic acid and the final step was performed with a 2% solution of perchloric acid in 2-butoxyethanol. The IVAS software suite (Cameca, version 3.6.1) was used to analyze the atom probe data. For the statistical evaluation of the precipitates a cluster search based on the maximum separation method was used, upon which the volume fraction F_v of precipitates was calculated according to [19]:

$$F_v = \frac{N \cdot v \cdot C}{V_{total}} \tag{1}$$

N corresponds to the total number of ions found in the clusters corresponding to the precipitates, v to the volume per atom according to the unit cell of the precipitate phase, V_{total} to the total volume of the measurement and C to a correction factor accounting for the detector efficiency. The parameters d_{Max} and N_{Min} used for the maximum separation method are presented in Table 2. d_{Max} is the maximum pair distance between adjacent atoms and N_{Min} minimal cluster size. An order of 4 was used for the maximum separation method. The erosion and envelope distance were chosen to be equal to d_{Max} . The value of d_{Max} was determined using a procedure described by Jäggle et al. [20].

The experimental data was used to calculate the contributions of solid solution hardening, grain size hardening, the dislocation density and precipitation hardening to the total hardness. The contribution of the martensite matrix ($\sigma_{\alpha'}$) was determined by using a Hall-Petch model to account for grain size hardening, furthermore the contribution of the dislocation density was also considered within this term. The solid solution strengthening (σ_{SS}) was determined by using the Fleischer model. Both models were implemented as described by Galindo-Nava et al. [21].

$$\sigma_{\alpha'} = \frac{300}{\sqrt{d_{Block}}} + 0.25M\mu b\sqrt{\rho} \tag{2}$$

$$\sigma_{SS} = \sum_i (\beta_i^2 x_i)^{1/2} \tag{3}$$

300 MPa $\mu\text{m}^{-1/2}$ is the Hall-Petch constant that was determined for maraging steels [21], d_{Block} is the average martensite block size, μ is the shear modulus of Fe (80.4 GPa [22]), b is the magnitude of the Burgers vector (0.268 nm [21]), ρ is the dislocation density and β_i and x_i are the solid solution factor and the molar fraction of each alloying element. The strength contribution stemming from the dislocation density (σ_ρ) was calculated as the difference between the total strength and the sum of the contributions from solid solution strengthening and grain size strengthening. With the value for σ_ρ the dislocation density was estimated with $\rho = \sigma_\rho^2 / (0.25M\mu b)^2$ from Equation (2). The solid solution factor β_i was determined using Equation (4) according to Fleischer’s formula [21].

$$\beta_i = \kappa\mu(\eta'_i + 16\delta_i)^{3/2} \tag{4}$$

The fitting parameter κ was determined as $\kappa = 0.0045$ [21], $\eta'_i = \eta_i / (1 + 0.5\eta_i)$ is calculated from the modulus distortion with respect to pure iron $\eta_i = |\mu_i - \mu_{Fe}| / \mu_{Fe}$ and $\delta_i = |r_i - r_{Fe}| / r_{Fe}$ corresponds to the lattice distortion with respect to pure iron. The shear modulus μ_i and the metallic radius r_i were obtained from [22]. The strength loss due to the formation of reverted austenite was considered using a linear mixture rule as presented by Schnitzer et al. [23] with the strength of 100% pure austenite being $\sigma_\gamma = 217$ MPa. With the volume fractions $F_{\alpha'}$ and F_γ of martensite and austenite respectively, the strength contribution from the matrix can be expressed as: $\sigma_{\text{Matrix}} = F_{\alpha'}\sigma_{\alpha'} + F_\gamma\sigma_\gamma$. With this, the yield strength σ_Y of the aged samples can be expressed as:

$$\sigma_Y = \sigma_0 + \sigma_{\text{Matrix}} + \sigma_{SS} + \sigma_P \tag{5}$$

$\sigma_0 = 50$ MPa corresponds to the strength due to lattice friction [21] and σ_P to the strength contribution due to precipitation hardening. The conversion from the yield strength in MPa to the Vickers hardness value H_V can be performed using a factor 1/3 according to $H_V = \sigma_Y / 3$ [24].

Table 2. The central element, maximum pair distance (d_{Max}) and minimal cluster size (N_{Min}) used for the maximum separation method for cluster detection for each condition.

Condition	β -NiAl			η -Ni ₃ Ti		
	Central Element	d_{Max} (nm)	N_{Min}	Central Element	d_{Max} (nm)	N_{Min}
0-7	Ti	0.95	75			
0-28	Al	0.75	130	Ti	0.95	400
0-56	Al	0.80	150	Ti	0.96	450
4-7	Al	0.78	150	Ti	0.93	800
4-28	Al	0.80	150	Ti	0.98	800
4-56	Al	0.75	130	Ti	0.98	800
15-7	Al	0.70	80	Ti	0.94	700
15-28	Al	0.71	80	Ti	0.94	800
15-56	Al	0.70	140	Ti	0.94	800

3. Results

Figure 2 shows the austenite fractions of all aged conditions. All samples had similar austenite fractions within a range between 7.5% and 12.5%. In the SA + Q condition the austenite fraction was measured and evaluated to be 4.4%. The trend shows an increasing austenite fraction with longer cooling times for the samples with 0 h aging time. For the 4 h and 15 h holding time samples the austenite fraction remained constant within the experimental uncertainty. EBSD revealed that the mean martensite block size was 7.6 μm in the SA + Q condition and between 5.6 μm and 7.6 μm in the aged conditions. No difference

of the matrix microstructure was found between the aged conditions, as shown in Figure 3 for the 0 h aging time samples.

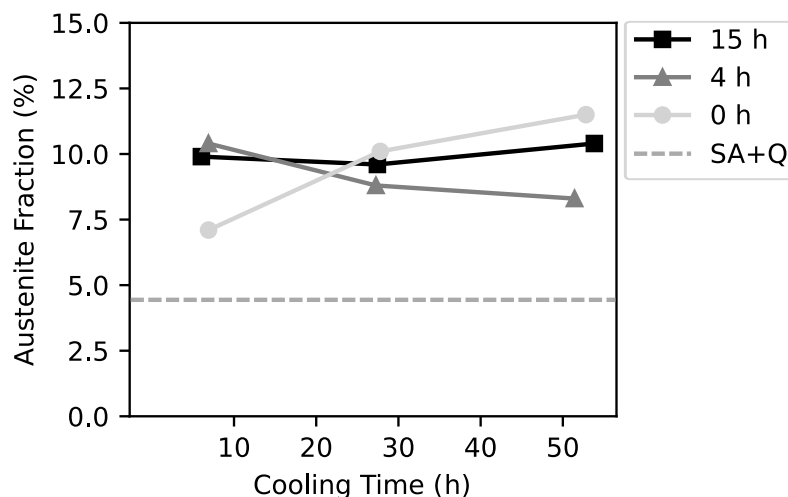


Figure 2. Austenite fraction of the aged conditions with 0 h, 4 h and 15 h aging time as function of the cooling time.

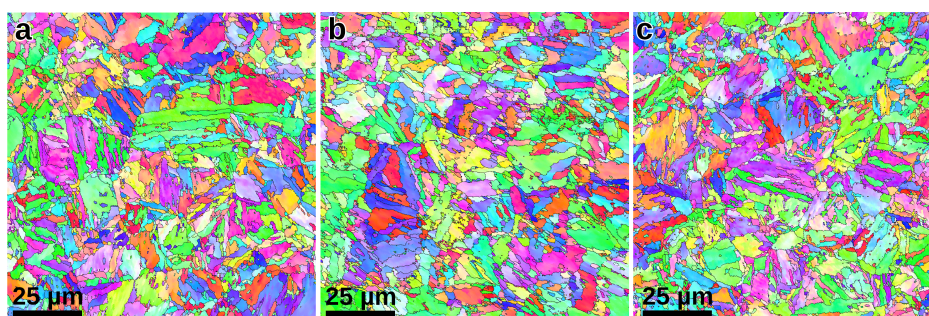


Figure 3. Inverse pole figures obtained from EBSD measurements of the sample group with 0 h aging time and (a) 7 h, (b) 28 h and (c) 56 h cooling time. The martensite block boundaries are represented by lines corresponding to a 10.5° orientation mismatch.

The results from the APT measurements are shown in Figure 4, where the precipitates are represented by iso-concentration surfaces. Two different types of precipitated phases were identified. A spherical phase with approximately equal concentration of Ni and Al, corresponding to a β -NiAl phase, and a rod-like precipitate phase with a Ni to Ti + Al ratio of about 65% Ni and 35% Ti + Al, corresponding to a η -Ni₃(Ti,Al) phase. The size of the η -Ni₃(Ti,Al) phase increased with longer aging time at each cooling time. In the samples with 0 h aging time the η -Ni₃(Ti,Al) phase was only observed in the conditions with 28 h and 56 h cooling time. The η -Ni₃(Ti,Al) phase was found in all conditions of the samples with 4 h and 15 h cooling time.

Figure 5a shows the ratio between Ni and Ti + Al for each heat treatment condition. The Ni to Ti + Al ratio fluctuates around 0.45 for the β -NiAl phase, but for the η -Ni₃(Ti,Al) phase the Ni concentration increases with the aging time. For the 0 h aging time sample the influence of a longer cooling time is displayed by a significantly increased Ni concentration in the η -Ni₃(Ti,Al) phase. The concentration of precipitating elements (Ni, Ti, Al) in the matrix is displayed in Figure 5b. The concentration of Ni, Ti and Al decreased with increasing aging time and partially with increased cooling time.

The volume fraction of each precipitate phase was calculated from the results of the cluster analysis and is shown in Figure 6. For the samples with 0 h and 4 h aging time the volume fraction of the β -NiAl and η -Ni₃(Ti,Al) phases increased between 28 h and 56 h cooling time. For the 15 h aging time sample the volume fraction of η -Ni₃(Ti,Al) decreased with longer cooling times, while the volume fraction of β -NiAl increased with a longer cooling time. The number density of both types of precipitates remained similar for all conditions, with exception of the 4-28 condition where a smaller number density of η -Ni₃(Ti,Al) was observed.

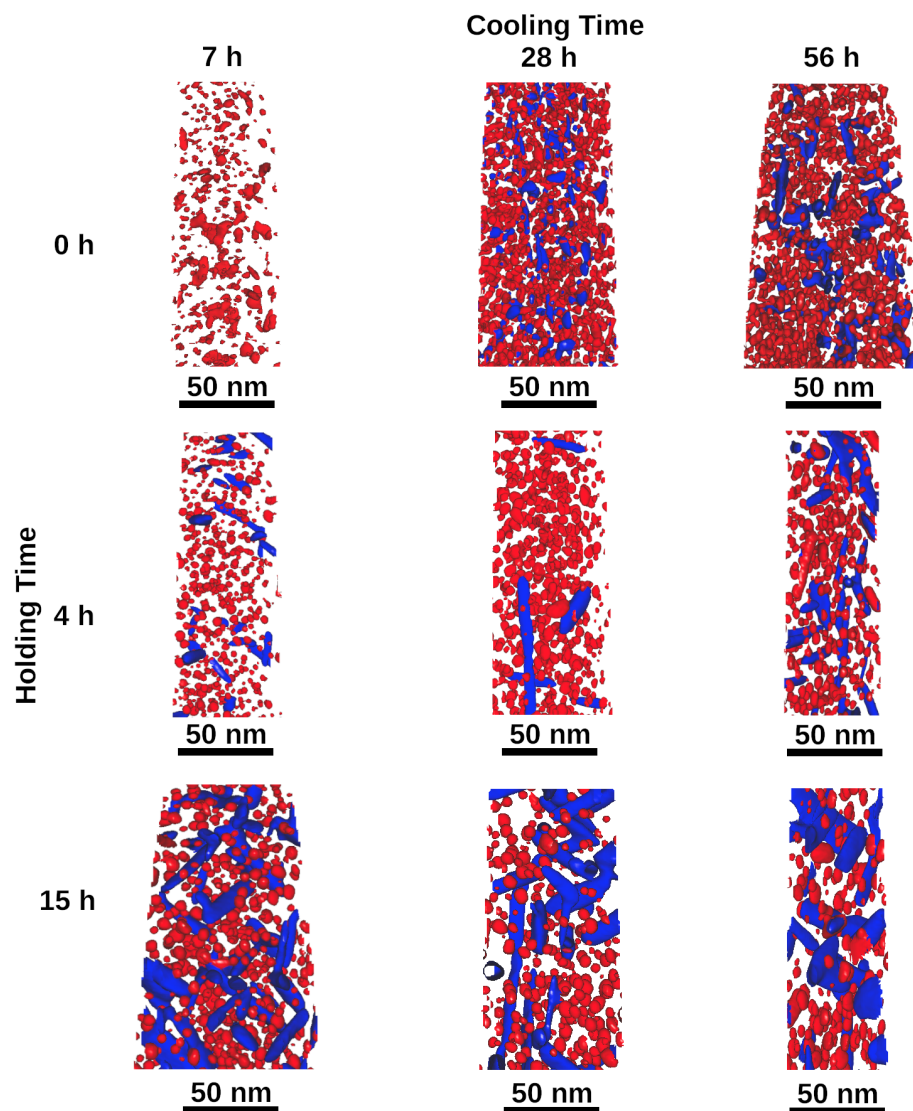


Figure 4. Iso-concentration surfaces showing the precipitate evolution with respect to the cooling time for the 15 h, 4 h and 0 h aged samples. The β -NiAl and η -Ni₃(Ti,Al) phases are represented by 30 at.% Ni + Al (red) and 65 at.% Ni + Ti + Al (blue) iso-concentration surfaces, respectively. For the 0 h aging time samples 25 at.% Ni + Al (red) and 40 at.% Ni + Ti + Al (blue) iso-concentration surfaces are used to represent the η -Ni₃(Ti,Al) and β -NiAl phases, respectively.

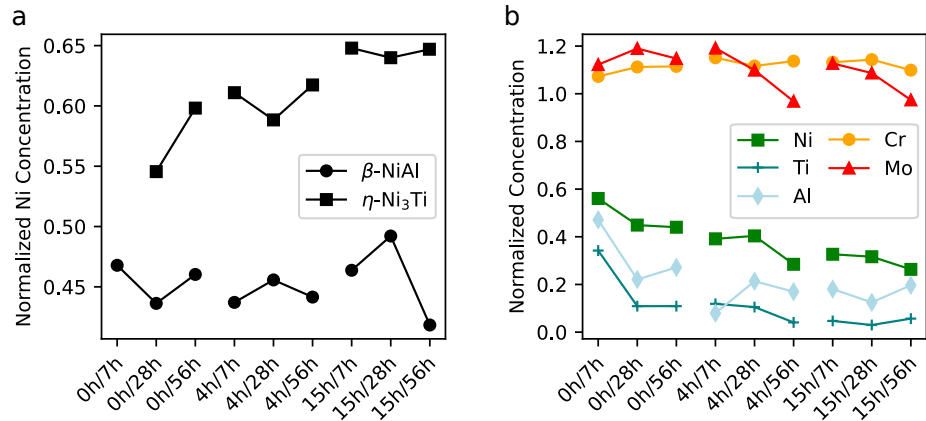


Figure 5. (a) Concentration of Ni in the precipitates, normalized to the total concentration of Ni, Ti and Al. (b) Concentration of the alloying elements in the matrix phase, normalized to the average bulk composition.

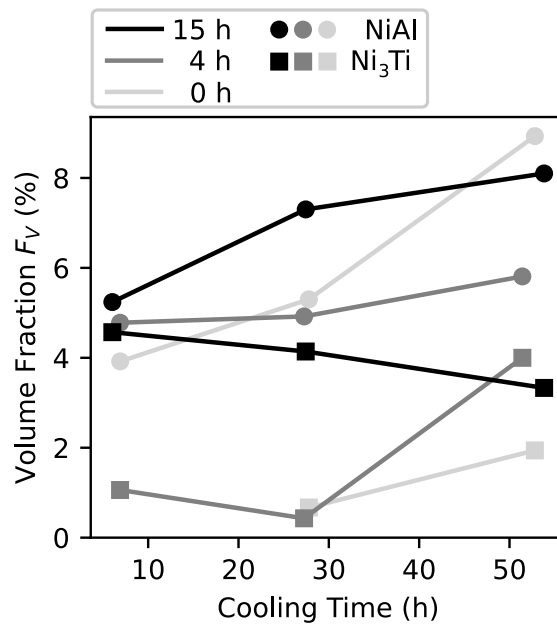


Figure 6. Volume fraction of the precipitates found in the aged conditions as function of the cooling time.

Figure 7a shows that the hardness of the materials increased with increasing cooling time for all 3 aging times. The hardness of the alloy in SA + Q condition was 324 HV10. The increase of hardness with longer cooling time was the strongest in the samples with 0 h aging time and the weakest in the samples with 15 h aging time.

The impact energy for each condition is shown in Figure 7b. No clear correlation was observed for the samples with 15 h and 4 h aging time, however both samples showed a drop in impact toughness for 28 h cooling time. The 0 h sample had a higher impact toughness after long cooling times than after short cooling times.

Figure 8 and Table 3 show the contribution of the matrix, solid solution hardening and precipitation hardening to the total hardness. The 0-7 condition showed the weakest precipitation hardening effect with a value of 296 HV, but the highest contribution from solid solution hardening with a value of 176 HV. Cooling the 0 h aged samples for 28 h or longer led to a significantly increased precipitation hardening effect compared to 7 h cooling

time. The 4 h and 15 h aged samples showed a similar hardening effect due to precipitation hardening after 7 h cooling time. For both aging times the contribution from precipitation hardening increased slightly with longer cooling times, possessing a maximum of 380 HV for the 4-56 condition. The hardness contribution from the matrix was within below 100 HV for all conditions.

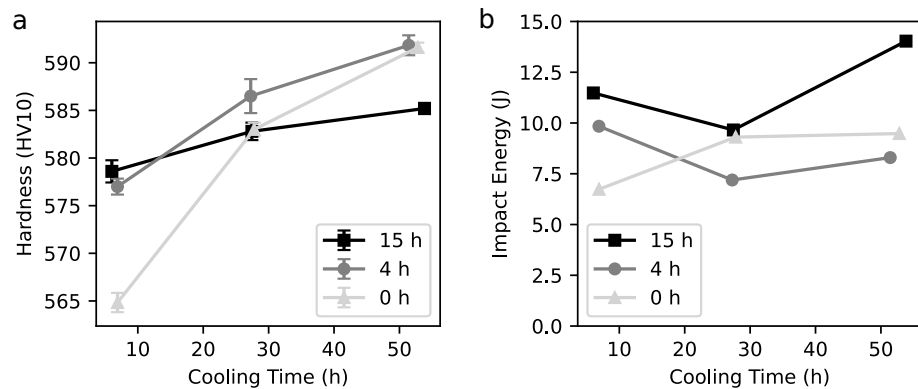


Figure 7. (a) Hardness and (b) impact toughness of the aged conditions with 0 h, 4 h and 15 h aging time as function of the cooling time.

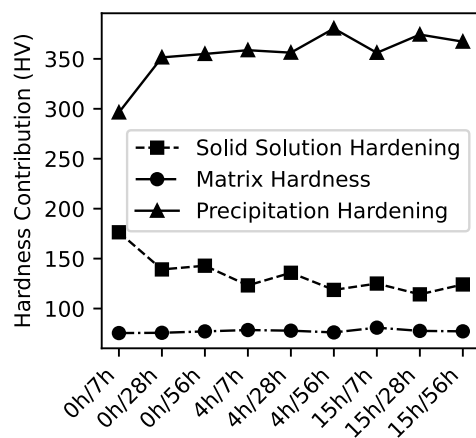


Figure 8. Contributions of different mechanisms to the total hardness for each aged condition.

Table 3. The contribution (in HV) of the matrix ($H_{V,Matrix}$), solid solution hardening ($H_{V,SS}$) and precipitation hardening ($H_{V,P}$) to the total hardness. $H_{V,0}$ corresponds to the hardness due to lattice friction.

Condition	H _V	H _{V,0}	H _{V,Matrix}	H _{V,SS}	H _{V,P}
0-7	565	17	75	176	296
0-28	583	17	76	139	351
0-56	592	17	77	143	355
4-7	577	17	78	123	359
4-28	587	17	78	136	356
4-56	592	17	76	119	380
15-7	579	17	81	125	356
15-28	583	17	78	114	374
15-56	585	17	77	124	367

4. Discussion

In this study a Co-free Fe-Ni-Cr-Mo-Ti-Al maraging steel was aged at 510 °C for 0 h, 4 h, and 15 h and cooled using three different cooling rates resulting in a cooling time of 7 h, 28 h and 56 h. Two different types of precipitate phases were identified after aging. The results showed a clear correlation between the cooling time and the hardness, as well as the precipitate evolution.

The changes of the mechanical properties can be discussed purely as an effect of precipitation hardening, austenite reversion and solid solution hardening. This is because the EBSD data showed that no grain growth was observed during aging (Figure 3). Furthermore, all samples were machined from similar positions of the raw material, thus similar degrees of deformation and dislocation density after aging can be assumed.

The austenite fraction remained similar for all cooling times for the 15 h and 4 h aging time samples, while it increased for the samples with an aging time of 0 h. The austenite reversion is directly influenced by the matrix solute content of ferrite (Cr, Mo, Ti, Al) and austenite (Ni) stabilizers and the aging temperature. Various studies [13,14,25,26] show that higher aging temperatures can strongly enhance the austenite reversion kinetics in maraging steels. The results of the 0 h aging time samples show that the austenite reversion and the formation of precipitates occur independent of each other. This is shown by the simultaneously increasing volume fraction of precipitates and austenite, with increasing cooling time. This can be compared to results from Schnitzer et al. [23], where a PH13-8 Mo maraging steel was studied. They found that the formation of austenite in the beginning of aging is independent on the formation of precipitates.

The APT results (Figures 4 and 6) showed that the formation of precipitates is influenced the most by the cooling time for the samples aged for 0 h and 4 h. For a aging time of 15 h both types of precipitates (β -NiAl and η -Ni₃(Ti,Al)) are already well-developed before the cooling process. For this sample group the volume fraction of β -NiAl increases with increasing cooling time, while the volume fraction of η -Ni₃(Ti,Al) decreases. After 4 h of aging only a small volume fraction of η -Ni₃(Ti,Al) is precipitated, when a cooling time of 7 h or 28 h is used. If the cooling time is increased to 56 h, also the 4 h holding sample group showed fully-developed η -Ni₃(Ti,Al) precipitates with volume fractions similar to the 15 h aged sample group. The samples which were immediately cooled after reaching the aging temperature (0 h holding time) showed fully developed precipitates with 28 h and 56 h cooling time. For the 0 h aging time samples, 7 h of cooling time was sufficient to form only clusters and small particles with different morphology and a chemical composition with similar concentrations of Ni and Ti + Al (Figure 5b). From the observed precipitate evolution it can be concluded that the large Ni, Ti and Al rich particles that were observed in this condition correspond to early stages of η -Ni₃(Ti,Al), while the small spherical precipitates correspond to the β -NiAl phase. In addition to the β -NiAl precipitates, the 28 h cooled sample also showed rod-like precipitates with a chemical composition consisting of approximately equal parts of Ni and Ti + Al. This phase can be considered as an incomplete stage of η -Ni₃(Ti,Al). Compared to the samples with 15 h and 4 h aging time the η -Ni₃(Ti,Al) phase is not well-developed in the 0 h aging time samples and the volume fraction is comparatively low. This is because the formation of η -Ni₃(Ti,Al) typically requires longer aging times and forms in a higher temperature range than β -NiAl. In short, a longer cooling time results in a progressing precipitation reaction. If both types of precipitates are fully formed after holding (15 h sample group) the total volume fraction of precipitates remains constant, but a shift from a balanced distribution of η -Ni₃(Ti,Al) and β -NiAl to a distribution with more β -NiAl can be observed.

The results of the hardness testing showed that a clear trend between longer cooling time and an increased hardness exists (Figure 7). Already in the 0-7 condition the hardness increase compared to the SA + Q condition is significant. In this condition, the hardening effect stems from Ni, Ti and Al rich precipitates and clusters with various sizes and morphologies. The increased volume fraction and continued formation of precipitates after longer cooling times (28 h and 56 h) resulted in a hardness increase. Within the 4 h and

15 h sample groups the hardness also was increased by longer cooling times. The results showed that the 0-56 and the 4-56 conditions had the highest hardness out of all samples.

The calculation of the individual contributions to the hardness of the aged alloy showed that the precipitation hardening was within a range of about 350 HV to 380 HV for most conditions (Figure 8). Figure 9 shows the correlation between the volume fraction of precipitates and the precipitation hardening effect. A trend of increased precipitation hardening with a higher volume fraction of precipitates could be observed for all samples and within each aging time group. The strongest precipitation hardening effect was found in the 4-56, 15-28 and 15-56 conditions. This stems from the high volume fraction of precipitates found in these conditions. The weakest contribution of the precipitation hardening to the total hardness was observed for the 0 h aging time sample group. However, due to the comparatively low volume fraction of precipitates a high solute content is present in the matrix. Therefore, a higher contribution from solid solution hardening to the total hardness is present in these conditions. The high hardness that was observed in the 0-56 conditions stems from a well-balanced combination of precipitation hardening and solid solution hardening.

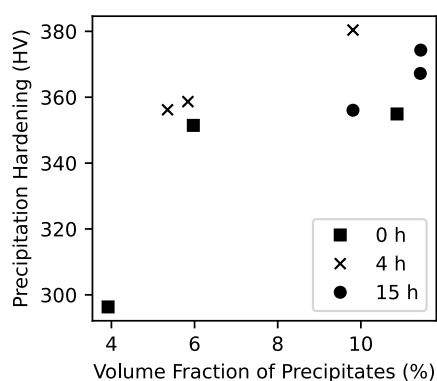


Figure 9. Precipitation hardening as function of the total volume fraction of precipitates (β -NiAl + η -Ni₃(Ti,Al)) for 0 h, 4 h and 15 h aging time.

The hardness contribution from the matrix, including grain size, dislocation hardening and softening due to reverted austenite, remained similar at about 100 HV for all aged conditions. The contribution of the reverted austenite to the matrix hardness was calculated using a linear mixture model, as proposed by Schnitzer et al. [27]. As all aged conditions showed similar austenite fractions, it can be concluded that the reversion from martensite to austenite is not a dominating mechanism for the hardness development of this steel (for an aging temperature of 510 °C).

The results of the Charpy impact tests showed that no correlation between the impact toughness and the cooling rate can be made using the selected heat treatments and experimental conditions. Most conditions showed a similar impact toughness with some fluctuation within each aging time group. No indication of embrittlement, caused by any of the heat treatments, was observed. However, the results suggest that a longer aging time can be beneficial to the impact toughness.

5. Conclusions

Following conclusions can be drawn on the influence of the cooling time on the precipitation hardening effect, impact toughness and microstructural evolution of a Co-free Fe-Ni-Cr-Mo-Ti-Al maraging steel:

- A slow cooling rate can be treated as an extension of the aging heat treatment, that uses lower temperatures. Longer cooling times can result in a higher volume fraction of precipitates and a higher hardness level.

- Solid solution hardening can play an important role for the total strength in under-peak aged precipitation hardened materials and peak hardness can be achieved with early stages of the precipitates.
- The highest hardness of this alloy can be achieved with a long cooling time and without significant loss of impact toughness. There is no clear correlation between the secondary aging effects (austenite reversion and change of impact toughness) and the cooling time.
- Aging heat treatments with a short aging time and long cooling times can be successfully used as an alternative to conventional aging heat treatments. Furthermore, no detrimental effect of long cooling times was found, when longer aging times were used. This knowledge can be useful for large work pieces, where air cooling can result in different cooling rates between the surface and the core of the work piece.

Author Contributions: Data curation, S.Z.; Formal analysis, S.Z.; Investigation, S.Z.; Methodology, S.Z.; Supervision, R.S.; Writing—original draft, S.Z.; Writing—review & editing, R.S. All authors have read and agreed to the published version of the manuscript.

Funding: The authors want to thank the European Research Fund for Coal and Steel (RFCS 847165) for providing the funding that made this study possible. Further thanks goes to the “iNiTiAl” consortium for providing the material.

Data Availability Statement: Access to the experimental data will be given out by the authors upon request.

Conflicts of Interest: The authors declare no conflict of interest.

References

1. Decker, R.F.; Novak, C.J.; Landig, T.W. Developments and projected trends in maraging steels. *JOM* **1967**, *19*, 60–66. [[CrossRef](#)]
2. Sha, W.; Guo, Z. *Maraging Steels: Modelling of Microstructure, Properties and Applications*, 1st ed.; Woodhead Publishing Ltd.: Cambridge, UK, 2009.
3. Wilm, A. Physikalisch-metallurgische Untersuchungen über magnesiumhaltige Aluminiumlegierungen. *Metallurgie* **1911**, *8*, 225.
4. Ardell, A.J. Precipitation hardening. *Metall. Trans. A* **1985**, *16*, 2131–2165. [[CrossRef](#)]
5. Ahmadi, M.R.; Povoden-Karadeniz, E.; Öksüz, K.I.; Falahati, A.; Kozeschnik, E. A model for precipitation strengthening in multi-particle systems. *Comput. Mater. Sci.* **2014**, *91*, 173–186. [[CrossRef](#)]
6. Schober, M.; Schnitzer, R.; Leitner, H. Precipitation evolution in a Ti-free and Ti-containing stainless maraging steel. *Ultramicroscopy* **2009**, *109*, 553–562. [[CrossRef](#)]
7. Li, K.; Yu, B.; Misra, R.D.; Han, G.; Liu, S.; Shang, C.J. Strengthening of cobalt-free 19Ni3Mo1.5Ti maraging steel through high-density and low lattice misfit nanoscale precipitates. *Mater. Sci. Eng. A* **2018**, *715*, 174–185. [[CrossRef](#)]
8. Leitner, H.; Schober, M.; Schnitzer, R.; Zinner, S. Strengthening behavior of Fe-Cr-Ni-Al-(Ti) maraging steels. *Mater. Sci. Eng. A* **2011**, *528*, 5264–5270. [[CrossRef](#)]
9. Schnitzer, R.; Schober, M.; Zinner, S.; Leitner, H. Effect of Cu on the evolution of precipitation in an Fe-Cr-Ni-Al-Ti maraging steel. *Acta Mater.* **2010**, *58*, 3733–3741. [[CrossRef](#)]
10. Kürnsteiner, P.; Wilms, M.B.; Weisheit, A.; Barriobero-Vila, P.; Jäggle, E.A.; Raabe, D. Massive nanoprecipitation in an Fe-19Ni-xAl maraging steel triggered by the intrinsic heat treatment during laser metal deposition. *Acta Mater.* **2017**, *129*, 52–60. [[CrossRef](#)]
11. Jiang, S.; Wang, H.; Wu, Y.; Liu, X.; Chen, H.; Yao, M.; Gault, B.; Ponge, D.; Raabe, D.; Hirata, A.; et al. Ultrastrong steel via minimal lattice misfit and high-density nanoprecipitation. *Nature* **2017**, *544*, 460–464. [[CrossRef](#)]
12. Zhang, C.; Wang, C.; Zhang, S.L.; Ding, Y.L.; Ge, Q.L.; Su, J. Effect of aging temperature on the precipitation behavior and mechanical properties of Fe-Cr-Ni maraging stainless steel. *Mater. Sci. Eng. A* **2021**, *806*, 140763. [[CrossRef](#)]
13. Nakagawa, H.; Yokota, H.; Miyazaki, T. Effects of aging temperature on the microstructures and mechanical properties of a precipitation hardening martensitic stainless steel containing retained austenite. *J. Mater. Sci.* **2000**, *35*, 2245–2253. [[CrossRef](#)]
14. Conde, F.F.; Escobar, J.D.; Oliveira, J.P.; Béres, M.; Jardini, A.L.; Bose, W.W.; Avila, J.A. Effect of thermal cycling and aging stages on the microstructure and bending strength of a selective laser melted 300-grade maraging steel. *Mater. Sci. Eng. A* **2019**, *758*, 192–201. [[CrossRef](#)]
15. Zhang, H.; Ji, X.; Ma, D.; Tong, M.; Wang, T.; Xu, B.; Sun, M.; Li, D. Effect of aging temperature on the austenite reversion and mechanical properties of a Fe-10Cr-10Ni cryogenic maraging steel. *J. Mater. Res. Technol.* **2021**, *11*, 98–111. [[CrossRef](#)]
16. Niu, M.C.; Yang, K.; Luan, J.H.; Wang, W.; Jiao, Z.B. Cu-assisted austenite reversion and enhanced TRIP effect in maraging stainless steels. *J. Mater. Sci. Technol.* **2022**, *104*, 52–58. [[CrossRef](#)]
17. Wang, M.; Tasan, C.C.; Ponge, D.; Raabe, D. Spectral TRIP enables ductile 1.1 GPa martensite. *Acta Mater.* **2016**, *111*, 262–272. [[CrossRef](#)]

18. Gault, B.; Moody, M.; Cairney, J.M.; Ringer, S.P. *Atom Probe Microscopy*; Springer: New York, NY, USA, 2012.
19. Zeisl, S.; Lassnig, A.; Hohenwarter, A.; Mendez-Martin, F. Precipitation behaviour of a Co-free Fe-Ni-Cr-Mo-Ti-Al maraging steel after severe plastic deformation. *Mater. Sci. Eng. A* **2021**, *833*, 142416. [[CrossRef](#)]
20. Jäggle, E.A.; Choi, P.P.; Raabe, D. The maximum separation cluster analysis algorithm for atom-probe tomography: Parameter determination and accuracy. *Microsc. Microanal.* **2014**, *20*, 1662–1671. [[CrossRef](#)]
21. Galindo-Nava, E.I.; Rivera-Díaz-Del-Castillo, P.E. A model for the microstructure behaviour and strength evolution in lath martensite. *Acta Mater.* **2015**, *98*, 81–93. [[CrossRef](#)]
22. Warlimont, H.; Martienssen, W. *Springer Handbooks of Materials Data*, 2nd ed.; Springer Nature: Cham, Switzerland, 2018.
23. Schnitzer, R.; Radis, R.; Nöhrer, M.; Schober, M.; Hochfellner, R.; Zinner, S.; Povoden-Karadeniz, E.; Kozeschnik, E.; Leitner, H. Reverted austenite in PH 13-8 Mo maraging steels. *Mater. Chem. Phys.* **2010**, *122*, 138–145. [[CrossRef](#)]
24. Galindo-Nava, E.I.; Rainforth, W.M.; Rivera-Díaz-del Castillo, P.E. Predicting microstructure and strength of maraging steels: Elemental optimisation. *Acta Mater.* **2016**, *117*, 270–285. [[CrossRef](#)]
25. Escobar, J.D.; Faria, G.A.; Wu, L.; Oliveira, J.P.; Mei, P.R.; Ramirez, A.J. Austenite reversion kinetics and stability during tempering of a Ti-stabilized supermartensitic stainless steel: Correlative in situ synchrotron X-ray diffraction and dilatometry. *Acta Mater.* **2017**, *138*, 92–99. [[CrossRef](#)]
26. Kooiker, H.; Perdahcıođlu, E.S.; van den Boogaard, A.H. Combined athermal and isothermal martensite to austenite reversion kinetics, experiment and modelling. *Mater. Des.* **2020**, *196*, 109124. [[CrossRef](#)]
27. Schnitzer, R.; Zickler, G.A.; Lach, E.; Clemens, H.; Zinner, S.; Lippmann, T.; Leitner, H. Influence of reverted austenite on static and dynamic mechanical properties of a PH 13-8 Mo maraging steel. *Mater. Sci. Eng. A* **2010**, *527*, 2065–2070. [[CrossRef](#)]

Publication III

The role of alloying elements in NiAl and Ni₃Ti strengthened Co-free maraging steels

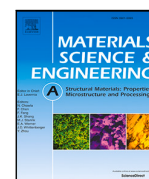
S. Zeisl, A. Landefeld, N. Van Steenberge, Y. Chang and R. Schnitzer

Materials Science and Engineering: A **861**, 144313 (2022)



Contents lists available at ScienceDirect

Materials Science & Engineering A

journal homepage: www.elsevier.com/locate/msea

The role of alloying elements in NiAl and Ni₃Ti strengthened Co-free maraging steels

S. Zeisl^{a,*}, A. Landefeld^a, N. Van Steenberge^b, Y. Chang^c, R. Schnitzer^a^a Department of Materials Science, Montanuniversität Leoben, Franz-Josef Straße 18, 8700 Leoben, Austria^b OnderzoekCentrum voor de Aanwending van Staal, Technologiepark Techlane A4C, 9052 Zwijnaarde, Belgium^c Steel Institute, RWTH Aachen University, Intzestraße 1, 52072 Aachen, Germany

ARTICLE INFO

Keywords:

Maraging steels
Atom probe tomography
Alloy design
X-ray diffraction
Intermetallic precipitates

ABSTRACT

Some precipitation hardened steels use a combination of the intermetallic β -NiAl and η -Ni₃Ti phases to achieve a beneficial combination of ultra-high strength and toughness. The age-hardening in such steels is a complex process that includes the simultaneous formation of precipitates and reverted austenite. The phase constitution and volume fraction of the precipitates strongly depends on the content of the alloying elements, such as Ti, Al, Cr and Mo. By using a step-wise alloy design scheme and high-resolution characterization methods this study seeks to reveal the influence of Ti and Al variations as well as of Cr and Mo on the precipitation hardening and austenite reversion for Co-free maraging steels based on the Fe-12Ni alloy system. It was found that Cr plays a major role in promoting the precipitation of the η -Ni₃Ti phase and simultaneously increases strength and toughness, Ti and Al variations can change the balance between η -Ni₃Ti and β -NiAl precipitates and Mo significantly promotes austenite reversion.

1. Introduction

Maraging steels belong to the group of precipitation hardened high-strength steels and provide a combination of high strength and satisfactory toughness. Because of their well-balanced properties they are often used in military, aerospace and sport applications [1]. Typical maraging steels consist of a soft Ni-martensite with embedded nano-sized precipitates that are crucial for the strength of the material [2]. In addition, reverted and retained austenite can be present depending on the chemical composition and the applied heat treatment [3]. Reverted austenite is formed during aging with either a lath-like (i.e. film-like) or a blocky morphology at low or high aging temperature, respectively [4].

The chemical composition determines which types of phases are precipitated, and we can distinguish between two classes of maraging steels: Co-alloyed and Co-free maraging steels [1]. Co is an alloying element that lowers the nucleation barrier for certain types of intermetallic phases, e.g. the Fe₂Mo phase or the Fe₇Mo₆ phase, which is a characteristic phase for Co-alloyed maraging steels [5]. Co-free maraging steel variants were developed out of necessity in the 1970s as a result of rising Co prices. They are typically hardened by β -NiAl or η -Ni₃Ti precipitates, but other types of phases such as the G or R phases have been identified as well [6,7].

The conventional heat treatment route for maraging steels consists of solution annealing and aging. Solution annealing is typically performed at temperatures around 850 °C – 950 °C in the austenite region, and afterwards the samples are quenched in air or water. Depending on the chemical composition, the martensite finish temperature can be lower than the quenching temperature in which case a subsequent cryogenic treatment is necessary to reduce the fraction of retained austenite. For instance: Zhirafar et al. [8] were able to reduce the fraction of retained austenite from 5.7% to 4.2% using a cryogenic treatment at –196 °C. Finally, the solution annealed maraging steel is aged at temperatures between 400–600 °C where it is hardened by the precipitation of intermetallic phases.

Although Co-free maraging steels with a combination of η -Ni₃Ti and β -NiAl precipitates were reported in the past [9,10] it is still unclear how different concentrations of Ti and Al change the volume fractions of both phases. Furthermore, the effect of Cr and Mo on the formation of η -Ni₃Ti and β -NiAl is not well established in the current literature. This paper seeks to elucidate the synergistic effects of the two intermetallic phases η -Ni₃Ti and β -NiAl, their interactions with Cr and Mo as alloying elements and the effect of different Ti and Al concentrations on the microstructure, evolution of precipitates as well as strength and toughness. In this work, starting with a base system of only Fe and 12 wt.% Ni, alloying elements were systematically added

* Corresponding author.

E-mail address: stefan.zeisl@unileoben.ac.at (S. Zeisl).<https://doi.org/10.1016/j.msea.2022.144313>

Received 26 September 2022; Received in revised form 3 November 2022; Accepted 6 November 2022

Available online 9 November 2022

0921-5093/© 2022 The Author(s). Published by Elsevier B.V. This is an open access article under the CC BY license (<http://creativecommons.org/licenses/by/4.0/>).

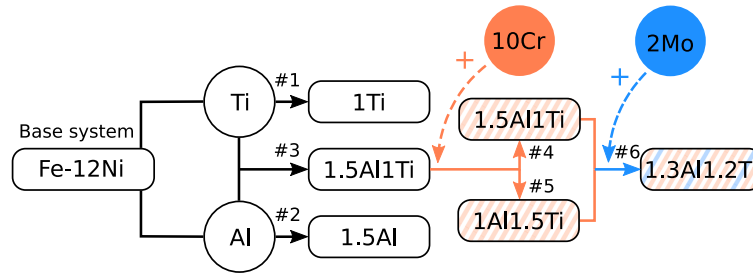


Fig. 1. Overview of the alloy selection scheme used in this study. The concentrations of the precipitate forming elements Al and Ti and the additional alloying elements Cr and Mo are shown in wt.%.

Table 1
Concentration of the alloying elements (in wt.% and at.%) of each alloy used in this study. The chemical composition of all alloys is balanced with Fe.

Alloy number - Name	wt.%					at.%				
	Ni	Cr	Mo	Al	Ti	Ni	Cr	Mo	Al	Ti
#1 - 1Ti	11.8				0.9	11.27				1.05
#2 - 1.5Al	11.5			1.4		10.83			2.87	
#3 - 1.5Al,1Ti	11.6			1.7	0.9	10.88			3.46	1.03
#4 - 10Cr,1.5Al,1Ti	11.9	9.9		1.6	1.0	11.1	10.42		3.24	1.14
#5 - 10Cr,1Al,1.5Ti	11.9	10		0.9	1.4	11.17	1.59		1.83	1.61
#6 - 10Cr,2Mo,1.3Al,1.2Ti	12.1	10	2.1	1.3	1.2	11.41	10.65	1.21	2.67	1.39

and six resulting alloys were investigated to gain understanding on how the chemical composition of a Co-free maraging alloy can be fine-tuned to obtain the desired mechanical properties.

2. Materials and methods

Six different alloys were synthesized for the present study according to the alloy design scheme displayed in Fig. 1. The alloys were produced by the Metals Processing Centre Gent (Gent, Belgium). The base system was an alloy of Fe with 12 wt.% Ni. In the first step 1 wt.% Ti and 1.5 wt.% Al were added (alloy 1 and 2) to produce materials that can be age-hardened with either η -Ni₃Ti or β -NiAl, respectively. For alloy 3 Ti and Al were both added to test the combination of η -Ni₃Ti and β -NiAl precipitates. In the next step 10 wt.% Cr and 2 wt.% Mo were added to improve the corrosion resistance and to study the influence on the microstructure, mechanical properties and the formation of the precipitates. Cr was added to obtain alloys 4 and 5 and Cr+Mo was added to obtain alloy 6. In alloys 4 to 6 the Ti and Al concentrations were varied between 1 wt.% and 1.5 wt.% to understand how Ti and Al variations effect the volume fraction of the η and the β phase. The chemical composition of the alloys was measured with X-ray fluorescence and is shown in Table 1.

The alloys were produced by vacuum induction melting and cast into ingots with a mass of 100 kg, which were hot-rolled (1250 °C) into sheets with a thickness of 8 mm. The sheets were solution annealed at 850 °C for a duration of 90 min. Alloys 4, 5 and 6 were subject to a cryogenic treatment at -80 °C for 16 h. Each alloy was aged at 510 °C for 16 h, a temperature and time combination that was selected based on preliminary tests.

Tensile tests were performed to obtain the ultimate tensile strength using a Instron 5500 universal testing machine with one test per condition. The tensile test specimens, which were manufactured from sheet material, had a circular cross-section with a diameter of 3.8 mm and a gauge length of 25 mm in transverse direction. Charpy impact toughness tests were performed to obtain the impact toughness of all conditions. A Zwick PSW750 machine was used to perform the tests at room temperature. One test per condition was performed. The Charpy test specimens were manufactured in transverse direction with a length of 55 mm, a cross-section of 8.7 × 10 mm² and a notch radius of 0.25 mm.

The martensite block size, which can be treated as the effective grain-size of maraging steels [11,12], was measured with electron backscatter diffraction (EBSD) using an Oxford EBSD detector and evaluated with Matlab and the MTEX EBSD analysis package. An orientation mismatch of 10.5° was used to define the martensite blocks. The austenite fraction was measured with X-ray diffraction (XRD) in a Bruker Advanced D8 DaVinci instrument with Cu-K_α radiation and evaluated using LaB₆-calibrated Rietveld refinement. Transmission electron microscopy (TEM) was performed in a Talos F200X G2 microscope. The results were analyzed using the Velox Imaging Software 2.5. TEM was used to visualize the martensite matrix and precipitates on a sub-micrometer scale and as a correlative tool to atom probe tomography (APT). The matrix and the η -Ni₃Ti particles were characterized using the bright field detector of the scanning TEM (STEM) and energy dispersive X-ray (EDX) mappings, the β -NiAl precipitates were visualized using a high-angle annular dark-field imaging (HAADF) detector.

The metallographic samples that were used for EBSD and XRD were prepared using standard polishing methods. The EBSD samples were finished by polishing with a solution of colloidal silica (0.05 μm particle size) to ensure a deformation-free surface. Transmission electron microscopy (TEM) samples were prepared by twin-jet polishing using a Struers A2 electrolyte.

APT was used to characterize the distribution and the chemistry of precipitates. The measurements were performed in a LEAP 3000X HR in the laser assisted mode. A pulse frequency of 250 kHz, a laser energy of 0.3 nJ, a detection rate of 1% and a specimen temperature of 60 K were used. The preparation of the APT specimens was performed with a standard 2-step electropolishing method [13]. The first polishing step was performed using a solution of 25 vol% of perchloric acid in glacial acetic acid and the final step was performed with a 2% solution of perchloric acid in 2-butoxyethanol. The IVAS software suite (version 3.6.14) was used to analyze the atom probe data. For the statistical evaluation of the precipitates, a cluster search based on the DBSCAN algorithm was used. The volume fraction F_v of precipitates was calculated according to [14]:

$$F_v = \frac{N \cdot v \cdot C}{V_{total}} \tag{1}$$

N is the total number of ranged ions in the clusters, v the volume per atom according to the unit cell of the precipitate phase, V_{total} the total

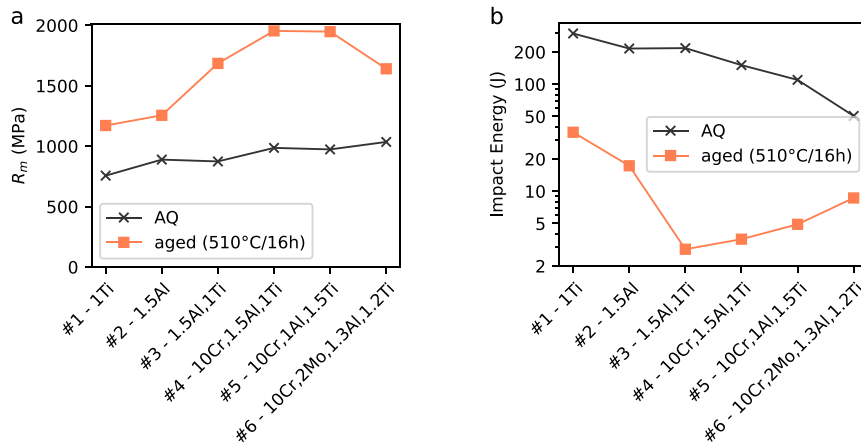


Fig. 2. Tensile strength R_m (a) and impact energy (b) of all alloys in the as quenched (AQ) and aged condition.

Table 2 DBSCAN algorithm parameters for each alloy and type of precipitate used for cluster detection.

Alloy	η -Ni ₃ Ti			β -NiAl		
	Element	d_{Max} (nm)	N_{Min}	Element	d_{Max} (nm)	N_{Min}
Alloy 1	Ti	1.0	100			
Alloy 2				Al	0.75	50
Alloy 3	Ti	1.05	2300	Al	0.87	50
Alloy 4	Ti	1.15	1000	Al	0.82	150
Alloy 5	Ti	1.05	1200	Al	0.82	150
Alloy 6	Ti,Al	1.05	2000	Al	0.82	150

volume of the measurement and C a correction factor that accounts for the detector efficiency (37%).

The cluster search was performed with a nearest-neighbor order of $k = 10$. The parameters d_{Max} and N_{Min} for the DBSCAN algorithm are presented in Table 2. d_{Max} is the maximum pair distance between adjacent atoms and N_{Min} is the minimal cluster size. The erosion and envelope distance were chosen to be equal to d_{Max} . d_{Max} was determined using a procedure described by Stephenson et al. [15].

3. Results

3.1. Mechanical properties

Tensile tests and Charpy impact tests were performed to determine the strength and toughness of the alloys. Fig. 2a shows the tensile strength of all alloys in the as-quenched and aged condition. The strength of the as-quenched samples increased from alloy 1 (756 MPa) to alloy 6 (1048 MPa), which corresponds to the addition of alloying elements, i.e. to the combination of Ti and Al and addition of Cr and Mo. In the aged condition all alloys showed a significantly increased strength compared to the as-quenched condition. This strength increase was the lowest for alloys 1 and 2 (366 MPa and 414 MPa, respectively), which only contained either Ti or Al as an addition to the base alloy. The combination of Ti and Al (alloy 3) resulted in a strength increase of 811 MPa. The addition of Cr (alloys 4 and 5) increased the strength further compared to alloy 3. The variation of Ti and Al between alloys 4 and 5 did not affect the tensile strength significantly. The strength increase was 974 MPa for alloy 4 and 966 MPa for alloy 5. Alloy 6 (alloyed with Mo) showed a lower strength in the aged condition than alloys 4 and 5. Compared to the as-quenched condition the strength increase was 592 MPa for alloy 6. In the aged condition the highest tensile strength was measured for alloys 4 and 5 (1954 MPa and 1948 MPa respectively) and the lowest for alloys 1 and 2 (1171 MPa

and 1255 MPa respectively). Alloy 3 had a tensile strength of 1685 MPa and alloy 6 had a tensile strength of 1640 MPa in the aged condition.

Fig. 2b shows the impact energy of all alloys in the as-quenched and aged condition. In the as-quenched condition the impact energy decreased in two steps. First, with the addition of Cr and second with the addition of Mo. The impact energy of alloys 1, 2 and 3 were 298 J, 215 J and 217 J respectively. Alloys 4 and 5 had an impact energy of 150 J and 109 J respectively and alloy 6 had an impact energy of 51 J. The aged alloys had a significantly decreased impact energy compared to the as-quenched condition. The highest impact energy of the aged conditions was observed for alloy 1 with 35 J and alloy 2 with 17 J while the lowest impact energy was found for alloy 3 with 2.9 J. The addition of Cr improved the toughness of the aged material slightly. Between the Cr-alloyed materials, the variant with a higher Ti concentration (alloy 5, 4.9 J) showed an increased impact energy compared to the variant with lower Ti concentration (alloy 4, 3.6 J). With the addition of Mo (alloy 6) the toughness was improved further as the impact energy increased to 8.7 J.

3.2. Microstructural characterization

The matrix of the material was characterized with EBSD and XRD, which were used to obtain the mean block size and the fraction of austenite, respectively. Fig. 3a–c shows the inverse pole figures that correspond to the microstructure of alloys 4, 5 and 6 in the as-quenched condition. The boundaries show a 10.5° orientation mismatch, representing martensite blocks. The mean martensite block size of alloy 4 was 6.4 μm, from alloy 4 to 5 it increased to 7.21 μm and from 5 to 6 to 10.71 μm. Furthermore, small grains of retained austenite were identified in all alloys (white grains in Fig. 3). In alloy 6 (Fig. 3c) two bands of large interconnected grains of retained austenite were observed in addition to the inter-granular grains of retained austenite that were observed in alloys 4 and 5 (Fig. 3a,b).

Fig. 4a shows the austenite fraction for all alloys and conditions. In the as-quenched condition alloys 1–5 showed no notable amounts of retained austenite. Alloy 6 (addition of Mo) had a fraction of retained austenite of 2.5%. The aging heat treatment affected the formation of reverted austenite differently for each alloy. Alloys 1 to 3 had a fraction of less than 1.5% austenite in the aged condition. The addition of Cr increased the fraction of reverted austenite slightly, which was similar for alloy 4 and alloy 5. Alloy 4 had an austenite fraction of 2.1% and alloy 5 of 2.9%. The fraction of reverted austenite increased significantly with alloy 6 (addition of Mo), for which the total fraction of austenite (retained and reverted) was measured as 13.6%.

In Fig. 5a–c the TEM micrographs of alloy 5 in the aged condition are displayed. Fig. 5a shows individual martensite laths and

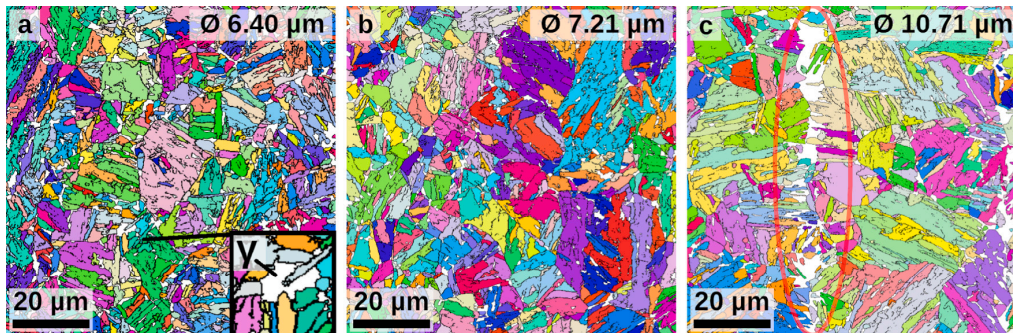


Fig. 3. Inverse pole figures of alloys 4–6 (a–c) showing the microstructure and the mean block size of the alloys in the as-quenched condition. Austenite grains are presented in white, as shown in the inset of (a). The marked area in (c) shows a column of retained austenite. (For interpretation of the references to color in this figure legend, the reader is referred to the web version of this article.)

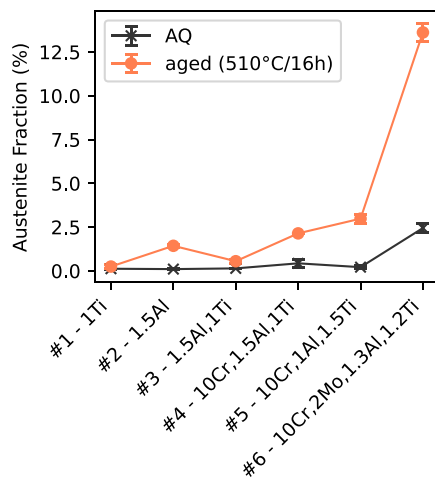


Fig. 4. Austenite fraction of all alloys in the as-quenched and aged conditions (510 °C for 16 h).

lath-like reverted austenite, which was observed along the martensite lath boundaries. The width of the martensite laths was approximately between 250 nm and 400 nm. In Fig. 5b the rod-like Ni_3Ti precipitate phase was identified. The inset in Fig. 5b shows an EDX mapping of Ti, which highlights the Ni_3Ti precipitates. In Fig. 5c HAADF imaging was used to show the NiAl precipitates, which are displayed as dark and spherical spots and highlighted in the inset of Fig. 5c. The mean length of the Ni_3Ti precipitates was about 20 nm and the mean diameter of the NiAl precipitates was about 5 nm.

Fig. 6 shows iso-concentration surfaces of the APT reconstructions for alloys 4 to 6. In all three alloys two types of precipitates were identified: a B2-type $\beta\text{-NiAl}$ phase, which is represented by 30 at.% Ni+Al iso-concentration surfaces, and a rod-like $\eta\text{-Ni}_3\text{Ti}$ phase, which is represented by 60 at.% Ni+Ti+Al iso-concentration surfaces. The iso-concentration surfaces showed that the number of NiAl particles decreased from alloy 4 to alloy 6, which corresponds to an increasing Ti concentration (alloy 5) and the addition of Mo (alloy 6). The morphology of the precipitates was well-defined for alloys 4 and 5, for which the NiAl and the Ni_3Ti phase were spherical and rod-like, respectively. In alloy 6 small disk-shaped precipitates (also represented by 30 at.% Ni+Al iso-concentration surfaces) with a chemical composition corresponding to the $\eta\text{-Ni}_3\text{Ti}$ phase were observed in addition to the spherical NiAl-type precipitates. Fig. 6d shows a Mo- and Fe-rich phase that was observed in alloy 6 at the precipitate–matrix interface

of a $\eta\text{-Ni}_3\text{Ti}$ particle. For alloy 5 the data from the cluster search was used to evaluate the mean length of $\eta\text{-Ni}_3\text{Ti}$ precipitates and the mean diameter of $\beta\text{-NiAl}$ precipitates. The mean length of the η phase was found to be $35.3 \text{ nm} \pm 16.5 \text{ nm}$ and the mean diameter of the β phase was found to be $6.7 \text{ nm} \pm 1.2 \text{ nm}$.

Fig. 7a shows the volume fraction of the η phase and of the NiAl phase for each alloy. The volume fraction of η increased from alloy 3 to alloy 4 and 5 with the addition of Cr. Alloy 5 with a Ti concentration of 1.5 wt.% showed a higher volume fraction of η than alloy 4 that had a Ti concentration of 1.0 wt.% Ti. Furthermore, the $\eta\text{-Ni}_3\text{Ti}$ volume fraction increased from alloy 5 to alloy 6 with the addition of Mo. Fig. 7b shows the concentration of the precipitating elements (Ni, Ti and Al) in the matrix phase. The Ni concentration in the matrix decreases with the addition of Cr and is similar for alloys 4, 5 and 6. The matrix concentration of Ti and Al was higher in alloy 3 than in the other alloys, which were similar.

Fig. 8 shows the proxigrams of the Ni_3Ti phase for alloy 1 and alloys 3–6. The proxigrams revealed that alloys 1, 3, 4 and 5 showed a Ni concentration close to 75%, while alloy 6 showed a lower Ni concentration within the precipitate. Additionally, a pile-up of Al was observed at the precipitate–matrix interface for alloys 3–6. Fig. 9a shows the Al concentration across the $\eta\text{-Ni}_3\text{Ti}$ precipitate–matrix interface to a greater detail than Fig. 8. The pile-up of Al was found to be the strongest for alloys 5 and 6, which corresponds to the alloy with Cr and 1.5 wt.% Ti and the alloy with Cr, Mo and 1.3 wt.% Al, respectively. Moreover, the Al concentration within the precipitates increased with the addition of Cr (alloy 4 and 5) and with the addition of Mo (alloy 6). Fig. 9b shows the proxigram that corresponds to the 5 at.% Mo iso-concentration surfaces in Fig. 6d. The particle was rich in Fe, Mo and Cr, and fitted the stoichiometry of a $(\text{Fe,Cr})_7(\text{Mo,Cr})_6$ phase.

4. Discussion

The results of mechanical testing (Fig. 2) showed that the tensile strength of the as-quenched samples increased as the concentration of alloying elements increased. After the solution annealing heat treatment and the subsequent quenching all alloying elements are dissolved within the martensite, resulting in a higher tensile strength due to an increased contribution from solid solution strengthening. At the same time, the high fraction of austenite (alloy 6) and a larger martensite block size (alloys 4 to 6) are detrimental to the total strength. While alloys 1 to 5 had negligible fractions of retained austenite alloy 6 had an austenite fraction of 2.5% in the as-quenched condition. The EBSD experiments showed that the martensite block size increased from alloy 4 to 6. According to earlier studies, the martensite block size can be understood as the effective strength controlling feature for grain size strengthening in maraging steels [11,12]. Moreover, a related study by Zeisl et al. [16] showed that the aging parameters in the present

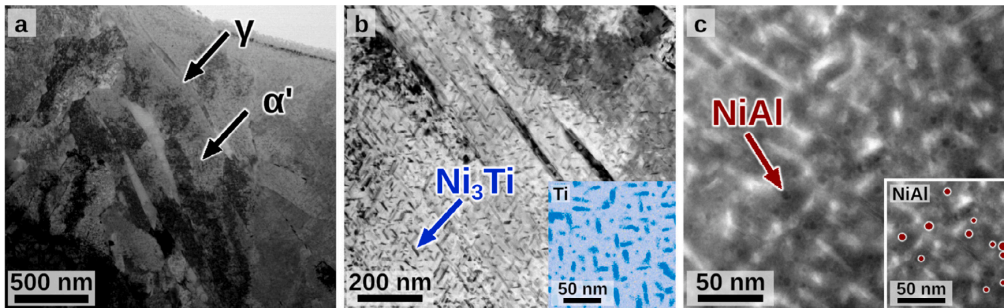


Fig. 5. (a), (b) STEM and (c) HAADF micrographs of alloy 5 (aged at 510 °C for 16 h) showing martensite laths (α'), reverted austenite (γ) and the rod-like Ni_3Ti and spherical NiAl precipitate phases. The inset in (b) shows the EDX mapping of Ti and the inset in (c) shows the micrograph of (c), but with some NiAl particles highlighted in dark red. (For interpretation of the references to color in this figure legend, the reader is referred to the web version of this article.)

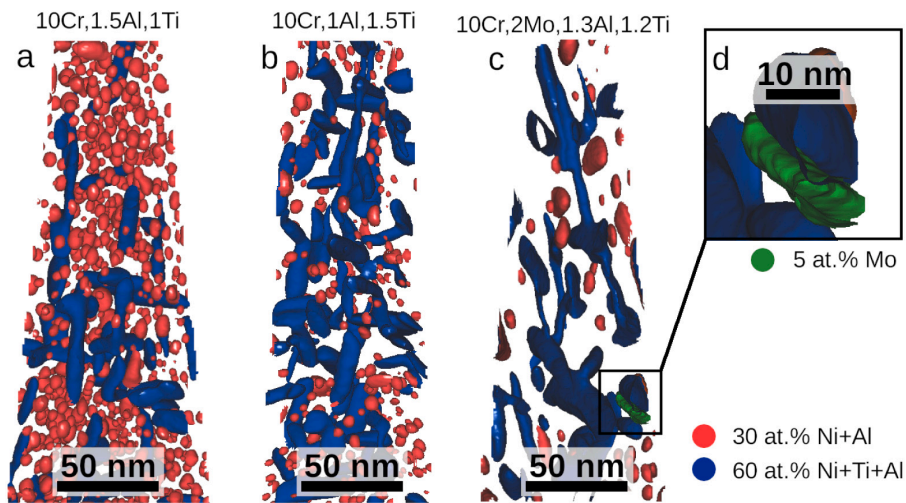


Fig. 6. Iso-concentration surfaces of 4 to 6 (a–c) in the condition aged at 510 °C for 16 h.

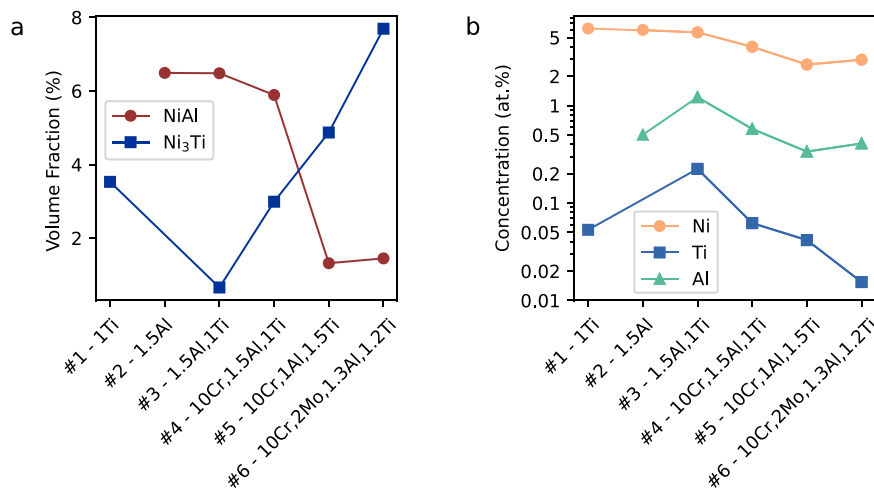


Fig. 7. (a) Volume fraction of the Ni_3Ti phase and the NiAl phase for each alloy in the condition aged at 510 °C for 16 h. (b) Concentration of the precipitate forming elements (Ni, Ti and Al) in the matrix phase (in at.%).

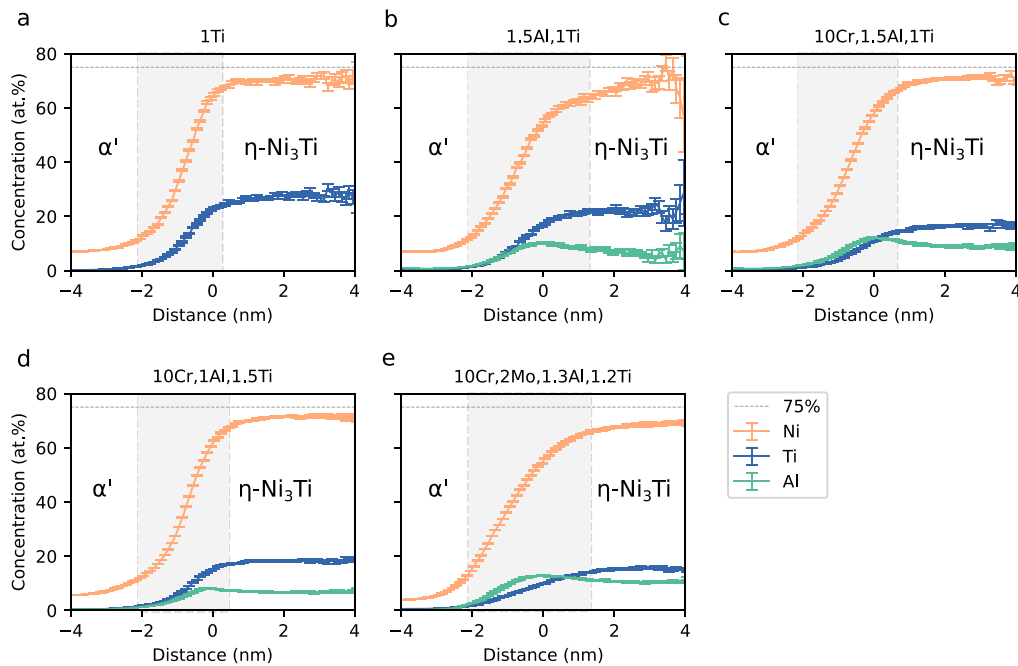


Fig. 8. Proxigram showing the change of the Ni, Ti and Al concentration (in at.%) across the precipitate–matrix (η - α') interface for alloys 1 (a) and 3–6 (b–e) in the condition aged at 510 °C for 16 h.

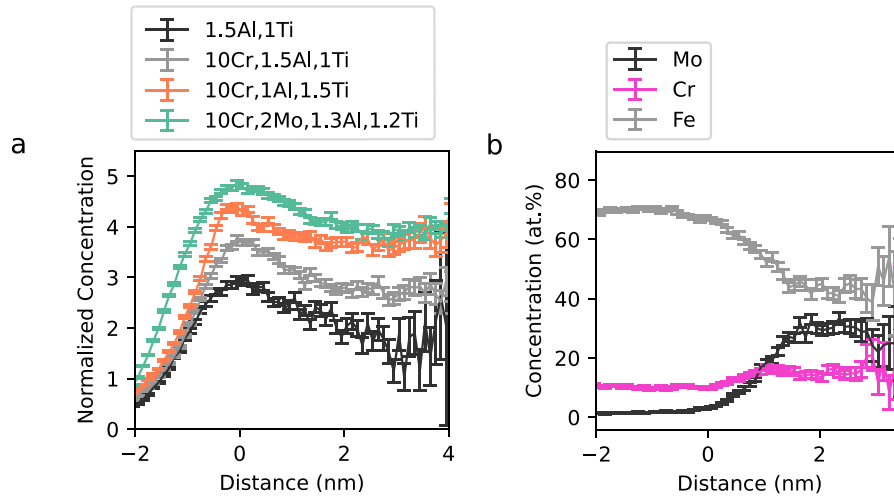


Fig. 9. (a) Al concentration, normalized to the bulk concentration of Al, across the precipitate–matrix (η - α') interface for alloys 3–6 in the condition aged at 510 °C for 16 h. (b) Proxigram of the Mo-rich phase (5 at.% Mo iso-concentration surface) in alloy 6 (10Cr,2Mo,1.3Al,1.2Ti).

study (510 °C for 16 h) do not lead to any measurable grain growth for this type of maraging steels. A higher austenite fraction and a larger martensite block size contribute to a smaller tensile strength, but the difference between the alloys was relatively small in the as-quenched condition.

The ternary alloys (alloy 1 and 2) had a similar strength in the aged condition (510 °C/16 h). For those two alloys the APT results showed a smaller volume fraction of η -Ni₃Ti precipitates in alloy 1 than β -NiAl precipitates in alloy 2. This suggests that η -Ni₃Ti has a higher strength contribution per volume fraction than β -NiAl. The tensile strength of alloys 3–5 aged at 510 °C increased with the addition of Cr. The high strength increase from alloy 3 to alloy 4 (R_m of 1685 MPa vs.

1954 MPa, respectively) can be explained by two effects: Firstly, the strong increase of the volume fraction of η -Ni₃Ti, which was observed after the addition of Cr. And secondly, the fact that the volume fraction of the β -NiAl phase did not change significantly between the aged alloys 3 and 4. Alloys 4 and 5 had a similar tensile strength and strength increase (compared to the as-quenched condition), but the observations from APT showed that the volume fractions of the precipitates were different. Alloy 5 had a higher volume fraction of η -Ni₃Ti and a lower volume fraction of β -NiAl than alloy 4. Alloys 4 and 5 differ in terms of the Ti and Al concentration, which was 1.5 wt.% Al and 1.0 wt.% Ti for alloy 4 and 1.5 wt.% Ti and 1.0 wt.% Al for alloy 5. The decrease of the volume fraction of the β phase was larger than the increase of

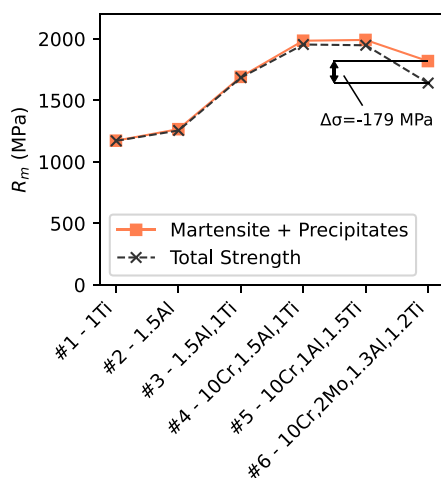


Fig. 10. Comparison of the measured tensile strength (total strength) of the aged alloys with the strength if no austenite was present (martensite + precipitates).

volume fraction of the η phase while retaining a similar strength. Going from alloy 4 to alloy 5 the microstructure moved from having an excess of β -NiAl particles in the microstructure to having an excess of η -Ni₃Ti.

It can be concluded that the η -Ni₃Ti phase is a stronger contributor to precipitation hardening than the β -NiAl phase and that the volume fraction of η -Ni₃Ti can be adjusted by changing the Ti concentration. It was also observed that adding Mo to this alloy system causes a strength decrease in the aged condition (16 h at 510 °C). The iso-concentration surfaces (see Fig. 6) show a clear visual difference of the precipitates in alloy 6 compared to alloy 4 and 5. The η -Ni₃Ti particles in alloy 6 appeared to be larger than in alloys 4 and 5 and the number of spherical β -NiAl particles is significantly smaller compared to the other alloys. It is possible that 510 °C and 16 h are not the optimal temperature and time for the aging of this alloy. Apart from the effects of precipitation strengthening, the strength decrease of alloy 6 can be explained by the high fraction of reverted austenite in the aged condition, as seen in Fig. 4. Schnitzer et al. [17] used a linear mixture rule to obtain the yield strength of only the martensite with precipitates. Fig. 10 shows the tensile strength of the martensite with precipitates, obtained with the linear mixture rule, compared to the measured tensile strength. For the strength of austenite (R_m) a value of 500 MPa [17] was used. The presence of austenite decreases the tensile strength of alloy 6 by 179 MPa. This comparison shows that although the precipitation strengthening effect in this alloy is lower than in alloys 4 and 5, the difference is smaller than the measured tensile strength suggests. The results of EBSD showed that alloy 6 had a larger martensite block size compared to alloys 4 and 5 in the as-quenched condition. A smaller contribution from grain size strengthening also contributes to the lower strength in alloy 6. An estimation using the Hall–Petch equation for lath martensite $\sigma_{GS} = \frac{300}{\sqrt{d_{Block}}}$ [18] shows that the strength contribution due to the block size is 20 MPa higher in alloy 5 than in alloy 6 when the block size from the as-quenched condition is used (see Fig. 3).

In the as-quenched condition, the impact toughness of the alloys decreased significantly with the addition of Cr, the addition of Mo and also with an increased Ti concentration (Fig. 2). This observation correlates well with the increasing strength in the as-quenched condition. For alloys 4 to 6 the increasing martensite block size (see Fig. 3a–c) can also be a contributing factor. For the aged material, alloy 3 showed the lowest impact toughness in the aged condition. The ternary alloys with either only Ti or Al (alloy 1 and 2 respectively) showed a significantly higher impact toughness than the other aged alloys. However, this high impact toughness stems from the lower tensile strength of alloy 1 and

2. A simultaneous increase of the impact toughness and the tensile strength in the aged condition was achieved by the addition of Cr (alloys 4 and 5). With the addition of Mo (alloy 6) the impact toughness was increased further, but the tensile strength decreased. This trend correlates to the fraction of reverted austenite that was observed for alloys 4 to 6 (see Fig. 4). TEM investigations of alloy 5 (aged at 510 °C, see Fig. 5) showed that the reverted austenite forms at the martensite lath boundaries, so-called lath-like reverted austenite. This is consistent with the results from earlier studies [4,19–21], which found a lath-like morphology of austenite for similar aging temperatures. Schnitzer et al. [20] found that the fracture elongation and ductility is increased when more reverted austenite is present. Reverted austenite improves the toughness of maraging steels by the TRIP (transformation induced plasticity) effect [22,23].

The fraction of retained austenite in the as-quenched condition is negligible for alloys 1 to 5. Alloy 6 (Mo-alloyed) showed a notable fraction of retained austenite, with 2.5%. Wu et al. [24] tested steels with 11 different chemical compositions and found that the fraction of retained austenite is inversely correlated to the predicted martensite start temperature M_s . They also found that the fraction of retained austenite increased with increasing Cr concentration, Ni concentration and with the presence of Mo, which is in agreement with the results of this study. For this steel the martensite start temperature can be estimated by a regression proposed by Barbier et al. [25]: $M_s = 545 - 9.2Cr - 17.3Ni - 15.4Mo - 1.4Al - 2.44Ti$. With the addition of Mo (alloy 6) the fraction of retained austenite increased compared to alloy 4 and 5, which is in agreement with the decrease of the martensite start temperature. In the aged condition alloys 1 to 3 showed a negligible austenite fraction. Adding Cr (alloys 4 and 5) and Mo (alloy 6) led to an increased austenite fraction, with Mo having a significantly stronger effect on the formation of reverted austenite than Cr. Sha et al. [26] reported that the addition of Cr had a stronger effect on increasing the volume fraction of reverted austenite than increasing the aging temperature by 10 °C. The reversion of austenite is a complex process that is influenced by the nucleation of austenite at local Ni enriched zones [23,27] while simultaneously competing with the precipitation of Ni-rich intermetallic phases, which means that the effect of the chemical composition of the alloy is hard to separate from the effect of the evolution of the precipitates and the matrix composition.

For alloy 5 the mean length of the η -Ni₃Ti phase and the mean diameter of the β -NiAl phase were determined using TEM and APT (see Figs. 5 and 6 for comparison). The results showed that both values were estimated lower from the TEM micrographs than they were measured using APT. The β precipitates are very challenging to contrast using TEM, and the difference to APT (5.1 nm from TEM and 6.7 nm from APT) can be explained by an error in the evaluation of the images. The size difference of the η phase (22.2 nm from TEM and 35.3 nm from APT) is expected, since TEM can only show a 2D projection of the particles and an optimal orientation for the length measurement could not be guaranteed. However, due to the nature of the cluster analysis, which sometimes cannot separate between two precipitates in very close proximity, the true value of the mean length of the η phase is expected to be a bit smaller than measured with APT.

The APT measurements also showed that the microstructure of the aged alloys shifts from a composition with an excess of β -NiAl to a composition with an excess of η -Ni₃Ti (see Fig. 7) with an increasing Ti concentration of the alloys, but also with the addition of Cr and Mo. This can be explained by the different formation mechanisms of the two precipitates. The β phase is a coherent phase formed by homogeneous nucleation [28] from Ni and Al rich clusters [14]. As such, the nucleation and growth kinetics of this phase must be strongly governed by the bulk diffusion of the precipitating elements. The η phase is a semi-coherent phase that preferentially nucleates at dislocations [29,30] followed by growth governed by pipe diffusion [9,29]. Furthermore, a study showed that the β -NiAl phase forms during earlier stages of aging, while the η -Ni₃Ti phase precipitates after a longer aging time [14]. One

explanation for the change from a microstructure with β -NiAl excess to a microstructure with η -Ni₃Ti excess with the addition of Cr and Mo is that Cr and Mo might have an influence on the diffusion kinetics of the precipitating elements (Ni, Ti, Al). The APT analysis of the η -Ni₃Ti phase showed that the Cr- and Mo-alloyed materials had a higher concentration of Al in the η -Ni₃Ti precipitate phase (see Fig. 9a), which suggests that more Al was re-distributed via pipe diffusion when Cr and Mo were present. A Fe and Mo rich phase was also observed in alloy 6 in the aged condition (Figs. 6d and 9b). Earlier work from Sha et al. [26] reported that Mo prefers to segregate to the η -Ni₃Ti particles and to subsequently form Fe₇Mo₆ particles, a typical phase for Mo-containing maraging steels. The segregation of Mo to the η -Ni₃Ti-matrix interface was later confirmed by Thuvander et al. [6] for a maraging steel with different composition. Last, it should be noted that the influence of the (Fe,Cr)₇(Mo,Cr)₆ phase in alloy 6 was not considered in the present study due to the much lower volume fraction than the counterparts.

5. Conclusion

Six different maraging model alloys based on the Fe-12Ni system were defined by the step-wise addition of alloying elements to study the influence of Ti and Al variations and the influence of Cr and Mo on the strength, toughness and the formation of precipitates. After testing the six different maraging alloys the following conclusions about the influence of the alloy composition on the evolution of the microstructure and the mechanical properties can be drawn:

- Per volume fraction the η -Ni₃Ti has a higher strengthening effect than the β -NiAl phase. However, the combination of both precipitate phases leads to a vastly improved precipitation hardening effect, compared to having only a single precipitate phase.
- The volume fractions of η -Ni₃Ti and β -NiAl precipitates can be directly influenced by the concentration of Ti and Al. A higher Al concentration leads to an excess of β -NiAl, while a higher Ti concentration leads to an excess of η -Ni₃Ti.
- The elements Cr and Mo, which are alloyed for improved corrosion resistance, promote the formation of the η -Ni₃Ti phase as opposed to the β -NiAl phase.
- Cr and Mo promote the formation of reverted austenite and thus improve impact toughness and ductility. Specifically the addition of Cr was crucial for improving both strength and ductility simultaneously.
- The Fe-12Ni-10Cr-1.5Ti-1Al alloy is a corrosion resistant maraging steel which is able to reach a tensile strength of 1948 MPa with an impact toughness of 4.9 J.

With further research on optimized process and aging parameters improving the toughness while breaking the 2000 MPa barrier seems plausible.

CRedit authorship contribution statement

S. Zeisl: Conceptualization, Methodology, Formal Analysis, Writing – original draft. **A. Landefeld:** TEM analysis, Writing – review & editing. **N. Van Steenberge:** Tensile Testing, Writing – review & editing. **Y. Chang:** EBSD analysis, Writing – review & editing. **R. Schnitzer:** Writing – review & editing, Supervision.

Declaration of competing interest

The authors declare the following financial interests/personal relationships which may be considered as potential competing interests: The European Research Fund for Coal and Steel (RFCS 847165): funding for S. Zeisl, Y. Chang and N. van Steenberge and for the material.

Data availability

Data will be made available on request.

Acknowledgments

The authors want to thank the European Research Fund for Coal and Steel (RFCS 847165) for providing the funding that made this study possible. Further thanks goes to the “iNiTiAl” consortium for providing the material.

References

- [1] W. Sha, Z. Guo, *Maraging Steels: Modelling of microstructure, properties and applications*, first ed., Woodhead Publishing Ltd., Cambridge, UK, 2009.
- [2] R.F. Decker, C.J. Novak, T.W. Landig, Developments and projected trends in maraging steels, *Jom* 19 (11) (1967) 60–66.
- [3] R. Schnitzer, R. Radis, M. Nöhler, M. Schober, R. Hochfellner, S. Zinner, E. Povoden-Karadeniz, E. Kozeschnik, H. Leitner, Reverted austenite in PH 13-8 Mo maraging steels, *Mater. Chem. Phys.* 122 (1) (2010) 138–145.
- [4] H. Zhang, X. Ji, D. Ma, M. Tong, T. Wang, B. Xu, M. Sun, D. Li, Effect of aging temperature on the austenite reversion and mechanical properties of a Fe-10Cr-10Ni cryogenic maraging steel, *J. Mater. Res. Technol.* 11 (2021) 98–111.
- [5] W. Sha, G.D. Smith, A. Cerezo, Atom probe field-ion microscopy study of ageing behaviour of a model FeNiCoMo maraging steel, *Surf. Sci.* 266 (1–3) (1992) 378–384.
- [6] M. Thuvander, M. Andersson, K. Stiller, Precipitation process of martensitic PH stainless steel Nanoflex, *Mater. Sci. Technol.* 28 (6) (2012) 695–701.
- [7] H. Leitner, R. Schnitzer, M. Schober, S. Zinner, Precipitate modification in PH13-8 Mo type maraging steel, *Acta Mater.* 59 (12) (2011) 5012–5022.
- [8] S. Zhirafar, A. Rezaeian, M. Pugh, Effect of cryogenic treatment on the mechanical properties of 4340 steel, *J. Mater. Process. Technol.* 186 (1–3) (2007) 298–303.
- [9] H. Leitner, M. Schober, R. Schnitzer, Splitting phenomenon in the precipitation evolution in an Fe-Ni-Al-Ti-Cr stainless steel, *Acta Mater.* 58 (4) (2010) 1261–1269.
- [10] R. Schnitzer, M. Schober, S. Zinner, H. Leitner, Effect of Cu on the evolution of precipitation in an Fe-Cr-Ni-Al-Ti maraging steel, *Acta Mater.* 58 (10) (2010) 3733–3741.
- [11] C.K. Yao, Z. Xu, Influence of hot-deformation on morphology and effective grain size of lath martensite in 18Ni maraging steel, *Mater. Chem. Phys.* 14 (6) (1986) 559–568.
- [12] E.I. Galindo-Nava, W.M. Rainforth, P.E. Rivera-Díaz-del Castillo, Predicting microstructure and strength of maraging steels: Elemental optimisation, *Acta Mater.* 117 (2016) 270–285.
- [13] B. Gault, M. Moody, J.M. Cairney, S.P. Ringer, *Atom Probe Microscopy*, in: Springer Series in Materials Science, Springer, New York, 2012.
- [14] S. Zeisl, A. Lassnig, A. Hohenwarter, F. Mendez-Martin, Precipitation behaviour of a Co-free Fe-Ni-Cr-Mo-Ti-Al maraging steel after severe plastic deformation, *Mater. Sci. Eng. A* 833 (November 2021) (2021) 142416.
- [15] L.T. Stephenson, M.P. Moody, P.V. Liddicoat, S.P. Ringer, New techniques for the analysis of fine-scaled clustering phenomena within atom probe tomography (APT) data, *Microsc. Microanal.* 13 (6) (2007) 448–463.
- [16] S. Zeisl, R. Schnitzer, Cooling Rate Controlled Aging of a Co-Free Fe-Ni-Cr-Mo-Ti-Al Maraging Steel, *Metals* 12 (4) (2022).
- [17] R. Schnitzer, S. Zinner, H. Leitner, Modeling of the yield strength of a stainless maraging steel, *Scr. Mater.* 62 (5) (2010) 286–289.
- [18] E.I. Galindo-Nava, W.M. Rainforth, P.E. Rivera-Díaz-del Castillo, Predicting microstructure and strength of maraging steels: Elemental optimisation, *Acta Mater.* 117 (2016) 270–285.
- [19] H. Nakagawa, H. Yokota, T. Miyazaki, Effects of aging temperature on the microstructures and mechanical properties of a precipitation hardening martensitic stainless steel containing retained austenite, *J. Mater. Sci.* 35 (5) (2000) 2245–2253.
- [20] R. Schnitzer, G.A. Zickler, E. Lach, H. Clemens, S. Zinner, T. Lippmann, H. Leitner, Influence of reverted austenite on static and dynamic mechanical properties of a PH 13-8 Mo maraging steel, *Mater. Sci. Eng. A* 527 (7–8) (2010) 2065–2070.
- [21] C.-y. Huang, H.-w. Yen, HRTEM investigations on nano precipitates in custom 475 maraging stainless steel, *Mater. Charact.* 178 (March) (2021) 111216.
- [22] M.C. Niu, K. Yang, J.H. Luan, W. Wang, Z.B. Jiao, Cu-assisted austenite reversion and enhanced TRIP effect in maraging stainless steels, *J. Mater. Sci. Technol.* 104 (2022) 52–58.
- [23] H. Zhang, M. Sun, D. Ma, B. Xu, T. Wang, D. Li, Y. Li, Effect of aging temperature on the heterogeneous microstructure and mechanical properties of a 12Cr-10Ni-Mo-Ti maraging steel for cryogenic applications, *J. Mater. Sci.* 56 (19) (2021) 11469–11484.

S. Zeisl et al.

Materials Science & Engineering A 861 (2022) 144313

- [24] W. Wu, L.Y. Hwu, D.Y. Lin, J.L. Lee, Relationship between alloying elements and retained austenite in martensitic stainless steel welds, *Scr. Mater.* 42 (11) (2000) 1071–1076.
- [25] D. Barbier, Extension of the martensite transformation temperature relation to larger alloying elements and contents, *Adv. Energy Mater.* 16 (1) (2014) 122–127.
- [26] W. Sha, A. Cerezo, G.D.W. Smith, Phase Chemistry and Precipitation Reactions in Maraging Steels: Part IV. Discussion and Conclusions, *Metall. Trans. A* 24 (June) (1993).
- [27] Y. Li, D.S. Martín, J. Wang, C. Wang, W. Xu, A review of the thermal stability of metastable austenite in steels: Martensite formation, *J. Mater. Sci. Technol.* 91 (2021) 200–214.
- [28] S. Jiang, H. Wang, Y. Wu, X. Liu, H. Chen, M. Yao, B. Gault, D. Ponge, D. Raabe, A. Hirata, M. Chen, Y. Wang, Z. Lu, Ultrastrong steel via minimal lattice misfit and high-density nanoprecipitation, *Nature* 544 (7651) (2017) 460–464.
- [29] S.J. Kim, C.M. Wayman, Precipitation behavior and microstructural changes in maraging FeNiMnTi alloys, *Mater. Sci. Eng. A* 128 (2) (1990) 217–230.
- [30] C. Zhang, C. Wang, S.L. Zhang, Y.L. Ding, Q.L. Ge, J. Su, Effect of aging temperature on the precipitation behavior and mechanical properties of Fe–Cr–Ni maraging stainless steel, *Mater. Sci. Eng. A* 806 (January) (2021) 140763.

Publication IV

Strengthening effect of NiAl and Ni₃Ti precipitates in Co-free maraging steels

S. Zeisl, N. Van Steenberge, and R. Schnitzer

Manuscript under review for *Journal of Materials Science* (2023)

Strengthening effect of NiAl and Ni₃Ti precipitates in Co-free maraging steels

Stefan Zeisl^{1*}, Nele Van Steenberge^{2†} and Ronald Schnitzer^{1†}

^{1*}Department of Materials Science, Montanuniversität Leoben, Franz-Josef Straße 18, Leoben, 8700, Austria.

²OnderzoeksCentrum voor de Aanwending van Staal, Technologiepark Techlane A4C, Zwijnaarde, 9052, Belgium.

*Corresponding author(s). E-mail(s): stefan.zeisl@unileoben.ac.at;

Contributing authors: nelevansteenberge@gmail.com;
ronald.schnitzer@unileoben.ac.at;

†These authors contributed equally to this work.

Abstract

One class of maraging steels are strengthened by a combination of β -NiAl and η -Ni₃Ti intermetallic phases which are precipitated during an aging heat treatment. To establish a meaningful structure-property relationship the precipitation strengthening effect from each phase must be isolated from the other strengthening mechanisms. To achieve this, a series of model alloys based on the Fe-12Ni alloy system were aged and characterized to determine the precipitation strengthening effect. In the course of this study, using a new approach, atom probe tomography was used to determine the spacing between precipitates and to calculate the individual strength contribution of the β and the η phase using a model describing the precipitate-dislocation interactions. It was found that the precipitation strengthening of the combined β and η phases is close to 1000 MPa and that the relative strengthening effect of each phase is sensitive to the Ti and Al concentration.

2 *Strengthening effect of NiAl and Ni₃Ti precipitates in Co-free maraging steels*

Keywords: APT, precipitation hardening, inter-precipitate distance, strength model

1 Introduction

Maraging steels belong to the group of precipitation hardening high-strength steels and provide an excellent combination of strength and toughness. Because of their well-balanced properties they are often used in military, aerospace and sport applications [1]. The microstructure of maraging steels consists of a soft Ni martensite matrix with nano-sized precipitates that are crucial for the strength of the material [2]. Depending on the chemical composition and the applied heat treatments maraging steels oftentimes also contain residual or reverted austenite.

The type of possible precipitate phases is governed by the chemical composition of the alloy. Generally, it can be distinguished between two classes of maraging steels: Co-alloyed and Co-free maraging steels [1]. Co is an alloying element that lowers the nucleation barrier for certain types of intermetallic phases, e.g. the Fe₂Mo phase, which is a characteristic phase for Co-alloyed maraging steels [3]. The Co-free variants developed out of necessity in the 1970s as a result of rising Co prices. These types of maraging steels are predominantly hardened by the β -NiAl or the γ -Ni₃Ti phase. However other types of phases such as the G or R phases have been identified as well [4].

The conventional heat treatment route for maraging steels consist of a solution annealing heat treatment in the austenite region, typically around 850-950°C. This is followed by quenching, resulting in a martensite microstructure. Depending on the chemical composition, the martensite finish temperature can

Strengthening effect of NiAl and Ni₃Ti precipitates in Co-free maraging steels 3

be lower than the quenching temperature. In this case a subsequent cryogenic treatment can be performed to decrease the fraction of residual austenite. As a last step the solution annealed maraging steel is aged at temperatures between 400-600°C which causes strengthening by the precipitation of intermetallic phases.

The value of precipitation strengthening is useful in order to draw meaningful conclusions about the process-structure-property relationships of a precipitation hardened material. To determine this contribution a variety of empirical relations based on the radius and the volume fraction of precipitates exist, e.g. [5–7]. However, the strengthening effect of precipitates is ultimately determined by the interaction between the dislocations and precipitates, for which the inter-precipitate spacing and the mean particle radius are the defining quantities [8]. Independent of the strengthening models the precipitation strengthening can also be determined as the remainder to the total yield strength if all other strength contributions are known [9].

In the current literature the determination of the precipitate spacing for very small distances (where electron microscopy reaches its limits) is not well established yet. Furthermore, many empirical models don't provide information about the mechanisms behind precipitation strengthening which is useful in order to determine why a certain particle exhibits a certain strengthening effect. Atom probe tomography (APT) is a measurement method which allows for atomic resolution [10] investigations of the elemental distribution at nano-scale of a material. This method can be used to reconstruct the three-dimensional distribution of precipitates and to determine the spacing between them.

Although the measurement of distances with APT is considered risky because the quality of the data is dependent on the reconstruction parameters

4 *Strengthening effect of NiAl and Ni₃Ti precipitates in Co-free maraging steels*

this risk can be limited if the reconstruction is calibrated using complementary microscopy. Furthermore, if the morphology of the precipitates is known beforehand the parameters can be adjusted to guarantee a correct reconstruction.

This study seeks to propose an approach to experimentally quantify the precipitation strengthening effect of materials with more than one precipitate phase. In essence, data from atom probe tomography will be used to calculate the surface-to-surface distance between spherical and rod-like precipitates. The validity of this approach will be verified by comparing it to the precipitation strengthening that is obtained as a remainder to the total yield strength by calculating all other contributions to the yield strength which are calculated using a model by Galindo-Nava et al. [5, 11].

2 Materials and Methods

Alloys with five different chemical compositions were produced by the *OnderzoeksCentrum voor de Aanwending van Staal* (Zwijnaarde, Belgium) via vacuum induction melting and cast into ingots with a mass of 100 kg. The ingots were hot-rolled (1250°C) into sheets with a thickness of 8 mm. The chemical composition of the alloys was measured with X-ray fluorescence and is shown in Table 1. The sheets were solution annealed at 850°C for a duration of 90 min. Alloys #4 and #5 were subject to a cryogenic treatment at -80°C for 16 h. All alloys were aged at 510°C for 16 h.

Tensile tests were performed to obtain the 0.2% offset yield strength ($R_{p0.2}$) using an Instron 5500 universal testing machine with one test per condition.

Strengthening effect of NiAl and Ni₃Ti precipitates in Co-free maraging steels 5

The tensile test specimens were manufactured from sheet material, had a circular cross-section with a diameter of 3.8 mm and a gauge length of 25 mm in transverse direction.

Table 1: Concentration of the alloying elements (in wt.%) of each alloy used in this study. The chemical composition of all alloys is balanced with Fe.

Alloy Number	wt.%			
	Ni	Cr	Al	Ti
#1 - 1Ti	11.8			0.9
#2 - 1.5Al	11.5		1.4	
#3 - 1.5Al,1Ti	11.6		1.7	0.9
#4 - 10Cr,1.5Al,1Ti	11.9	9.9	1.6	1
#5 - 10Cr,1Al,1.5Ti	11.9	10	0.9	1.5

The microstructure was characterized from micro- to nano-scale using electron backscatter diffraction (EBSD), X-ray diffraction (XRD) and APT. EBSD was used to measure the martensite block size, which can be treated as the effective grain-size of maraging steels [5, 12]. EBSD was performed using a Versa3D DualBeam workstation and the data were analyzed using the OIM Analysis software, and the martensite blocks were defined using an orientation mismatch of 10.5°.

XRD was used to determine the austenite fraction, the lattice parameter of the martensite and the dislocation density of the martensite. The XRD measurements were performed with a Bruker Advanced D8 DaVinci instrument with Cu-K_α radiation. The results were evaluated using LaB₆-calibrated Rietveld refinement, and the dislocation density ρ was estimated from the h-k-l independent micro-strain ϵ using the Williamson-Smallman approach [13, 14]: $\rho = (\rho_D \rho_S)^{1/2}$ with ρ_D being the dislocation density due to the domain size and ρ_S being the dislocation density corresponding to the micro-strain ϵ . ρ_D was

6 *Strengthening effect of NiAl and Ni₃Ti precipitates in Co-free maraging steels*

calculated from $\rho_D = 3/D^2$ with D being the domain size, for which the mean martensite block size was used. ρ_S was calculated from $\rho_S = k \langle \epsilon^2 \rangle / b^2$ with $k=14.4$ [15] being a material constant and $b=0.249$ nm being the Burgers vector.

The metallographic samples that were used for EBSD and XRD were prepared using standard polishing methods. The EBSD samples were finished by electropolishing using a Struers A2 electrolyte.

APT was used to characterize the size of the precipitates, the mean free distance and surface-to-surface distance between precipitates and the chemical composition of the matrix phase and precipitates. The measurements were performed in a LEAP 3000X HR microscope with the laser-assisted mode. For the laser-assisted mode a pulse frequency of 250 kHz, a laser energy of 0.3 nJ and a specimen temperature of 60 K were used. The preparation of the APT specimens was performed with a standard 2-step electropolishing method [16]. The first polishing step was performed using a solution of 25 vol% of perchloric acid in glacial acetic acid and the final step was performed with a 2% solution of perchloric acid in 2-butoxyethanol. The IVAS software suite (version 3.6.14) was used to analyze the atom probe results. For the statistical evaluation of the precipitates a cluster search based on the DBSCAN algorithm was used. The parameters d_{Max} and N_{Min} for the DBSCAN algorithm are presented in Table 2. d_{Max} is the maximum pair distance between adjacent atoms and N_{Min} is the minimal cluster size. The erosion and envelope distance were chosen to be equal to d_{Max} , which was determined using a procedure described by Stephenson et al. [17].

Table 2: DBSCAN algorithm parameters, for each alloy and type of precipitate, that were used for cluster detection.

Alloy	Center	Ni ₃ Ti		Center	NiAl	
		d_{Max} (nm)	N_{Min}		d_{Max} (nm)	N_{Min}
#1	Ti	1.0	100			
#2				Al	0.75	90
#3	Ti	1.05	1000	Al	0.87	50
#4	Ti	1.15	1000	Al	0.82	150
#5	Ti	1.05	1200	Al	0.82	150

2.1 Determination of the precipitate spacing

The mean surface-to-surface distance between the precipitates L_S was determined with two different approaches. For the spherical β -NiAl phase L_S was determined by using a 3-d tree analysis [18] as implemented in the Python package SciPy [19]. The 3-d tree analysis was generated using the center points of the clusters, which were obtained from the cluster analysis, and was used to determine the distance to the first, second and third nearest neighboring cluster for each cluster. The radius R_1 and R_2 of each neighboring cluster pair was subtracted from the center-to-center distance to obtain the surface-to-surface distance. L_S was defined as the mean surface-to-surface distance of all cluster pairs. Fig. 1 demonstrates the connections between neighboring clusters and shows the distance between their centers for the NiAl phase in alloy #5, exemplary.

The surface-to-surface distance L_S of the η -Ni₃Ti phase was calculated by a line-interception method that was implemented in Python. The positions of the clustered atoms were grouped into circular slices with a thickness of Δz along the z-direction of the APT reconstruction as shown in Fig. 2a. L_S was calculated as the mean value of the mean free distance of each z-slice, which is shown in Fig. 2b. For all evaluations in this study a thickness of $\Delta z=2$ nm

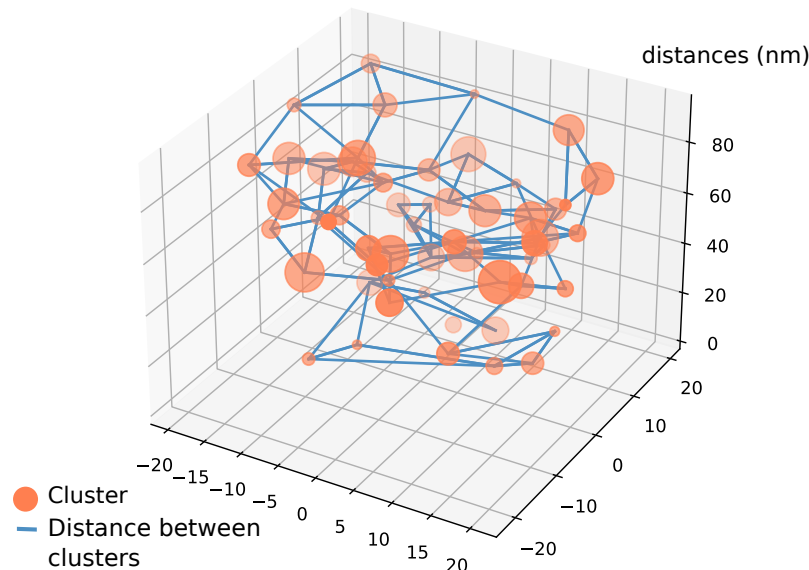
8 *Strengthening effect of NiAl and Ni₃Ti precipitates in Co-free maraging steels*

Figure 1: First-, second- and third-nearest neighbor pairs for a set of NiAl clusters from alloy #5.

was used. To ensure a reliable mean value, this evaluation was performed for 5 different rotation angles around the z-axis of the reconstruction.

To calculate the mean radius \bar{r} the Ni₃Ti clusters were transformed into a cylinder with a radius of r_C with equal volume and length of the original precipitates. \bar{r} was calculated according to [8]: $\bar{r} = \sqrt{2/3}r_C$.

The mean free distance λ between the precipitates was calculated using the previously described line-interception method. For alloys #3 to #5 a combined data-set of both precipitate types was used to determine λ for each alloy.

2.2 Determination of the precipitation strengthening

The value of the strength increase due to precipitation strengthening (σ_{PH}) was calculated by two different models. The first model relied on a work by Galindo-Nava et al. [5, 11] and used the experimental results of EBSD, XRD and APT to calculate the contribution of the grain-size, solid-solution strengthening, dislocation density and the austenite fraction to the yield strength. σ_{PH}

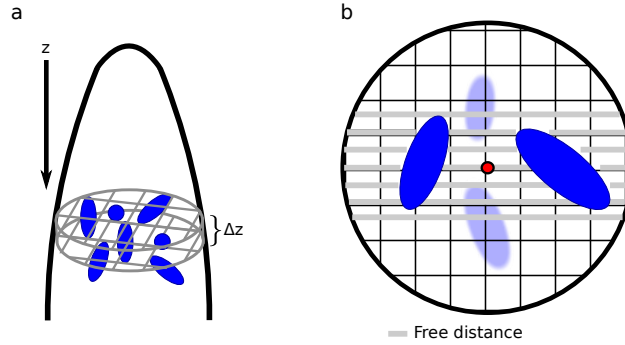


Figure 2: a) Demonstration of the partitioning of the APT reconstruction into z-layers with thickness Δz . b) Demonstration of the measurement of the mean free distance between precipitates of a z-layer.

was determined as the remainder between the yield strength and the sum of the aforementioned strength contributions. This model was used to verify the validity of the second model.

The strength resulting from grain size strengthening (σ_{GS} , Equation 1 [11]) was determined with a Hall-Petch model and the contribution of the dislocation density (σ_{ρ} , Equation 2 [11]) is given by the Taylor equation. The solid solution strengthening (σ_{SS}) was determined by using the Fleischer model (Equation 3 [11]).

$$\sigma_{GS} = \frac{300}{\sqrt{d_{\text{Block}}}} \quad (1)$$

$$\sigma_{\rho} = 0.25M\mu b\sqrt{\rho} \quad (2)$$

$$\sigma_{SS} = \sum_i (\beta_i^2 x_i)^{1/2} \quad (3)$$

$300 \text{ MPa}\mu\text{m}^{1/2}$ is the Hall-Petch constant for maraging steels [11], d_{Block} is the average martensite block size, b is the magnitude of the Burgers vector in α -Fe (0.249 nm), μ is the shear modulus of α -Fe (80.4 GPa [20]), ρ is the dislocation density and β_i and x_i correspond to the solid solution factor and the concentration (in at.%) of each alloying element, respectively. The solid solution factor β_i was determined using Equation 4 according to Fleischer's

10 *Strengthening effect of NiAl and Ni₃Ti precipitates in Co-free maraging steels*
formula [11].

$$\beta_i = \kappa\mu(\eta'_i + 16\delta_i)^{3/2} \quad (4)$$

κ is a factor with the value $\kappa = 0.0045$ [11]. $\eta'_i = \eta_i/(1 + 0.5\eta_i)$ was calculated from the modulus mismatch with respect to pure iron $\eta_i = |\mu_i - \mu_{Fe}|/\mu_{Fe}$. $\delta_i = |r_i - r_{Fe}|/r_{Fe}$ corresponds to the lattice mismatch with respect to pure iron. The shear modulus μ_i and the metallic radius r_i were obtained from [20].

The influence of reverted austenite on the yield strength was calculated using a linear mixture rule [21, 22]. Schnitzer et al. [22] determined the yield strength of pure austenite in maraging steels as $\sigma_\gamma = 217$ MPa. If $F_{\alpha'}$ and F_γ are the volume fractions of martensite and austenite, respectively, then the yield strength can be expressed as: $\sigma_Y = F_{\alpha'}\sigma_{\alpha'} + F_\gamma\sigma_\gamma$. The strength of the martensite with precipitates ($\sigma_{\alpha'}$) of the aged samples can be expressed as [5]:

$$\sigma_{\alpha'} = \sigma_0 + \sigma_{GS} + \sigma_\rho + \sigma_{SS} + \sigma_{PH} \quad (5)$$

With $\sigma_0 = 50$ MPa being the strength contribution due to lattice friction [11].

The second model is based on work from Ahmadi et al. [8] and describes the precipitation hardening effect of multi-particle systems. This model considers the strong and weak shearing mechanisms for screw and edge dislocations and the non-shearing Orowan mechanism. For this study, dealing with maraging steels with a body-centered cubic martensite matrix, only screw dislocations were considered. Furthermore, the shearing mechanisms were only considered for the coherent β -NiAl phase. For the semi-coherent η -Ni₃Ti phase only the Orowan mechanism was considered [23].

The following part presents the equations for the critical resolved shear stress (τ) stemming from the different strengthening mechanisms for screw

Strengthening effect of NiAl and Ni₃Ti precipitates in Co-free maraging steels 11

dislocations for shearable particles as presented by Ahmadi et al. [8]. The strengthening due to shearable particles is the sum of multiple effects: the coherency, modulus, anti-phase boundary, stacking fault and interfacial effect [8]. According to this model each effect contributes to the strength via a superposition expression: $\tau_1^q = \tau_{Coh}^q + \tau_{Mod}^q + \tau_{APB}^q + \tau_{SF}^q + \tau_{IF}^q$ with $q = 1.8$. The combined strength increase of multiple particles is also added up via the same type of expression: $\tau_{PH}^q = \tau_1^q + \tau_2^q + \dots + \tau_n^q$. The literature offers multiple options for the selections of q for τ_{PH} [8, 24]. For the present material a value of $q=1.2$, which is the same for all alloys, was used since this value presented the best fit to the results of model 1.

The original model provided equations for both strong and weak shearable particles. However, preliminary evaluations showed that for the present alloys (aged at 510°C for 16 h) only the strong mechanisms were relevant. For further details on the model and the derivation of the equations the reader is advised to refer to [8].

A central value for the evaluation of the strengthening effects is the dislocation line tension $T(\Theta)$, which can be calculated as [8]:

$$T(\Theta) = \frac{Gb^2}{4\pi} \left(\frac{1 + \nu - 3\nu(\sin\Theta)^2}{1 - \nu} \right) \ln\left(\frac{r_o}{r_i}\right) \quad (6)$$

with $G=80.4$ GPa [20] being the shear modulus of the matrix, $\nu=0.29$ [20] the Poisson's ratio of the matrix, Θ the angle between the line element of the dislocation and its Burgers vector ($\Theta=0$ for screw dislocations), r_o the outer cut-off radius, which is the distance between two precipitates along the dislocation line corresponding to the mean free distance λ , and r_i the inner cut-off radius, which is the radius of the dislocation core and is between b and $4b$. r_i was chosen as 0.3 nm [25].

12 *Strengthening effect of NiAl and Ni₃Ti precipitates in Co-free maraging steels*

The strong coherency strengthening effect is calculated by:

$$\tau_{\text{coh,strong}} = 2 \frac{J}{L_s} \left(\frac{T^3 G \bar{r}}{b^3} \right)^{\frac{1}{4}} \quad (7)$$

with the magnitude of the Burgers vector $b=0.249$ nm, \bar{r} the mean radius of the precipitates, ϵ the constrained strain produced by the lattice misfit, L_s the mean free distance between precipitates and J a correction factor.

The strong modulus strengthening effect is calculated by:

$$\tau_{\text{mod,strong}} = J \frac{\omega_1 |G_p - G| b^2 (r_s/b)^{\omega_2}}{b L_s} \quad (8)$$

with $\omega_1=0.0722$ [8] and $\omega_2=0.81$ [8] being constants representing the dislocation core energy inside and outside of the precipitate, respectively, $G_p = 70.2$ GPa [26] the shear modulus of the β -NiAl precipitate phase and r_s the equivalent radius of the precipitate.

The creation of an anti-phase boundary due to the movement of superdislocations creates a contribution to precipitation strengthening which can be described by:

$$\tau_{\text{APB,strong}} = J \left(\frac{2VT}{\pi b L_s} \right) \left(\frac{\pi \gamma_{\text{APB}} r_s}{VT} - 1 \right)^{\frac{1}{2}} \quad (9)$$

with $\gamma_{\text{APB}} = 800$ J/m² (for β -NiAl) and V is a constant that was assumed as 2.8 [8]. The formation of additional interface area between the matrix and the precipitate due to cutting creates a strength contribution that can be described

Strengthening effect of NiAl and Ni₃Ti precipitates in Co-free maraging steels 13

by:

$$\tau_{\text{IF,strong}} = J \frac{2\gamma_{\text{IFE}}b}{bL_s} \quad (10)$$

with $\gamma_{\text{IFE}}=20 \text{ mJm}^{-2}$ [27] being the interface energy between the NiAl precipitates and the matrix phase.

The contribution from the Orowan bypass mechanism can be evaluated from the following equation:

$$\tau_{\text{Orowan}} = \frac{Gb}{2\pi\sqrt{1-\nu}L_s} \ln \frac{2r_s}{r_i} \quad (11)$$

The correction factor J was fitted to minimize the error between model 1 and model 2. Both precipitate types had a different value for J , however between all alloys the value of J was the same for each precipitate type.

To compare the results of this model with the results from model 1 the yield stress (σ_y) is calculated from the critical resolved shear stress (τ) using the Taylor relation: $M = \sigma_y/\tau$ [28], where $M=3$ is the Taylor orientation factor [29].

3 Results

Mechanical characterization was performed in order to obtain the yield strength ($R_{p0.2}$) of the aged alloys so that the contribution of precipitation strengthening (σ_{PH}) could be determined. For this, tensile tests were carried out. Fig. 3a shows the engineering stress-strain curves of all alloys in the aged condition. Fig. 3b shows the yield strength of the alloys and it was observed that it increased with the addition of alloying elements, specifically with the

14 *Strengthening effect of NiAl and Ni₃Ti precipitates in Co-free maraging steels*

combination of Ti and Al (alloy #3) and the addition of Cr (alloys #4 and #5).

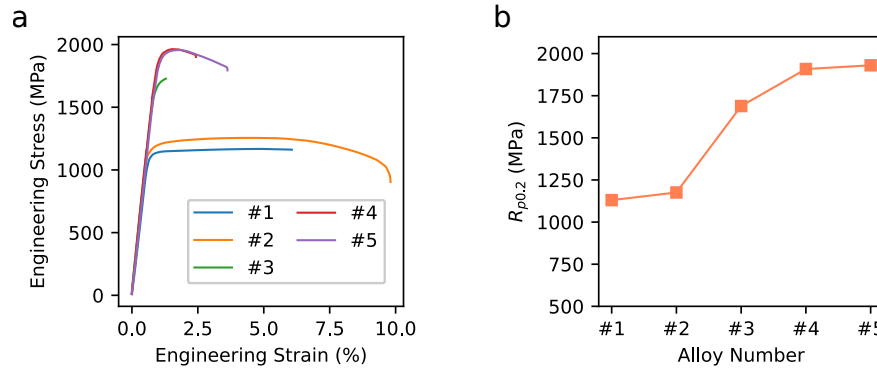


Figure 3: a) Engineering stress-strain curve of all alloys in the aged condition. b) Yield strength ($R_{p0.2}$) of all alloys in the aged condition.

The characterization of the microstructure was performed by EBSD measurements to obtain information about the mean martensite block size and by XRD measurements to obtain the austenite fraction, the lattice parameter of the matrix phase and the dislocation density. Fig. 4 shows the microstructure of all alloys and the mean martensite block size, which was between 16.2 μm and 6 μm . The inverse pole figures also showed that there was a distinct difference of the grain morphology between the Cr-free (alloys #1-#3) and the Cr-alloyed steels (alloys #4 and #5). In essence, the martensite blocks in the Cr-free steels were more globular than in the Cr-alloyed steels, which were more elongated. The results of the XRD measurements are shown in Fig. 5. The austenite fraction was between 0% and 3% for alloy #1 and alloy #5, respectively, the lattice parameter remained relatively constant between 2.872 \AA for alloys #1 and #2 and 2.874 \AA for alloys #3 to #5, and the dislocation density of the materials was between $5.8 \cdot 10^{14} \text{ m}^{-2}$ and $9.6 \cdot 10^{14} \text{ m}^{-2}$.

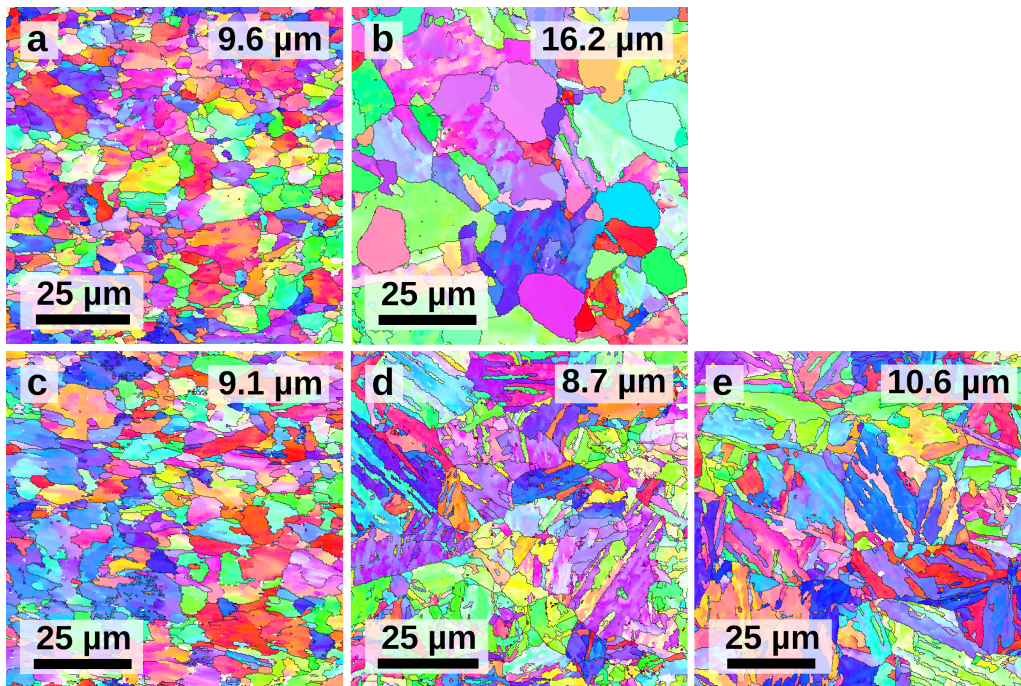


Figure 4: Inverse pole figures obtained from EBSD showing the microstructure and the mean grain size for alloys #1 to #5 (a-e).

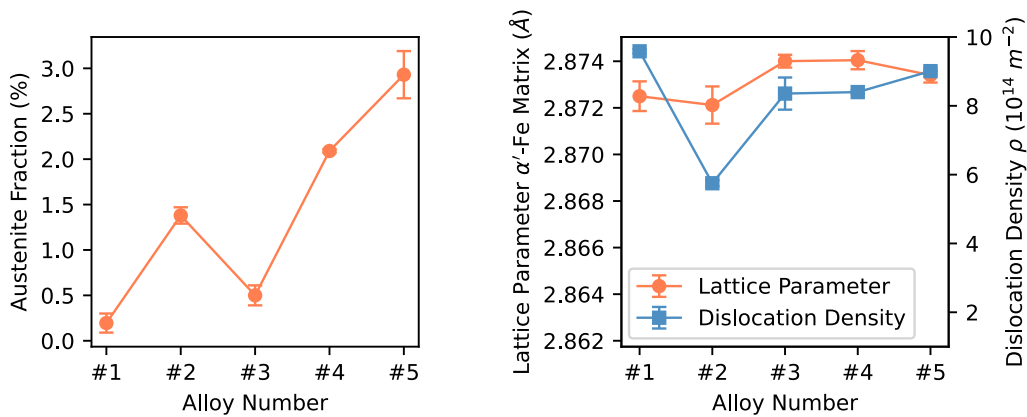


Figure 5: The fraction of austenite and the lattice parameter and dislocation density of the martensite matrix as obtained from evaluation of the XRD data.

The precipitates and the chemical composition of the matrix were characterized on a nano-scale using APT. The precipitate composition varied with the chemical composition. Fig. 6a-e show the iso-concentration surfaces corresponding to the η phase and the β phase, which were rod-like and spherical, respectively,

16 *Strengthening effect of NiAl and Ni₃Ti precipitates in Co-free maraging steels*

for all tested alloys. Alloys #1 and #2 only had one type of precipitate which were the η -Ni₃Ti phase in alloy #1 and the β -NiAl phase in alloy #2. Alloys #3, #4 and #5 all contained both phases. Additionally, the iso-concentration surfaces showed that the volume fraction of the η phase increased from alloy #3 to alloy #5.

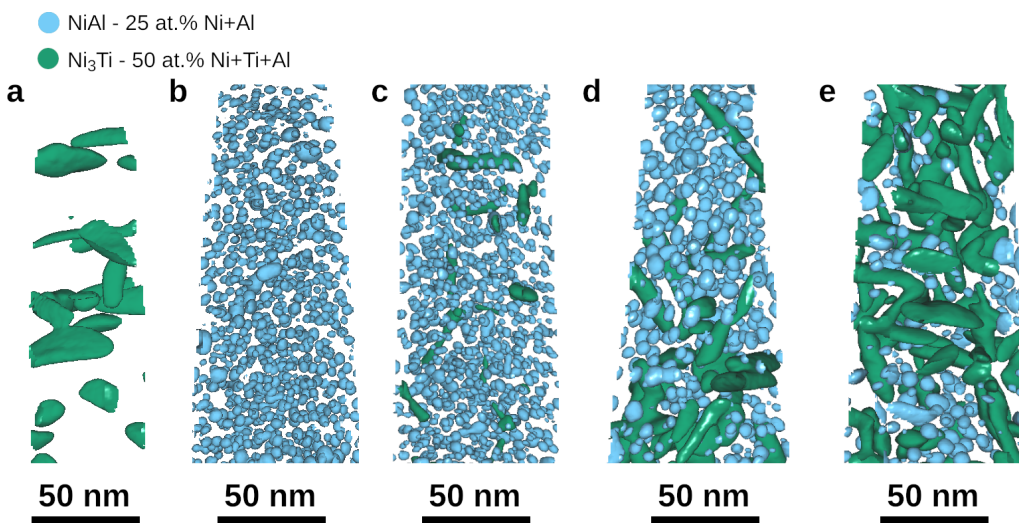


Figure 6: Iso-concentration surfaces corresponding to the Ni₃Ti and the NiAl phase for alloys #1 to #5 (a-e).

The surface-to-surface distance L_s between the precipitates and the mean radius \bar{r} were evaluated using the methods described in section 2.1. Fig. 7a shows that L_s of both intermetallic phases changed with the chemical composition. For Ni₃Ti L_s was the smallest in alloys #1 and #5, and for NiAl L_s was the smallest in alloys #2, #3 and #4. Fig. 7b shows the mean radius \bar{r} of both precipitate types for all alloys. \bar{r} varied between 2.3 nm and 2.8 nm for NiAl and between 3.2 nm and 6.5 nm for Ni₃Ti.

Fig. 8a shows the chemical composition of the martensite matrix phase. The precipitating elements Ni, Ti and Al remained solved in the matrix to different extents, with Ni having the highest and Ti having the lowest matrix

concentrations. The variation of the Ti and Al matrix concentrations was similar between the alloy variations with alloy #3 having the highest solved Ti (0.2 at.%) and Al (1.2 at.%). The Ni concentration decreased steadily from 6.2 at.% to 2.6 at.% for alloy #1 to alloy #5, respectively. Between alloy #4 and #5 the Cr concentration remained at 12.0 at.%. Fig. 8b shows the concentration of Ni, Al and Ti within the β -NiAl precipitates for alloys #2 to #5. In alloys #3 to #5 a similar amount of Ti (about 5 at.%) was present within the NiAl precipitates, and a slight Ni deficit, compared to an ideal ratio of Ni to Al and Ti of 50%, was found within the precipitates. The Ni concentrations were between 40 at.% and 47 at.%.

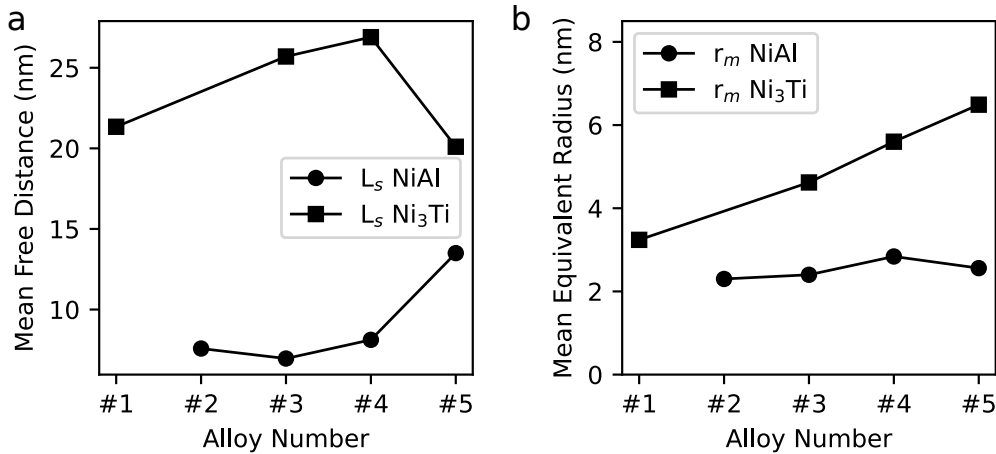


Figure 7: Mean free distance L_s and mean diameter \bar{r} of the η -Ni₃Ti and β -NiAl precipitates for all alloys.

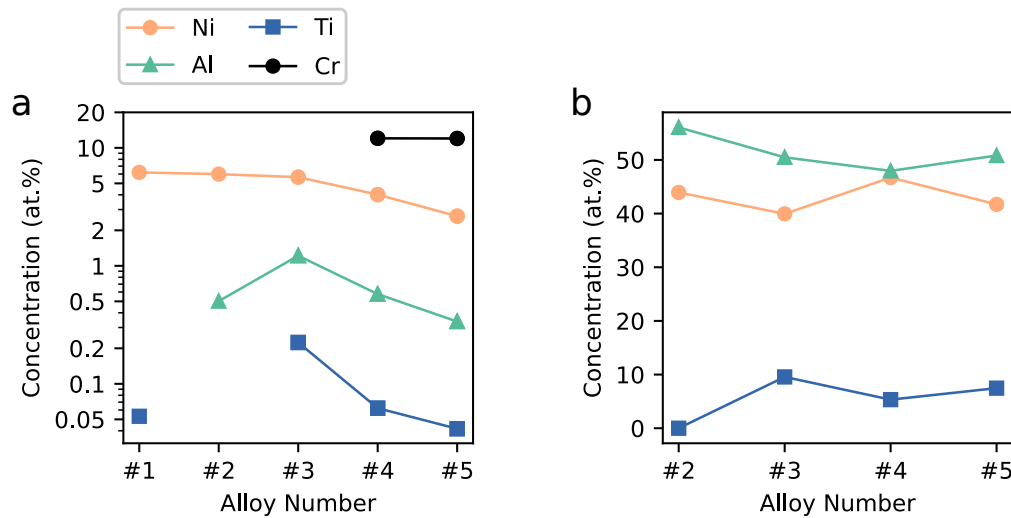
18 *Strengthening effect of NiAl and Ni₃Ti precipitates in Co-free maraging steels*

Figure 8: Chemical composition of a) the martensite matrix phase and b) the β -NiAl precipitate phase for all alloys in the aged condition. For b) the concentration was normalized to the sum of the Ni, Al and Ti concentrations.

4 Strength Modeling

Model 1 and model 2 were implemented and the strength contributions were calculated from the results of mechanical and microstructural characterization. Fig. 9 shows the comparison between the precipitation strengthening obtained from model 1 and model 2, furthermore for model 2 the contribution from each type of precipitate (η -Ni₃Ti and β -NiAl) is also shown. Both models are in good agreement with only small deviations. It was also found that the contribution to the yield strength from the β phase is higher or equal than the contribution from the η phase for alloys #1 to #4. For alloy #5, which was alloyed with Cr and had a higher Ti-concentration than alloy #4, the contribution from the Ni₃Ti phase to the total strength was compared to the NiAl phase.

Fig. 10a shows the contributions to the strength of the martensite with precipitates for model 1. The grain-size strengthening was similar for all alloys with values between 86 MPa and 112 MPa. The solid solution strengthening was highest for alloys #3 and #4 with a value of $\sigma_{SS} = 255$ MPa and 280 MPa,

Strengthening effect of NiAl and Ni₃Ti precipitates in Co-free maraging steels 19

respectively. For alloys #1, #2 and #5 the solid solution strengthening was 99 MPa, 143 MPa and 177 MPa, respectively. The strengthening effect due to dislocations was lowest for alloy #2 (360 MPa) and similar for alloys #2 to #5 with values between 434 MPa and 464 MPa.

Fig. 10b shows the strengthening effect of the different shearing mechanisms for the β -NiAl precipitates. It was calculated that the strengthening effect due to the anti-phase-boundaries (τ_{APB}) is the dominant mechanism for this inter-metallic phase. Coherency strengthening (τ_{Coh}), stemming from the lattice mismatch between matrix and precipitate, played the second largest role. The strengthening effect from the formation of a precipitate-matrix interface (τ_{IF}) and from the mismatch of the elastic modulus (τ_{Mod}) only played a minor role.

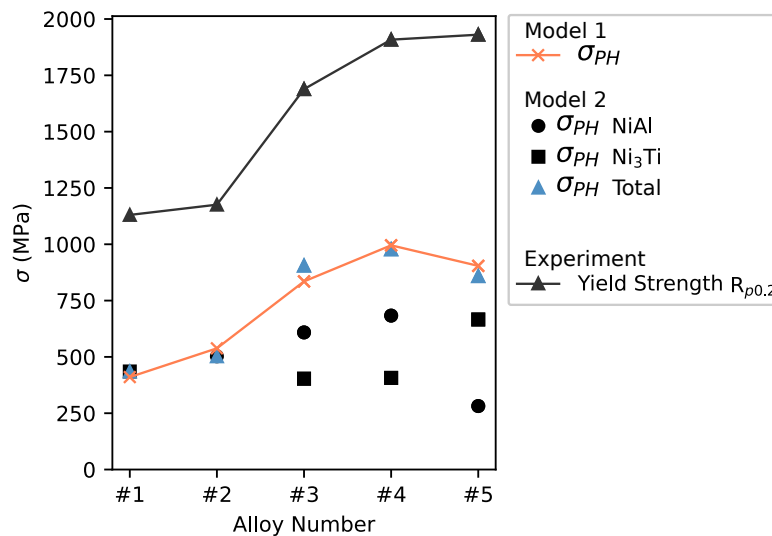


Figure 9: The calculated precipitation strengthening (σ_{PH}) according to model 1 and model 2 for all alloys and the yield strength obtained from the tensile tests.

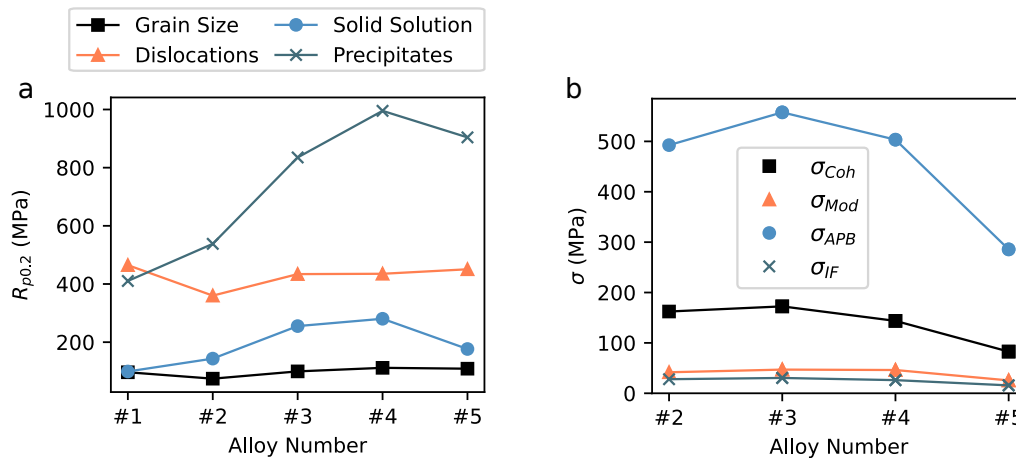
20 *Strengthening effect of NiAl and Ni₃Ti precipitates in Co-free maraging steels*

Figure 10: a) Contributions to the total strength of the martensite with precipitates stemming from grain size strengthening, the effect of the dislocation density, solid solution strengthening and precipitation strengthening. b) Contributions to the precipitation strengthening of the β -NiAl phase from the different shearing mechanisms according to model 2.

5 Discussion

In this study two different approaches on calculating the precipitation strengthening effect using experimental data were analyzed. Model 1 calculated the contribution of grain size, dislocation density and solid solution strengthening to the yield strength (according to [5]) using the results from XRD (austenite fraction and dislocation density), EBSD (block size) and APT (matrix composition). The value of precipitation strengthening (σ_{PH}) was then determined as the remainder to the experimentally measured yield strength (see Equation 5). σ_{PH} obtained from model 1 was used as a comparison and to verify the validity of σ_{PH} obtained from model 2. Model 2 (based on work from Ahmadi et al. [8]) used the mean radius \bar{r} , mean free distance λ and the surface-to-surface distance L_S , which was measured directly from atom probe cluster search data.

Model 1 also compared the strengthening mechanisms that contribute to the total strength (see Fig. 10a) and confirmed that precipitation strengthening plays the largest role for the total strength of the alloys, which is expected and

Strengthening effect of NiAl and Ni₃Ti precipitates in Co-free maraging steels 21

well-known for maraging steels. This is a result of the high number density of precipitates and the small distances between each precipitate. This model also showed that the strengthening effect from dislocations (σ_ρ) plays a major role for the present alloys, especially for alloy #1, for which σ_{PH} and σ_ρ were similar. The alloys had a dislocation density between $5.8 \cdot 10^{14} \text{ m}^{-2}$ and $9.6 \cdot 10^{14} \text{ m}^{-2}$, which is in agreement with the results of other authors [30, 31].

The third-largest strengthening mechanism was solid solution strengthening (σ_{SS}), but the contribution to the total strength was strongly dependent on the alloy. Especially alloys #3 and #4 benefited from an enhanced solid solution strengthening effect (255 MPa and 280 MPa, respectively) while for the other alloys the contribution was between 99 MPa and 176 MPa. The calculation of σ_{SS} showed that Ti is the strongest contributor per at.%, closely followed by Al. Cr added about 40 MPa to the strength in alloys #4 and #5, due to the constant concentration of Cr in the matrix. The effect of Ni on σ_{SS} was negligible (about 5 MPa) compared to the total strengthening effect, which is due to the similar atomic radius and shear modulus of Ni and Fe. The high solid solution factors β (see Equation 3) of Ti and Al stem from the lattice distortion and modulus distortion compared to the matrix, which is high because the lattice parameter and the shear modulus are sufficiently different, and this means that a strong solid solution strengthening effect can be achieved. Despite the slightly higher solid solution factor of Ti a higher contribution to σ_{SS} came from Al because the matrix concentration of Ti ($\lesssim 0.1 \text{ at.}\%$) was significantly lower than the matrix concentration of Al ($\gtrsim 0.7 \text{ at.}\%$). The APT results showed that a higher fraction of Ti was used for the formation of precipitates (see Fig. 8a).

The effect of the grain size (σ_{GS}) or martensite block size was smaller than 112 MPa for all alloys and was the weakest mechanism to contribute to the

22 *Strengthening effect of NiAl and Ni₃Ti precipitates in Co-free maraging steels*

total strength. Generally a smaller block size can be considered to be favorable both in terms of increased strength (see Eq. 1) and increased ductility [32]. However since the size of the hierarchical structures (i.e. blocks, packets and prior austenite grains) in martensite can be influenced by the manufacturing process (e.g. hot-deformation [12, 33]) σ_{GS} might be able surpass σ_{SS} for materials with a different processing route.

Model 2 used direct measurements from APT to determine the mean radius \bar{r} , mean free distance λ and surface-to-surface distance L_S between precipitates to calculate σ_{PH} , which was based on work from Ahmadi et al. [8]. The results of model 2 were compared to σ_{PH} obtained from model 1. In contrast to model 1, model 2 was able to distinguish between the strengthening effect of the β -NiAl phase and η -Ni₃Ti phase and the different shearing mechanisms.

Both models are in good agreement for each alloy, and it could be shown that the alloys switched from being mainly strengthened by the β phase (alloy #3) to being mainly strengthened by the η phase (alloy #5) which is in agreement with the increase of the volume fraction of the η -Ni₃Ti phase from alloy #3 to alloy #5 (see Fig. 6). For the practical use of model 2 and the measurement mechanism presented in this study a calibration for each new material with model 1 and the correct fitting of the correction factor J is suggested.

A detailed look on the strengthening mechanisms of the β -NiAl phase showed that the APB mechanism, followed by the coherency mechanism played the largest role for the strengthening in these alloys (see Fig. 10b). The high contribution from APB strengthening stems from the high APB energy (800 mJ/m²) for the ordered B2-type β -NiAl phase (see Eq. 9).

Regarding the accuracy of the calculations from both models some points need to be addressed. For model 1 the largest uncertainty stems from the

Strengthening effect of NiAl and Ni₃Ti precipitates in Co-free maraging steels 23

experimental error of the three characterization methods (EBSD, XRD and APT), but also from the calculation of σ_{GS} . Galindo-Nava et al. [5] suggested a Hall-Petch factor of $300 \text{ MPam}^{1/2}$ while a study by Rack [34] showed that the Hall-Petch factor for maraging steels can vary with alloy composition and aging heat treatment. In order to improve the accuracy of the results and calibration of model 2 a study to determine the Hall-Petch factor should be performed for any material that makes use of this model.

For model 2 the uncertainty stems from employing direct distance measurements with APT data. This data is sensitive to the reconstruction parameters and also to the selection of cluster analysis parameters, allowing for two opportunities of human error. Firstly, the selection of the reconstruction parameters directly influences the shape of the reconstruction, the size in x-, y- and z-direction and all length measurements performed with this data. This error can be minimized if complementary microscopy is used and the reconstruction parameters are fitted to the shape of the original APT specimen. A second way to ensure a correct reconstruction is to ensure that the reconstruction correctly represents the precipitate morphology, if it is known beforehand. Secondly, the cluster analysis parameters influence the number and the size of the precipitates that are identified. This error can be minimized if a consistent parameter selection strategy is employed. Examples for meaningful strategies can be found in the works of Stephenson et al. [17] and Jäggle et al. [35]. Finally, the accuracy of the calculations could also be improved by determining the exact values of the material constants (e.g. γ_{APB}) that were used for the precipitation strengthening calculation of the β phase using the shearing mechanism. Since the APT results showed that the β phase solves $<5 \text{ at.}\%$ of Ti some deviations of these quantities, compared to pure NiAl, can be expected.

6 Conclusions

Five different maraging steels were characterized by their mechanical properties, their microstructure and dislocation density. Their precipitates were characterized using APT. These experimental data were used to verify if the precipitation strengthening effect of a η -Ni₃Ti and β -NiAl strengthened maraging steel can be calculated by a precipitation strengthening model with the use of direct measurements from APT data. The findings led to the following conclusions:

- The mean free distance and the surface-to-surface distance can be calculated from APT measurements using two different approaches: a nearest-neighbor calculation for spherical particles and an 3D line-interception method for non-spherical particles.
- It was possible to use the mean free distance and the surface-to-surface distance to calculate the precipitation strengthening effect using a precipitation strengthening model and to obtain meaningful results for five maraging steels with different alloy compositions and varying volume fractions of the η -Ni₃Ti and β -NiAl precipitates. The results demonstrated that this approach can be used to establish a meaningful structure-property relationship.
- At the selected aging condition (510°C/16 h) the precipitation strengthening stemming from the β -NiAl phase and the η -Ni₃Ti phase is strongly dependent on the alloy concentration of Al and Ti. For the alloys with a lower Ti and higher Al concentration (1.6 wt.% Al and 1.0 wt.% Ti) the β phase significantly outperforms the η phase while the opposite is true for the alloy with a higher Ti and lower Al concentration (0.9 wt.% Al and 1.5 wt.% Ti)

Strengthening effect of NiAl and Ni₃Ti precipitates in Co-free maraging steels 25

- The combination of both precipitate types significantly improves the strength of the alloys even when the volume fraction of one precipitate phase is low.

Data availability

Access to the experimental data will be given out by the authors upon request.

CRedit author statement

Stefan Zeisl: Conceptualization, Methodology, Formal Analysis, Writing - Original Draft, **Nele Van Steenberge:** Alloy Production, Tensile Testing, Writing - Review & Editing, **Ronald Schnitzer:** Supervision, Writing - Review & Editing.

Acknowledgments

The authors want to thank the European Research Fund for Coal and Steel (RFCS 847165) for providing the funding that made this study possible. Further thanks goes to the “iNiTiAl” consortium for providing the material.

Declaration of competing interests

The authors declare the following financial interests which may be considered as potential conflicting/competing interests: The European Research Fund for Coal and Steel (RFCS 847165) for funding S. Zeisl and N. van Steenberge and for funding the production of the material.

Supplementary information

Not applicable.

26 *Strengthening effect of NiAl and Ni₃Ti precipitates in Co-free maraging steels*

Ethical approval

Not applicable.

References

- [1] Sha W, Guo Z (2009) *Maraging Steels: Modelling of microstructure, properties and applications*, 1st edn. Woodhead Publishing Ltd., Cambridge, UK
- [2] Decker RF, Novak CJ, Landig TW (1967) Developments and projected trends in maraging steels. *Journal of Metals* 19(11):60–66
- [3] Sha W, Smith GD, Cerezo A (1992) Atom probe field-ion microscopy study of ageing behaviour of a model FeNiCoMo maraging steel. *Surface Science* 266(1-3):378–384
- [4] Thuvander M, Andersson M, Stiller K (2012) Precipitation process of martensitic PH stainless steel Nanoflex. *Materials Science and Technology* 28(6):695–701
- [5] Galindo-Nava EI, Rainforth WM, Rivera-Díaz-del Castillo PE (2016) Predicting microstructure and strength of maraging steels: Elemental optimisation. *Acta Materialia* 117:270–285
- [6] Gladman T (1999) Precipitation hardening in metals. *Materials Science and Technology* 15(1):30–36
- [7] Maeng H, Choi Y, Lee SJ (2019) Model of Precipitation Hardening of Al – Mg – Si Alloys Under Aging. *Metal Science and Heat Treatment* 61(7-8):455–460

Strengthening effect of NiAl and Ni₃Ti precipitates in Co-free maraging steels 27

- [8] Ahmadi MR, Povoden-Karadeniz E, Öksüz KI, et al (2014) A model for precipitation strengthening in multi-particle systems. *Computational Materials Science* 91:173–186
- [9] Zeisl S, Schnitzer R (2022) Cooling Rate Controlled Aging of a Co-Free Fe-Ni-Cr-Mo-Ti-Al Maraging Steel. *Metals* 12(4):538
- [10] Miller MK, Forbes RG (2014) *Atom-Probe Tomography: The Local Electrode Atom Probe*, 1st edn. Springer, Boston, MA, USA
- [11] Galindo-Nava EI, Rivera-Díaz-Del-Castillo PE (2015) A model for the microstructure behaviour and strength evolution in lath martensite. *Acta Materialia* 98:81–93
- [12] Yao CK, Xu Z (1986) Influence of hot-deformation on morphology and effective grain size of lath martensite in 18Ni maraging steel. *Materials Chemistry and Physics* 14(6):559–568
- [13] Williamson GK, Hall WH (1953) X-ray line broadening from filed aluminium and wolfram. *Acta Metallurgica* 1(1):22–31
- [14] Murugesan S, Kuppusami P, Mohandas E, et al (2012) X-ray diffraction Rietveld analysis of cold worked austenitic stainless steel. *Materials Letters* 67(1):173–176
- [15] Williamson GK, Smallman RE (1956) III. Dislocation densities in some annealed and cold-worked metals from measurements on the X-ray Debye-Scherrer spectrum. *Philosophical Magazine* 1(1):34–46
- [16] Gault B, Moody M, Cairney JM, et al (2012) *Atom Probe Microscopy*, 1st edn. Springer, New York, NY, USA

- 28 *Strengthening effect of NiAl and Ni₃Ti precipitates in Co-free maraging steels*
- [17] Stephenson LT, Moody MP, Liddicoat PV, et al (2007) New techniques for the analysis of fine-scaled clustering phenomena within Atom Probe Tomography (APT) data. *Microscopy and Microanalysis* 13(6):448–463
- [18] Otair M (2013) Approximate K-Nearest Neighbour Based Spatial Clustering Using K-D Tree. *International Journal of Database Management Systems* 5(1):97–108
- [19] Virtanen P, Gommers R, Oliphant TE, et al (2020) {SciPy} 1.0: Fundamental Algorithms for Scientific Computing in Python. *Nature Methods* 17:261–272
- [20] Warlimont H, Martienssen W (2018) *Springer Handbooks of Materials Data*, 2nd edn. Springer Nature, Cham, Switzerland
- [21] Chen HC, Cheng GH (1989) Effect of martensite strength on the tensile strength of dual phase steels. *Journal of Materials Science* 24(6):1991–1994
- [22] Schnitzer R, Radis R, Nöhner M, et al (2010) Reverted austenite in PH 13-8 Mo maraging steels. *Materials Chemistry and Physics* 122(1):138–145
- [23] He Y, Yang K, Sha W, et al (2004) Microstructure and mechanical properties of a 2000 MPa Co-free maraging steel after aging at 753 K. *Metallurgical and Materials Transactions A: Physical Metallurgy and Materials Science* 35 A(9):2747–2755
- [24] Ardell AJ (1985) Precipitation hardening. *Metallurgical Transactions A* 16(12):2131–2165
- [25] Clouet E, Ventelon L, Willaime F (2011) Dislocation core field. II. Screw dislocation in iron. *Physical Review B - Condensed Matter and Materials*

Strengthening effect of NiAl and Ni₃Ti precipitates in Co-free maraging steels 29

Physics 84(22):224107

- [26] Faraoun H, Aourag H, Esling C, et al (2005) Elastic properties of binary NiAl, NiCr and AlCr and ternary Ni₂AlCr alloys from molecular dynamic and abinitio simulation. *Computational Materials Science* 33(1-3):184–191
- [27] Calderon H, Fine ME (1984) Coarsening kinetics of coherent NiAl-type precipitates in FeNiAl and FeNiAlMo alloys. *Materials Science and Engineering* 63(2):197–208
- [28] Shen JH, Li YL, Wei Q (2013) Statistic derivation of Taylor factors for polycrystalline metals with application to pure magnesium. *Materials Science and Engineering A* 582:270–275
- [29] Galindo-Nava EI, Rivera-Díaz-Del-Castillo PE (2016) Understanding the factors controlling the hardness in martensitic steels. *Scripta Materialia* 110:96–100
- [30] Jacob K, Yadav D, Dixit S, et al (2021) High pressure torsion processing of maraging steel 250: Microstructure and mechanical behaviour evolution. *Materials Science and Engineering A* 802(June 2020):140665
- [31] Zhu J, Lin GT, Zhang ZH, et al (2020) The martensitic crystallography and strengthening mechanisms of ultra-high strength rare earth H13 steel. *Materials Science and Engineering A* 797:140139
- [32] Simm T, Sun L, McAdam S, et al (2017) The Influence of Lath, Block and Prior Austenite Grain (PAG) Size on the Tensile, Creep and Fatigue Properties of Novel Maraging Steel. *Materials* 10(7):730

- 30 *Strengthening effect of NiAl and Ni₃Ti precipitates in Co-free maraging steels*
- [33] Castro Güiza GM, Oliveira CA (2016) Microstructural changes produced by hot forging in a C300 Maraging Steel. *Materials Science and Engineering A* 655:142–151
- [34] Rack HJ (1978) Age hardening-grain size relationships in 18Ni maraging steels. *Materials Science and Engineering* 34(3):263–270
- [35] Jäggle EA, Choi PP, Raabe D (2014) The maximum separation cluster analysis algorithm for atom-probe tomography: Parameter determination and accuracy. *Microscopy and Microanalysis* 20(6):1662–1671

Summary and discussion of the publications

6.1 Aim of the investigations

The studies that were performed as part of this thesis were aimed at obtaining the process-structure-property relationship of an industrial maraging steel with the chemical composition of Fe-12Ni-10Cr-2Mo-1.5Al-1.2Ti (in wt.%) and to improve the strength and ductility of this alloy. The goal was to obtain an alloy-process combination that can guarantee an ultimate tensile strength of 1850 MPa at a fracture elongation of 10% or higher.

The work in this thesis focused on the optimization of the precipitation hardening effect and austenite reversion by varying process parameters (deformation and cooling rate) and by varying the chemical composition (see section 3.1). Furthermore, a method was created to quantify the precipitation-strengthening effect by using measurements from atom probe tomography. This method proved useful to help establish a meaningful structure-property relationship for the maraging steel alloys that were used.

6.2 Influence of processing parameters on the precipitation

All steels that were used in this thesis had chemical compositions based on the Fe-12Ni alloy system with additions of Al, Ti, Cr, and Mo. For these alloys two different intermetallic phases, the β -NiAl phase and the η -Ni₃Ti phase, were of main interest for precipitation hardening.

Publication I and *Publication II* studied an industrial-grade maraging steel (Fe-12Ni-10Cr-2Mo-1.5Al-1.2Ti) which is hardened by both aforementioned intermetallic phases. Further-

more, both studies used a range of different aging times from 0 h to 16 h while the aging temperature was held constant within each study. It was found that for both aging temperatures that were used (500°C and 510°C) the precipitation hardening of this steel starts with the formation of Ni- and Al-rich clusters followed by the formation of β -NiAl precipitates which was followed by the formation of η -Ni₃Ti precipitates. Fig. 6.1 shows the precipitate evolution of this steel at an aging temperature of 500°C. It was observed that 5 min aging was sufficient to produce a clustering of Ni and Al, 60 min of aging was sufficient for the formation of small β precipitates, and 16 h of aging produced fully-developed β and η precipitates.

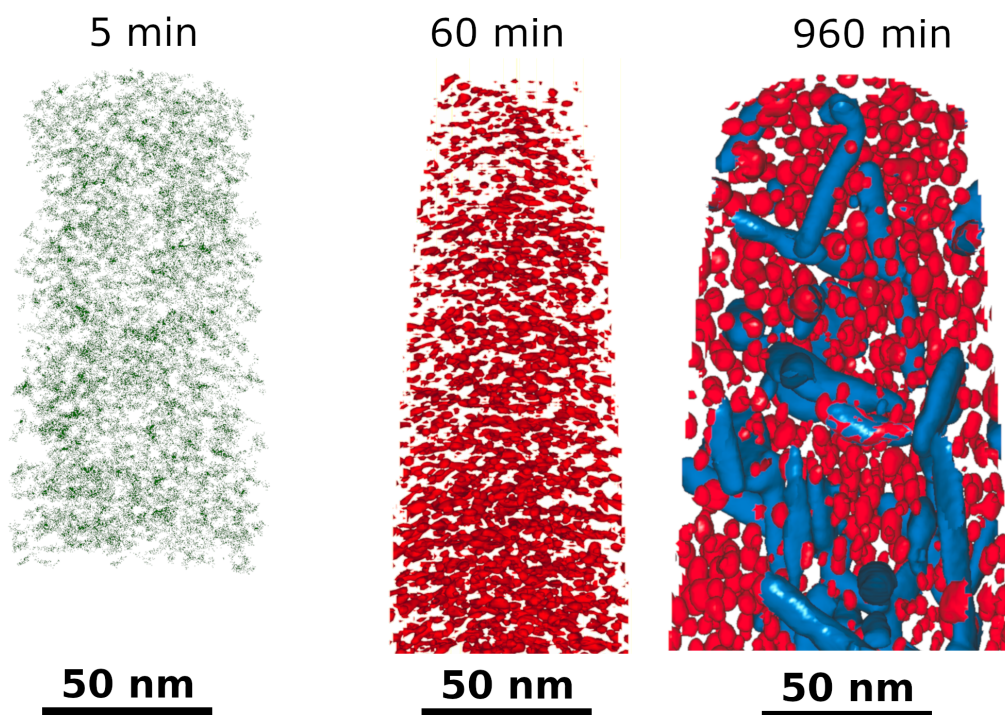


Figure 6.1: Stages of precipitate development for aging times between 5 min and 960 min at 500°C for a Fe-12Ni-10Cr-2Mo-1.5Al-1.2Ti maraging steel. The β -NiAl phase is represented by red 20 at.% Ni+Al iso-concentration surfaces while the η -Ni₃Ti phase is represented by blue 70 at.% Ni+Ti+Al iso-concentration surfaces. Adapted from *Publication I* [91].

As part of *Publication I* the solution annealed material was deformed using HPT and the influence on the precipitation during aging was studied. During HPT the material was transformed from a lath martensite microstructure to a globular microstructure as shown in Fig. 6.2.

Fig. 6.3 shows the precipitation stages after HPT. Using identical heat treatment parameters (500°C for 5 min to 960 min) it was observed that HPT changed how the material responds to the aging heat treatment. In the early stages of aging the clusters were larger and less

homogeneously distributed after HPT. Moreover, a second precipitate phase already formed after 60 min of aging which was identified as an γ' -Ni₃(Al,Ti) using selected area diffraction (SAD). Finally, after 960 min of aging it was observed that this γ' phase formed at the grain boundaries of the refined HPT material.

All material in *Publication I* was water-quenched after the aging heat treatment. Furthermore, the individual material pieces were small compared to industrial workpieces. As such, the cooling of the samples is not comparable to industrial processes, especially if we also consider that workpieces with a complex geometry might have varying cooling rates within the workpiece due to differences in the wall thickness.

Publication II addressed the role of the cooling time after aging to determine the extent to which this parameter can influence the aging of the material. Within this study material was aged at 510°C for three different aging times (0 h, 4 h, and 15 h) in combination with three different cooling times (7 h, 28 h, and 56 h). It was found that the cooling time can act as an extension of the aging process after the isothermal holding. This extension resulted in the formation of both precipitate types, despite the relatively short holding times of 0 h and 4 h.

Fig. 6.4 shows the different stages of precipitation for the samples with 0 h and 4 h holding times. The 4 h aged samples showed both precipitate types for all cooling times from 7 h to 56 h, but it was evident that the volume fraction of the η phase increased with

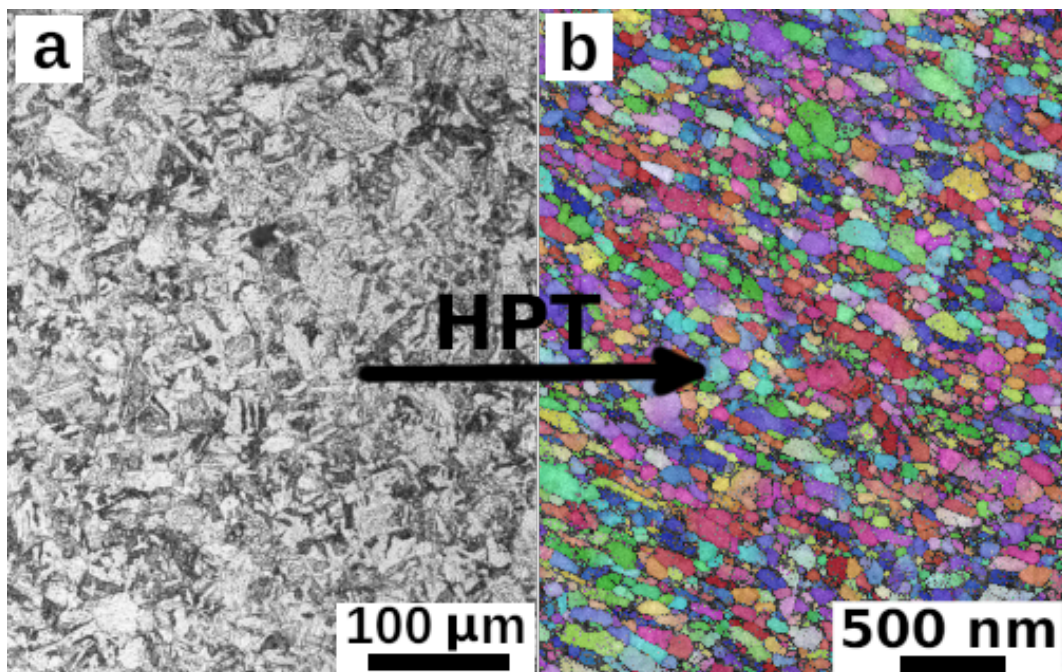


Figure 6.2: Microstructural change during HPT in the solution annealed condition of a Fe-12Ni-10Cr-2Mo-1.5Al-1.2Ti maraging steel. a) Before HPT (LOM), and b) after HPT (TKD IPF-Z map). Adapted from *Publication I* [91].

increasing cooling time. The 0 h cooling time sample group was immediately cooled after the target aging temperature was reached. With the shortest cooling time only early stage β precipitates were observed. However, with cooling times of 28 h and 56 h the η phase also precipitated, and similar to the 4 h sample the volume fraction of the η phase increased with increasing cooling time. These results were in stark contrast to the undeformed material from *Publication I*, for which the η phase was only observed after 16 h of aging. It could be shown that similar precipitation effects can be produced by prolonging the cooling time and decreasing the time of isothermal holding, a trade-off which might also be beneficial for energy consumption. Moreover, by enforcing a slow cooling rate it is possible to ensure that large workpieces with complex geometries and differences in the wall thickness cool more evenly and, as a consequence, have a more homogeneous distribution of precipitates.

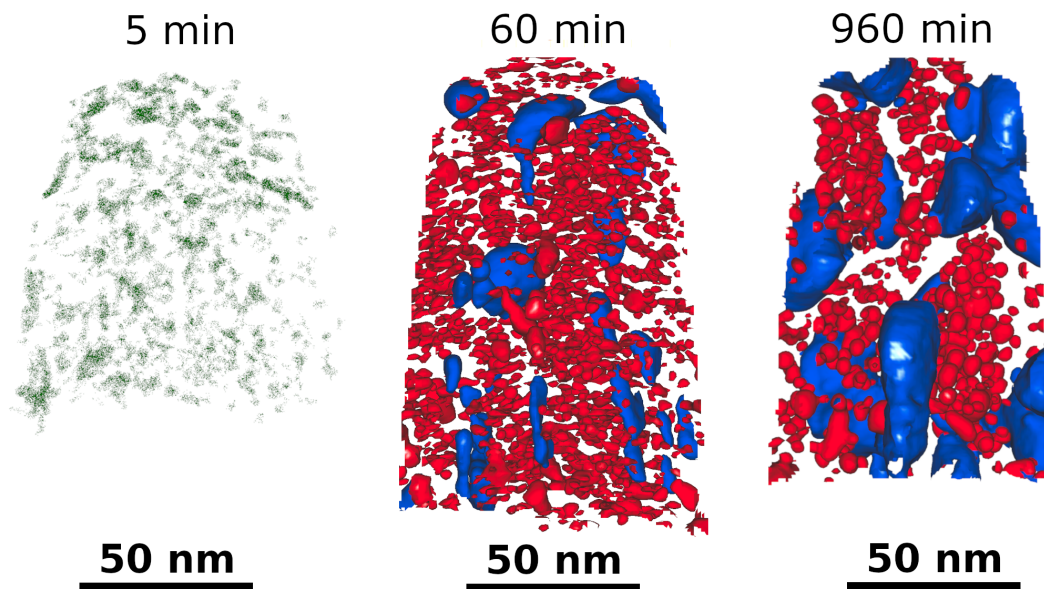


Figure 6.3: Stages of precipitate development for aging times between 5 min and 960 min at 500°C for a Fe-12Ni-10Cr-2Mo-1.5Al-1.2Ti maraging steel after HPT. The β -NiAl phase is represented by red 20 at.% Ni+Al iso-concentration surfaces while the η -Ni₃Ti phase is represented by blue 70 at.% Ni+Ti+Al iso-concentration surfaces. Adapted from *Publication I* [91].

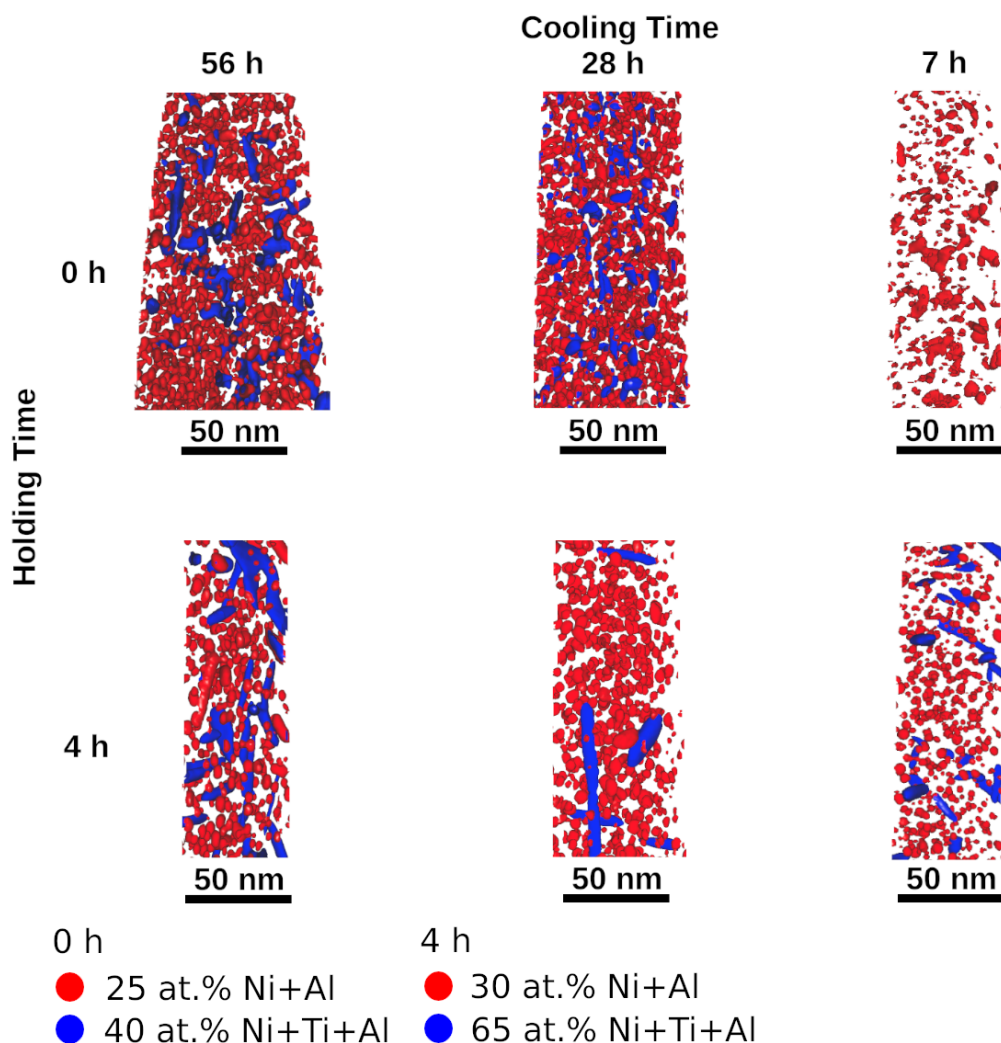


Figure 6.4: Stages of aging for a Fe-12Ni-10Cr-2Mo-1.5Al-1.2Ti maraging steel using isothermal holding times of 0 h and 4 h and using cooling times between 7 h and 56 h. The β -NiAl phase is represented by red Ni+Al iso-concentration surfaces while the η -Ni₃Ti phase is represented by blue Ni+Ti+Al iso-concentration surfaces. Adapted from *Publication II* [92].

6.3 Influence of the chemical composition on the microstructure

The influence of the chemical composition on the precipitation hardening, microstructure, and mechanical properties was studied with model alloys based on the Fe-12Ni alloy system. Fig. 6.5 shows the alloy selection process that was used for *Publication III* and *Publication IV* and Table 6.1 shows the corresponding chemical compositions. Starting from a Fe-12Ni base Al, Ti, Cr, and Mo were subsequently added to produce alloys which were numbered alloy #1 to alloy #6, like shown in Fig. 6.5 and Table 6.1. The resulting alloys were solution annealed at 850°C for 90 min and aged at 510°C for 16 h. The main interest was how the

addition of alloying elements influences the amount of austenite in the microstructure (before and after aging) and how the precipitation is influenced by the individual alloying elements.

Table 6.1: The concentration of the alloying elements (in wt.%, balanced with Fe) of the alloys used in *Publication III* and *Publication IV*.

Alloy Number - Name	wt.%				
	Ni	Cr	Mo	Al	Ti
#1 - 1Ti	11.8				0.9
#2 - 1.5Al				1.4	
#3 - 1.5Al,1Ti	11.6			1.7	0.9
#4 - 10Cr,1.5Al,1Ti	11.9	9.9		1.6	1.0
#5 - 10Cr,1Al,1.5Ti	11.9	10		0.9	1.4
#6 - 10Cr,2Mo,1.3Al,1.2Ti	12.1	10	2.1	1.3	1.2

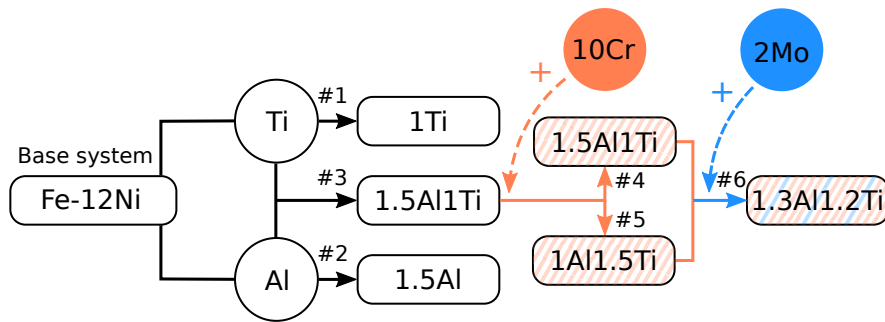


Figure 6.5: Process for the systematic alloy selection for determining the influence of Al, Ti, Cr, and Mo on the properties of Fe-12Ni maraging steels. Adapted from *Publication III*[93].

Retained and reverted austenite

To study the influence of the individual alloying elements on the formation of austenite XRD measurements were performed in the solution annealed and the aged condition (510°C/16 h) to separate the effects of retained austenite and reverted austenite. Fig. 6.6 shows the austenite fraction of all alloys in the solution annealed and the aged condition. It was observed that all Cr-free alloys showed only negligible fractions of austenite in both heat treatment conditions. Only the introduction of Cr and Mo led to an increased amount of austenite. This effect was explained by the correlation between the M_S temperature and the fraction of reverted austenite, which was previously established by Wu et al. [30]. The experiments concluded that Cr and Mo were also responsible for an increased amount of reverted austenite with Mo having a significantly stronger effect. However, the mechanism behind this effect could not be established and remains an open research question.

In *Publication I* it was shown that Mo can segregate to the grain boundaries of an HPT-deformed maraging steel with a similar chemical composition to the model alloy #6. It

was believed that the segregation of Mo to the grain boundaries strongly suppressed the formation of austenite.

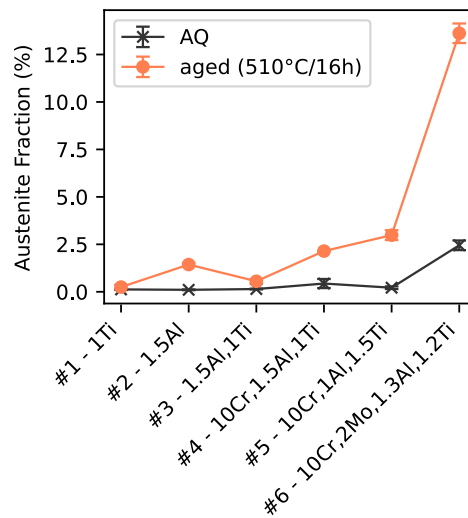


Figure 6.6: Austenite fraction of the different alloys in the solution annealed and quenched condition. Adapted from *Publication III*[93].

Fig. 6.7 shows that larger austenite grains were found between martensite blocks, packets, and prior austenite grains while smaller austenite films were found between martensite laths.

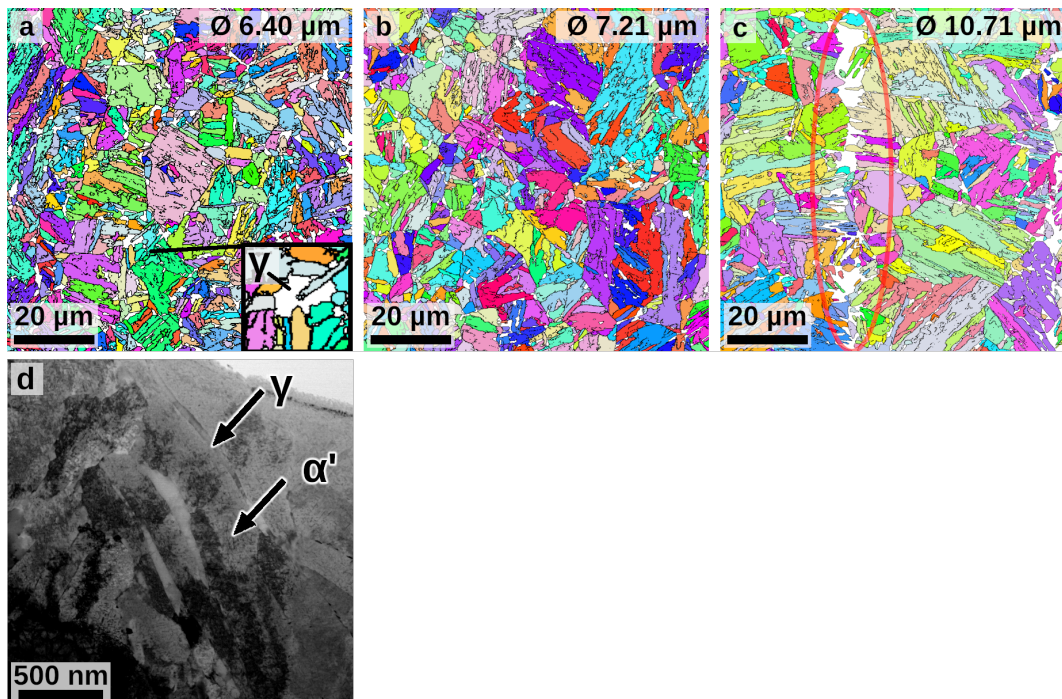


Figure 6.7: IPF-Z images obtained by EBSD. The martensite block boundaries are shown as black lines which were defined with a misorientation of 10.5° and the austenite phase is shown in white. Adapted from *Publication III*[93].

Precipitation of β -NiAl and η -Ni₃Ti

The precipitation of the β -NiAl and η -Ni₃Ti phases was strongly influenced by the chemical composition as shown in Fig. 6.8.

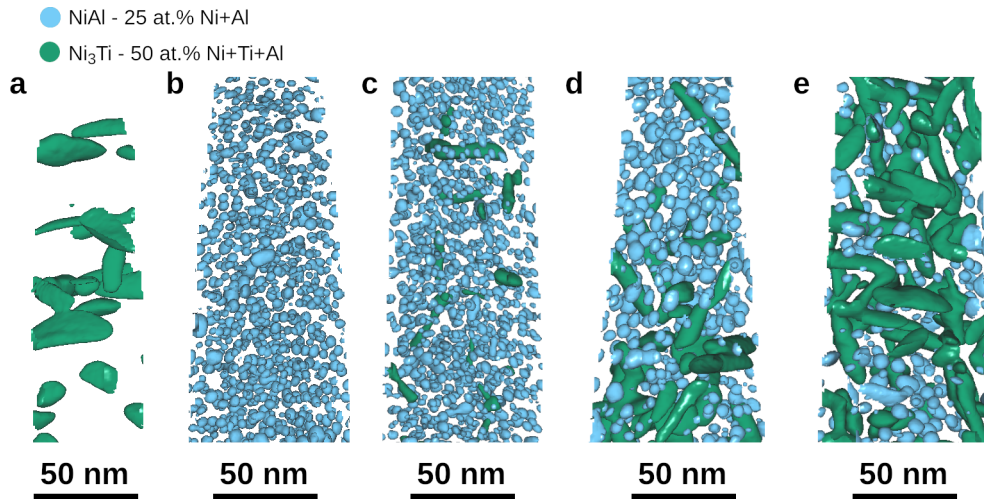


Figure 6.8: Iso-concentration surfaces showing the precipitates in model alloys #1 to #5 (a-e) after aging at 510°C for 16 h. The β -NiAl and η -Ni₃Ti phases are represented by blue and green iso-concentration surfaces, respectively. Adapted from *Publication IV* [94].

The ternary alloys with only either Al or Ti both had only one precipitate type after the aging heat treatment at 510°C and the combination of Ti and Al led to the formation of both precipitate types, but with a very low volume fraction of the η phase. A significant change in the precipitation behavior was achieved by adding Cr to the alloys which slightly increased the precipitation of the β -NiAl and significantly increased the precipitation of the η phase. After the addition of Mo to the alloys the volume fraction of the η phase increased further, however, the volume fraction of the β phase decreased. The assumption, which was proposed in *Publication III*, is that Cr and Mo decrease the bulk-diffusion speed of Al and that more Al is redistributed via pipe diffusion which could promote the formation of the η phase (which knowingly nucleates at dislocations). This assumption is backed up by the pile-up of Al which was observed at the precipitate-matrix interface of the Cr and Mo alloyed materials, as shown in Fig. 6.9. The variation of Ti and Al in the Cr alloyed materials showed that a higher Ti content leads to a higher fraction of the η phase in the aged condition at 510°C for 16 h.

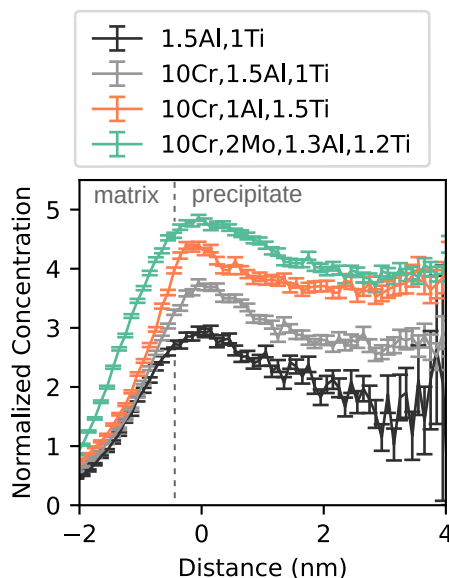


Figure 6.9: Al concentration (normalized to the bulk composition) across the η -Ni₃Ti precipitate-matrix interface for various alloy compositions. Adapted from *Publication III*[93].

6.4 Strengthening mechanisms of Fe-12Ni maraging steels

The hardness and strength of the maraging steels tested in this thesis were strongly dependent on the process and the chemical composition and the following section will elaborate on how the strength is influenced by these parameters.

Solid solution strengthening

Fig. 6.10 a shows the ultimate tensile strength of the maraging model alloys used in *Publication III* and *Publication IV*. The strength in the solution annealed condition increases with increasing alloying content, which stems from an increased contribution from solid solution strengthening.

The solid solution strengthening in maraging steels is not static but it is influenced by the aging of the material. As the aging proceeds, the atoms of precipitating elements are removed from the matrix phase while atoms from elements like Cr and Mo are expelled from the precipitates and enriched in the matrix. Fig. 6.10 c shows the chemical composition of the matrix phase for each chemical composition that was tested in *Publication IV*. It was found that Ti, followed by Al had the strongest influence on solid-solution hardening in the alloys.

A similar characterization was carried out with the industrial alloys in *Publication II* where the matrix concentration of all alloying elements was calculated as a function of the holding time and the cooling time. Fig. 6.11 a shows that, on average, the concentration of Ni, Ti,

Al, and Mo decreased with an increasing holding time at the aging temperature and with an increasing cooling time, which correlates directly to the observed decreased contribution from solid-solution strengthening which is shown in Fig. 6.11 b.

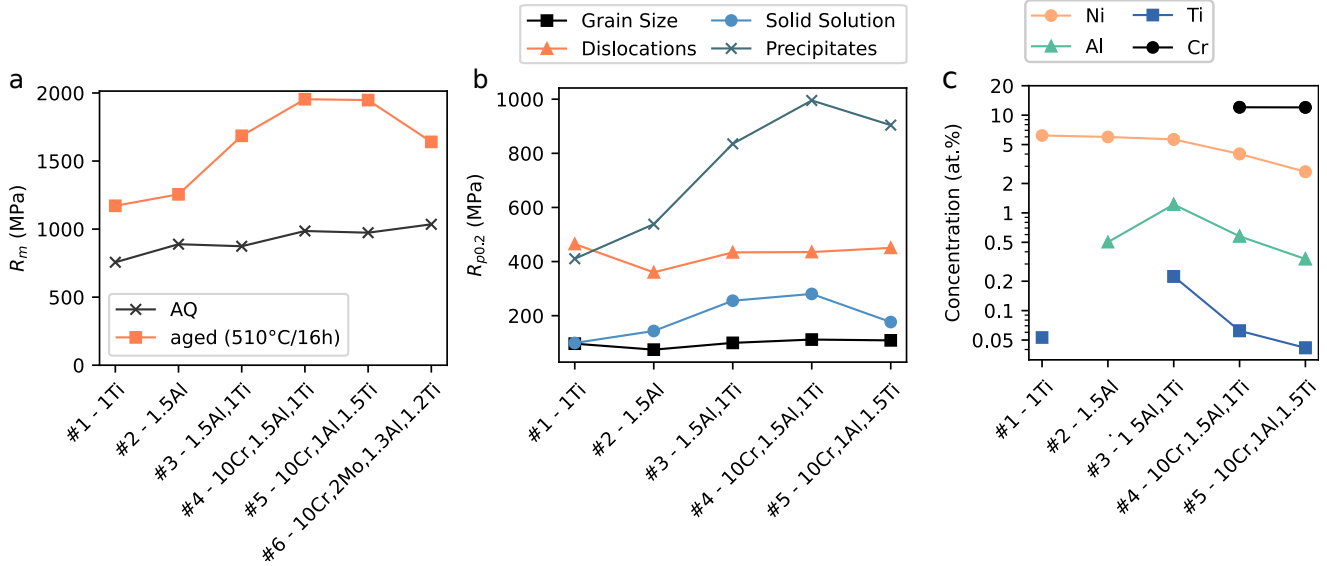


Figure 6.10: a) Ultimate tensile strength of the model maraging alloys in the solution annealed and aged condition (510°C/16 h), adapted from *Publication III*[93]. b) Contributions to the yield strength from the different strengthening mechanisms for the aged maraging model alloys, adapted from *Publication IV*[94]. c) Chemical composition of the matrix phase, adapted from *Publication IV*[94].

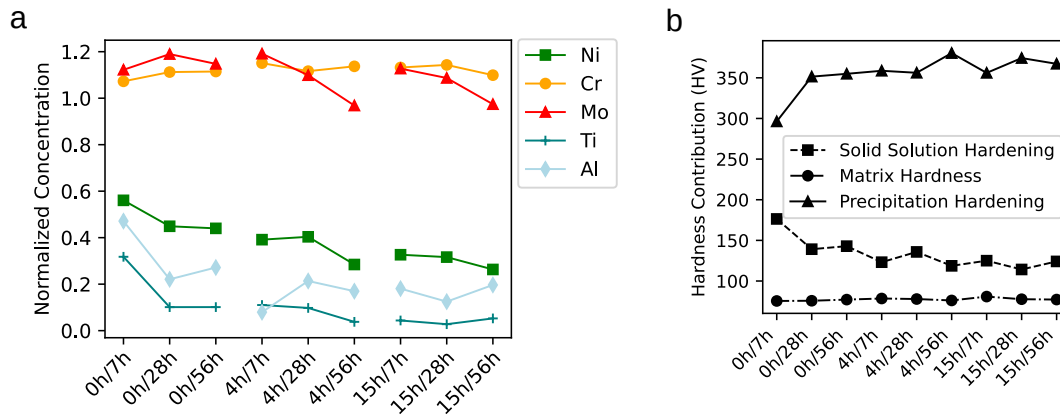


Figure 6.11: a) Chemical composition of the matrix phase of an industrial-grade Fe-12Ni-10Cr-2Mo-1.5Al-1.2Ti maraging steels as a function of the holding time and the cooling time and b) solid solution and precipitation hardening for the same alloy and aging conditions. Adapted from *Publication II*[92].

Precipitation strengthening

Investigations on the precipitation strengthening in *Publication III* could show that the η -Ni₃Ti phase had a higher strengthening effect per volume fraction than the β -NiAl phase.

To gain a deeper understanding of the strengthening mechanisms behind the η and β phase precipitation hardening the inter-precipitate distance was measured in *Publication IV* using a novel approach.

Fig. 6.12 shows the contributions to the precipitation strengthening from the η phase and the β phase and a comparison to the total yield strength in the different model alloys. It was found that the variants with only Ti and only Al (alloys #1 and #2, respectively) produced similar precipitation strengthening effects at the same aging conditions, while the combination of both elements in alloy #3 led to a significant strength increase due to the combination of two precipitate types with different strengthening mechanisms, which were the Orowan mechanism for the η phase and the shearing mechanism for the β phase. In detail, it could be shown that for the β phase the anti-phase boundary strengthening effect was the largest contribution to strengthening from the shearing mechanism. In alloy #5, with increased Ti concentration and lower Al concentration, the η phase was a stronger contributor to precipitation strengthening than the β phase. This is in agreement with the significantly higher η volume fraction in alloy #5 (see Fig. 6.8).

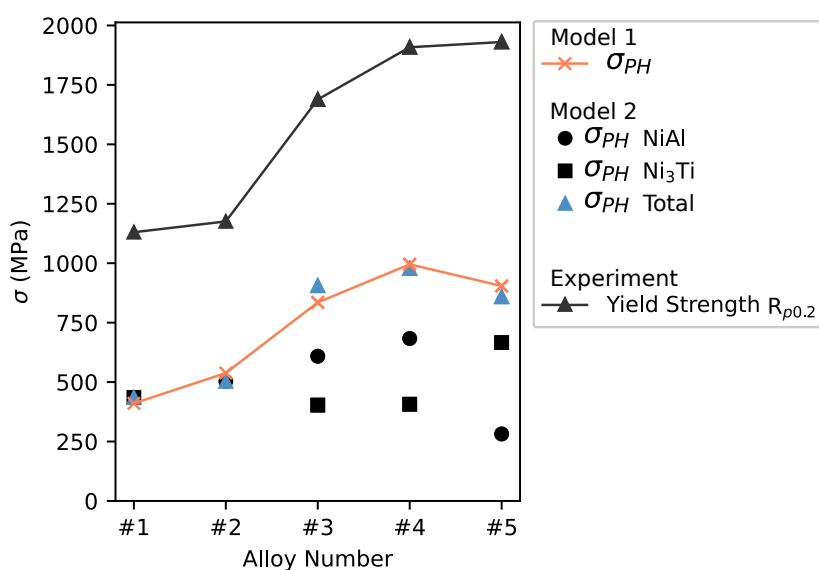


Figure 6.12: Contributions to the precipitation strengthening from the η -Ni₃Ti phase and the β -NiAl phase compared to the total yield strength. Adapted from *Publication IV* [94].

Other strengthening mechanisms

Grain size strengthening was only a small contributor to the total strength for the industrial alloy and the model alloys as shown in Fig. 6.10 b and Fig. 6.11 b. However, in *Publication I* it was found that HPT deformation in the solution annealed condition increased the hardness by 270 HV₅, as shown in Fig. 6.13. While the individual hardness contributions were not calculated for this study, it is reasonable that a large amount of this strength increase came from the refinement of the grain size to approximately 150 nm. Furthermore, Fig. 6.13 shows

that this difference remained similar during aging (up to 16 h at 510°C) of the material, which is in agreement with the results of TKD measurements that showed no grain growth after aging the HPT material.

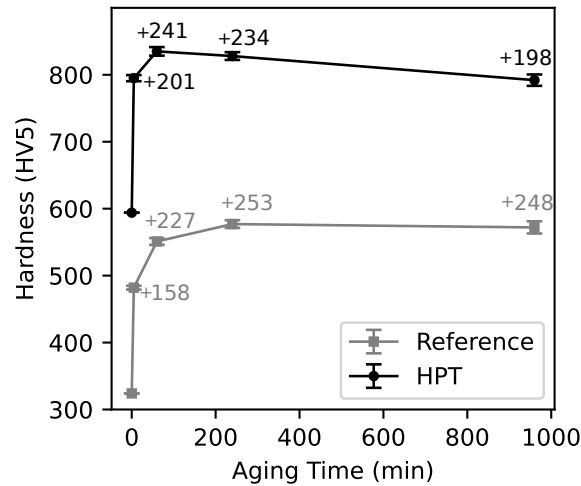


Figure 6.13: Hardness of the industrial maraging steel (with and without HPT deformation) before aging and for all aging times (aged at 500°C). The numbers (e.g. +158) indicate the hardness difference compared to the condition before aging. Adapted from *Publication I* [91].

All model alloys had a similar dislocation density that led to a strength contribution of approximately 400 MPa. While the dislocation density was not measured for the industrial alloys it seems reasonable that their dislocation density strengthening is within a similar range compared to the model alloys since the high dislocation density in maraging steels stems from the transformation of austenite to lath martensite during quenching.

Novel features

The work in this thesis generated results that were able to advance the field of Co-free maraging steels and specifically advance the knowledge about Fe-12Ni-based Co-free maraging steels and their process-structure-property relationships. The following points can be considered as novel features and findings:

- It was shown that the lath martensite microstructure of Co-free maraging steels can be refined and transformed into a globular microstructure using high pressure torsion. This transformation results in a vast increase of the hardness in the solution annealed condition. Furthermore, this transformation leads to a faster aging response and faster formation of precipitates out of the clusters.
- The adjustment of the cooling time after aging can be used to prolong the effects of aging for shorter aging times. Furthermore, a longer cooling time is beneficial to the strength of the Fe-12Ni-10Cr-2Mo-1.5Al-1Ti Co-free maraging steel.
- Cr and Mo are crucial elements for precipitation strengthening in Ti and Al alloyed Fe-12Ni maraging steels which promote the simultaneous precipitation of the η -Ni₃Ti next to the β -NiAl phase.
- The concentration of Ti and Al can be varied within 1.0 wt.% and 1.5 wt.% for both elements which allows the adjustment of a higher or lower volume fraction of the η phase or vice-versa the β phase. Within this variation range, the mechanical properties remain similar, which is a crucial advantage for using recycled material.
- A method to measure the inter-precipitate distance with results from APT was established. This method allows the calculation of the strength contributions of each type of precipitate which can be used to compare the precipitation-strengthening effect of different conditions.

Outlook

The field of maraging steels is a vast field of study that includes many different alloy compositions and different processing and heat treatment routes. Within this thesis, several questions on the behavior of Fe-12Ni Co-free maraging steels were answered, including the effect of the alloying elements Cr and Mo on the precipitation and austenite content. It was found that the interaction between the precipitation and the formation of reverted austenite is a complex process that is accompanied by the diffusion of precipitating and austenite stabilizing elements which changes the chemical composition of the matrix and thus the driving force for austenite formation. This thesis could show that Cr and Mo promote the formation of precipitates and lower the Ni concentration in the matrix for a Fe-12Ni maraging steel, but a simultaneous increase of reverted austenite was observed, which is counter-intuitive. Furthermore, it was shown that the addition of Cr and Mo promotes the formation of the η -Ni₃Ti phase. The mechanisms behind both observations remain unanswered and could be a topic for further research.

One possible solution to answer these questions could be to look at the austenite fraction over time at the aging temperature (e.g. with high-temperature XRD or dilatometer tests) and at the microstructural composition and chemistry at nano-scale for the early stages of aging for different alloy compositions with and without Cr and Mo (using APT). The results could show if these alloying elements also change the kinetics of austenite formation and how the matrix composition changes during the early stages of aging which could support or disprove the theory of slowed-down bulk diffusion established in *Paper III*. With the selfsame samples, a site-specific preparation at lath boundaries for APT might also give information about the differences in the local Ni enrichment which allows for conclusions regarding the formation of reverted austenite.

Bibliography

- [1] C. G. Bieber, Progress with 25% nickel steels for high strength applications, *Metal Progress* 78 (1960) 99.
- [2] R. F. Decker, J. T. T. Eash, A. J. J. Goldman, 18% Nickel Maraging Steel, *Trans. ASM* 55 (1962) 58–76.
- [3] R. F. Decker, C. J. Novak, T. W. Landig, Developments and projected trends in maraging steels, *Jom* 19 (1967) 60–66.
- [4] W. Sha, Z. Guo, *Maraging steels: modelling of microstructure, properties and applications*, Woodhead Publishing Ltd., Cambridge, UK, 2009.
- [5] P. Würzinger, R. Rabitsch, W. Meyer, Production of maraging steel grades and the influence of specified and nonspecified elements for special applications, *Journal of Materials Science* 39 (2004) 7295–7302.
- [6] M. Ahmed, I. Salam, F. H. Hashmi, A. Q. Khan, Influence of banded structure on the mechanical properties of a high-strength maraging steel, *Journal of Materials Engineering and Performance* 6 (1997) 165–171.
- [7] A. Fathy, T. Mattar, H. El-Faramawy, W. Bleck, Mechanical properties of new low-nickel cobalt-free maraging steels, *Steel Research* 73 (2002) 549–556.
- [8] G. M. Castro Güiza, C. A. Oliveira, Microstructural changes produced by hot forging in a C300 maraging steel, *Materials Science and Engineering A* 655 (2016) 142–151.
- [9] D. Matlock, G. Krauss, J. Speer, Microstructures and properties of direct-cooled microalloy forging steels, *Journal of Materials Processing Technology* 117 (2001) 324–328.
- [10] K. Li, B. Yu, R. D. Misra, G. Han, S. Liu, C. J. Shang, Strengthening of cobalt-free 19Ni3Mo1.5Ti maraging steel through high-density and low lattice misfit nanoscale precipitates, *Materials Science and Engineering A* 715 (2018) 174–185.

- [11] S. Zhirafar, A. Rezaeian, M. Pugh, Effect of cryogenic treatment on the mechanical properties of 4340 steel, *Journal of Materials Processing Technology* 186 (2007) 298–303.
- [12] N. S. Kalsi, R. Sehgal, V. S. Sharma, Cryogenic treatment of tool materials: a review, *Materials and Manufacturing Processes* 25 (2010) 1077–1100.
- [13] R. Schnitzer, M. Schober, S. Zinner, H. Leitner, Effect of Cu on the evolution of precipitation in an Fe-Cr-Ni-Al-Ti maraging steel, *Acta Materialia* 58 (2010) 3733–3741.
- [14] L. Sun, T. Simm, T. Martin, S. McAdam, D. Galvin, K. Perkins, P. Bagot, M. Moody, S. Ooi, P. Hill, M. Rawson, H. Bhadeshia, A novel ultra-high strength maraging steel with balanced ductility and creep resistance achieved by nanoscale β -NiAl and Laves phase precipitates, *Acta Materialia* 149 (2018) 285–301.
- [15] C.-y. Huang, H.-w. Yen, HRTEM investigations on nano precipitates in Custom 475 maraging stainless steel, *Materials Characterization* 178 (2021) 111216.
- [16] K. Li, L. Wei, B. An, B. Yu, R. D. Misra, Aging phenomenon in low lattice-misfit cobalt-free maraging steel: Microstructural evolution and strengthening behavior, *Materials Science and Engineering A* 739 (2019) 445–454.
- [17] C. Zhang, C. Wang, S. L. Zhang, Y. L. Ding, Q. L. Ge, J. Su, Effect of aging temperature on the precipitation behavior and mechanical properties of Fe–Cr–Ni maraging stainless steel, *Materials Science and Engineering A* 806 (2021) 140763.
- [18] M. Thuvander, M. Andersson, K. Stiller, Atom probe tomography investigation of lath boundary segregation and precipitation in a maraging stainless steel, *Ultramicroscopy* 132 (2013) 265–270.
- [19] R. Smallman, A. Ngan, Precipitation hardening, *Modern Physical Metallurgy* (2014) 499–527.
- [20] Y. Li, D. S. Martín, J. Wang, C. Wang, W. Xu, A review of the thermal stability of metastable austenite in steels: martensite formation, *Journal of Materials Science and Technology* 91 (2021) 200–214.
- [21] H. Zhang, M. Sun, D. Ma, B. Xu, T. Wang, D. Li, Y. Li, Effect of aging temperature on the heterogeneous microstructure and mechanical properties of a 12Cr–10Ni–Mo–Ti maraging steel for cryogenic applications, *Journal of Materials Science* 56 (2021) 11469–11484.
- [22] M. C. Niu, K. Yang, J. H. Luan, W. Wang, Z. B. Jiao, Cu-assisted austenite reversion and enhanced TRIP effect in maraging stainless steels, *Journal of Materials Science & Technology* 104 (2022) 52–58.

- [23] L. Guo, L. Zhang, J. Andersson, O. Ojo, Additive manufacturing of 18% nickel maraging steels: defect, structure and mechanical properties: a review, *Journal of Materials Science and Technology* 120 (2022) 227–252.
- [24] G. Krauss, Martensite in steel: Strength and structure, *Materials Science and Engineering A* 273-275 (1999) 40–57.
- [25] H. Calderon, M. E. Fine, Coarsening kinetics of coherent NiAl-type precipitates in FeNiAl and FeNiAlMo alloys, *Materials Science and Engineering* 63 (1984) 197–208.
- [26] H. Kitahara, R. Ueji, N. Tsuji, Y. Minamino, Crystallographic features of lath martensite in low-carbon steel, *Acta Materialia* 54 (2006) 1279–1288.
- [27] P. Thome, M. Schneider, V. A. Yardley, E. J. Payton, G. Eggeler, Crystallographic analysis of plate and lath martensite in Fe-Ni alloys, *Crystals* 12 (2022) 156.
- [28] C. K. Yao, Z. Xu, Influence of hot-deformation on morphology and effective grain size of lath martensite in 18Ni maraging steel, *Materials Chemistry and Physics* 14 (1986) 559–568.
- [29] M. Yaso, S. Hayashi, S. Morito, T. Ohba, K. Kubota, K. Murakami, Characteristics of retained austenite in quenched high C-high Cr alloy steels 1050 ° C 1150 ° C 50 (2009) 275–279.
- [30] W. Wu, L. Y. Hwu, D. Y. Lin, J. L. Lee, Relationship between alloying elements and retained austenite in martensitic stainless steel welds, *Scripta Materialia* 42 (2000) 1071–1076.
- [31] D. Barbier, Extension of the martensite transformation temperature relation to larger alloying elements and contents, *Advanced Engineering Materials* 16 (2014) 122–127.
- [32] H. Zhang, X. Ji, D. Ma, M. Tong, T. Wang, B. Xu, M. Sun, D. Li, Effect of aging temperature on the austenite reversion and mechanical properties of a Fe-10Cr-10Ni cryogenic maraging steel, *Journal of Materials Research and Technology* 11 (2021) 98–111.
- [33] U. K. Viswanathan, G. K. Dey, V. Sethumadhavan, Effects of austenite reversion during overageing on the mechanical properties of 18 Ni (350) maraging steel, *Materials Science and Engineering A* 398 (2005) 367–372.
- [34] J. Patel, M. Cohen, Criterion for the action of applied stress in the martensitic transformation, *Acta Metallurgica* 1 (1953) 531–538.

- [35] Y. Matsuoka, T. Iwasaki, N. Nakada, T. Tsuchiyama, S. Takaki, Effect of grain size on thermal and mechanical stability of austenite in metastable austenitic stainless steel, *ISIJ International* 53 (2013) 1224–1230.
- [36] Z. Guo, W. Sha, D. Vaumousse, Microstructural evolution in a PH13-8 stainless steel after ageing, *Acta Materialia* 51 (2003) 101–116.
- [37] M. Thuvander, M. Andersson, K. Stiller, Precipitation process of martensitic PH stainless steel Nanoflex, *Materials Science and Technology (United Kingdom)* 28 (2012) 695–701.
- [38] D. M. Vanderwalker, Precipitation sequence of Ni₃Ti in Co-free maraging steel, *Metallurgical transactions. A, Physical metallurgy and materials science* 18 A (1987) 1191–1194.
- [39] Y. He, K. Yang, W. Sha, D. J. Cleland, Microstructure and mechanical properties of a 2000 MPa Co-free maraging steel after aging at 753 K, *Metallurgical and Materials Transactions A: Physical Metallurgy and Materials Science* 35 A (2004) 2747–2755.
- [40] R. Tewari, S. Mazumder, I. S. Batra, G. K. Dey, S. Banerjee, Precipitation in 18 wt\% Ni maraging steel of grade 350, *Acta Materialia* 48 (2000) 1187–1200.
- [41] M. Thuvander, M. Andersson, K. Stiller, Precipitation process of martensitic PH stainless steel Nanoflex, *Materials Science and Technology* 28 (2012) 695–701.
- [42] U. K. Viswanathan, G. K. Dey, M. K. Asundi, Precipitation hardening in 350 grade maraging steel, *Metallurgical Transactions A* 24 (1993) 2429–2442.
- [43] W. Sha, A. Cerezo, G. D. W. Smith, Phase chemistry and precipitation reactions in maraging steels: part IV. Discussion and conclusions, *Metallurgical Transactions A* 24 (1993).
- [44] S. Banerjee, P. Mukhopadhyay, *Transformations Related to Omega Structures*, Pergamon Materials Series 12 (2007) 473–553.
- [45] D. J. King, M. Yang, T. M. Whiting, X. Liu, M. R. Wenman, G-phase strengthened iron alloys by design, *Acta Materialia* 183 (2020) 350–361.
- [46] A. Gemperle, J. Gemperlová, W. Sha, G. D. Smith, Aging behaviour of cobalt free chromium containing maraging steels, *Materials Science and Technology (United Kingdom)* 8 (1992) 546–554.
- [47] R. Schnitzer, S. Zinner, H. Leitner, Modeling of the yield strength of a stainless maraging steel, *Scripta Materialia* 62 (2010) 286–289.

- [48] T. H. Simm, L. Sun, D. R. Galvin, E. P. Gilbert, D. Alba Venero, Y. Li, T. L. Martin, P. A. Bagot, M. P. Moody, P. Hill, H. K. Bhadeshia, S. Biroasca, M. J. Rawson, K. M. Perkins, A SANS and APT study of precipitate evolution and strengthening in a maraging steel, *Materials Science and Engineering A* 702 (2017) 414–424.
- [49] R. Schnitzer, R. Radis, M. Nöhner, M. Schober, R. Hochfellner, S. Zinner, E. Povoden-Karadeniz, E. Kozeschnik, H. Leitner, Reverted austenite in PH 13-8 Mo maraging steels, *Materials Chemistry and Physics* 122 (2010) 138–145.
- [50] D. Pan, Y. Zhao, Y. Wang, X. Xu, X. Chong, Development of new Cobalt-free maraging steel with superior mechanical properties via electro-pulsing technology, *Metals* 9 (2019).
- [51] M. Thuvander, M. Andersson, K. Stiller, Multiple influences of molybdenum on the precipitation process in a martensitic PH stainless steel, *Metals* 9 (2019) 1118.
- [52] M. Schober, R. Schnitzer, H. Leitner, Precipitation evolution in a Ti-free and Ti-containing stainless maraging steel, *Ultramicroscopy* 109 (2009) 553–562.
- [53] M. Niu, G. Zhou, W. Wang, M. B. Shahzad, Y. Shan, K. Yang, Precipitate evolution and strengthening behavior during aging process in a 2.5 GPa grade maraging steel, *Acta Materialia* 179 (2019) 296–307.
- [54] A. Mahmoudi, M. R. Ghavidel, S. H. Nedjad, A. Heidarzadeh, M. N. Ahmadabadi, Aging behavior and mechanical properties of maraging steels in the presence of submicrocrystalline Laves phase particles, *Materials Characterization* 62 (2011) 976–981.
- [55] W. M. Garrison, M. K. Banerjee, *Martensitic non-stainless steels: high strength and high alloy*, Elsevier Ltd., 2018.
- [56] R. Schnitzer, G. A. Zickler, E. Lach, H. Clemens, S. Zinner, T. Lippmann, H. Leitner, Influence of reverted austenite on static and dynamic mechanical properties of a PH 13-8 Mo maraging steel, *Materials Science and Engineering A* 527 (2010) 2065–2070.
- [57] P. W. Hochanadel, G. R. Edwards, C. V. Robino, M. J. Cieslak, Heat treatment of investment cast PH 13-8 Mo stainless steel: Part I. Mechanical properties and microstructure, *Metallurgical and Materials Transactions A* 25 (1994) 789–798.
- [58] H. J. Rack, Age hardening-grain size relationships in 18Ni maraging steels, *Materials Science and Engineering* 34 (1978) 263–270.
- [59] P. E. Rivera-Díaz-Del-Castillo, K. Hayashi, E. I. Galindo-Nava, Computational design of nanostructured steels employing irreversible thermodynamics, *Materials Science and Technology (United Kingdom)* 29 (2013) 1206–1211.

- [60] S. Morito, H. Saito, T. Maki, T. Furuhashi, Effect of PAGS on crystallography and morphology of lath martensite in low carbon steels, *ISIJ International* 45 (2004) 91–94.
- [61] E. I. Galindo-Nava, P. E. Rivera-Díaz-Del-Castillo, A model for the microstructure behaviour and strength evolution in lath martensite, *Acta Materialia* 98 (2015) 81–93.
- [62] R. L. Fleischer, Substitutional solution hardening, *Acta Metallurgica* 11 (1963) 203–209.
- [63] A. Wilm, Physikalisch-metallurgische Untersuchungen über magnesiumhaltige Aluminiumlegierungen, *Metallurgie* 8 (1911).
- [64] R. F. Decker, S. Floreen, Maraging steels - the first 30 years, in: R. K. Wilson (Ed.), *Maraging steels : recent developments and applications*, The Minerals, Metals and Materials Society, Warrendale, Pa., 1988, pp. 1–38.
- [65] W. Sha, G. D. Smith, A. Cerezo, Atom probe field-ion microscopy study of ageing behaviour of a model FeNiCoMo maraging steel, *Surface Science* 266 (1992) 378–384.
- [66] A. Baldan, Progress in Ostwald ripening theories and their applications to nickel-base superalloys. Part I: Ostwald ripening theories, *Journal of Materials Science* 37 (2002) 2171–2202.
- [67] G. Gottstein, *Physical Foundations of Materials Science*, Springer-Lehrbuch, 3rd ed., Springer, Berlin Heidelberg, 2007.
- [68] M. R. Ahmadi, E. Povoden-Karadeniz, K. I. Öksüz, A. Falahati, E. Kozeschnik, A model for precipitation strengthening in multi-particle systems, *Computational Materials Science* 91 (2014) 173–186.
- [69] T. Gladman, Precipitation hardening in metals, *Materials Science and Technology* 15 (1999) 30–36.
- [70] A. J. Ardell, Precipitation hardening, *Metallurgical Transactions A* 16 (1985) 2131–2165.
- [71] A. P. Mouritz, *Introduction to aerospace materials*, Woodhead Publishing, 2012.
- [72] J. T. Black, R. A. Kohser, *DeGarmo's Materials and Processes in Manufacturing*, DeGarmo's, 10th ed., Wiley, Hoboken, NJ, USA, 2008.
- [73] Y. Lian, J. Huang, J. Zhang, C. Zhao, W. Gao, Z. Zhang, M. Ma, Effects of cold rolling on the microstructure and properties of Fe-Cr-Ni-Mo-Ti maraging steel, *Materials Science and Engineering A* 712 (2018) 663–670.

- [74] J. Tian, W. Wang, H. Li, M. B. Shahzad, Y. Shan, Z. Jiang, K. Yang, Effect of deformation on precipitation hardening behavior of a maraging steel in the aging process, *Materials Characterization* 155 (2019) 109827.
- [75] A. Azushima, R. Kopp, A. Korhonen, D. Y. Yang, F. Micari, G. D. Lahoti, P. Groche, J. Yanagimoto, N. Tsuji, A. Rosochowski, A. Yanagida, Severe plastic deformation (SPD) processes for metals, *CIRP Annals - Manufacturing Technology* 57 (2008) 716–735.
- [76] X. Sauvage, G. Wilde, S. V. Divinski, Z. Horita, R. Z. Valiev, Grain boundaries in ultra-fine grained materials processed by severe plastic deformation and related phenomena, *Materials Science and Engineering A* 540 (2012) 1–12.
- [77] Y. Cao, S. Ni, X. Liao, M. Song, Y. Zhu, Structural evolutions of metallic materials processed by severe plastic deformation, *Materials Science and Engineering R: Reports* 133 (2018) 1–59.
- [78] X. Queleñec, A. Menand, J. M. Le Breton, R. Pippan, X. Sauvage, Homogeneous Cu-Fe supersaturated solid solutions prepared by severe plastic deformation, *Philosophical Magazine* 90 (2010) 1179–1195.
- [79] R. Z. Valiev, M. Y. Murashkin, E. V. Bobruk, G. I. Raab, Grain refinement and mechanical behavior of the Al alloy, subjected to the new SPD technique, *Materials Transactions* 50 (2009) 87–91.
- [80] B. Schuh, F. Mendez-Martin, B. Völker, E. P. George, H. Clemens, R. Pippan, A. Hohenwarter, Mechanical properties, microstructure and thermal stability of a nanocrystalline CoCrFeMnNi high-entropy alloy after severe plastic deformation, *Acta Materialia* 96 (2015) 258–268.
- [81] J. Kappacher, O. Renk, D. Kiener, H. Clemens, V. Maier-Kiener, How grain boundary characteristics influence plasticity close to and above the critical temperature of ultra-fine grained bcc Ta_{2.5}W, *Acta Materialia* 216 (2021) 117110.
- [82] A. P. Zhilyaev, T. G. Langdon, Using high-pressure torsion for metal processing: Fundamentals and applications, *Progress in Materials Science* 53 (2008) 893–979.
- [83] M. K. Miller, R. G. Forbes, *Atom-probe tomography: the local electrode atom probe*, Springer, New York, NY, USA, 2014.
- [84] A. Roth, *Vacuum technology*, 3rd ed., Elsevier Science, Amsterdam, The Netherlands, 2012.

- [85] B. Gault, M. Moody, J. M. Cairney, S. P. Ringer, Atom probe microscopy, Springer, New York, 2012.
- [86] T. Kelly, D. Larson, J. Bunton, R. O. Neil, Local electrode atom probe tomography, Springer, New York, NY, USA, 2006.
- [87] F. Theska, S. P. Ringer, S. Primig, Atom Probe Microscopy of Strengthening Effects in Alloy 718, *Microscopy and Microanalysis* 25 (2019) 470–480.
- [88] S. Pogatscher, H. Antrekowitsch, H. Leitner, A. S. Sologubenko, P. J. Uggowitzer, Influence of the thermal route on the peak-aged microstructures in an Al-Mg-Si aluminum alloy, *Scripta Materialia* 68 (2013) 158–161.
- [89] L. T. Stephenson, M. P. Moody, P. V. Liddicoat, S. P. Ringer, New techniques for the analysis of fine-scaled clustering phenomena within atom probe tomography (APT) data, *Microscopy and Microanalysis* 13 (2007) 448–463.
- [90] E. A. Jäggle, P. P. Choi, D. Raabe, The maximum separation cluster analysis algorithm for atom-probe tomography: parameter determination and accuracy, *Microscopy and Microanalysis* 20 (2014) 1662–1671.
- [91] S. Zeisl, A. Lassnig, A. Hohenwarter, F. Mendez-Martin, Precipitation behaviour of a Co-free Fe-Ni-Cr-Mo-Ti-Al maraging steel after severe plastic deformation, *Materials Science and Engineering: A* 833 (2021) 142416.
- [92] S. Zeisl, R. Schnitzer, Cooling rate controlled aging of a Co-Free Fe-Ni-Cr-Mo-Ti-Al maraging steel, *Metals* 12 (2022).
- [93] S. Zeisl, A. Landefeld, N. Van Steenberge, Y. Chang, R. Schnitzer, The role of alloying elements in NiAl and Ni₃Ti strengthened Co-free maraging steels, *Materials Science and Engineering: A* 861 (2022) 144313.
- [94] S. Zeisl, N. V. Steenberge, R. Schnitzer, Strengthening effect of NiAl and Ni₃Ti precipitates in Co-free maraging steels, *Journal of Materials Science (Manuscript under review)* (2023).